Development of Mesoporous Carbon Fibers as Novel Catalyst Supports for Polymer Electrolyte Fuel Cell

黄, 亭維

Development of Mesoporous Carbon Fibers as Novel Catalyst Supports for Polymer Electrolyte Fuel Cell

Ting-Wei Huang

2020 年 7 月

Development of Mesoporous Carbon Fibers as Novel Catalyst Supports for Polymer Electrolyte Fuel Cell

九州大学
KYUSHU UNIVERSITY

A dissertation submitted to the Kyushu University
in partial fulfillment of the requirements for the
degree of Doctor of Engineering

By

Ting-Wei Huang

Department of Hydrogen Energy System
Graduate School of Engineering
Kyushu University

Approved by :
Prof. Dr. Akari Hayashi, thesis examiner/supervisor
Graduate School of Engineering, Kyushu University

Prof. Dr. Kohei Ito, thesis co-examiner
Graduate School of Engineering, Kyushu University

Prof. Dr. Tsuyohiko Fujigaya, thesis co-examiner
Graduate School of Engineering, Kyushu University

Fukuoka, Japan
2020

Abstract

In this work, hydrogen energy was focused on as one of the solutions for global environmental problems through the combination with renewable energy. Polymer electrolyte fuel cell (PEFC) generating electricity with a hydrogen fuel was particularly focused on among technologies related to hydrogen energy. Even though PEFC is a commercialized technology, cost and durability are still barriers on the way of further spreading PEFC. Particularly, degradation of catalyst layers is a serious problem since they mainly determine PEFC performance. Catalyst layers are commonly composed of electrocatalysts, Pt particles dispersed on carbon, and a proton conduction ionomer. One of degradation mechanisms of cathode electrocatalysts is known to agglomeration of Pt particles on the carbon support. In the previous work, Pt particles were encapsulated within pores of mesoporous carbon (MC) supports, resulting in increase in durability of electrocatalysts. However, a critical issue that the μm-scale structure was not well controlled although the nm-scale structure was well controlled was found. Since the μm-scale structure of catalyst layers was very important to get high PEFC performance, only slightly low PEFC performance was achieved.

In this study, in order to solve the problem on the μm-scale structure, controlling of the three-dimensional μm-scale structure was proposed by further fiberization of MC using an electrospinning deposition (ESD) method. The objectives of this research were to develop MC fibers (MCFs), to apply to catalyst layers of PEFC, and then to improve PEFC performance.

In chapter 1, a research background, advantages, and critical issues of PEFC technology were first introduced. Then, the previous research approach toward the durability issue of electrocatalysts was explained. Finally, objectives and research approaches of this study were introduced based on the critical issue found in the previous study.

In chapter 2, synthetic and material characterization methods for MCFs were introduced. Then, the methods of material and electrochemical characterization as electrocatalysts were explained after Pt deposition on MCFs. Lastly, for the evaluation as PEFC, preparation and evaluation methods of membrane electrode assemblies (MEAs) were discussed.

In chapter 3, different MCFs were prepared by varying conditions, such as pH, concentration, heat treatment, and so on, and characterized to find an optimum condition in order to get MCFs with the large pore diameter and pore volume. After the optimization of synthetic conditions, MCFs revealed the fiber diameter of 1-2 μm and

the mesopore diameter of 4 nm or larger. Because of their fiber structure, the higher elasticity and electronic conductivity was achieved in comparison to MC bulk.

In chapter 4, as electrocatalyts, various MCFs were electrochemically evaluated after Pt deposition. Electrochemical active surface area (ECSA) and oxygen reduction reaction (ORR) activity of MCFs based electrocatalysts were characterized. MCFs with 2.5-3 nm Pt nanoparticles encapsulated into 4-5 nm mesopores showed highest ORR activity among MCF based electrocatalysts, which was comparative to a conventional electroatalyst. Also, a correlation between ORR activity and mesoporosity was studied. Mesopores with the larger diameter and larger pore volume were necessary for large ECSA and high ORR activity, derived by good dispersion of Pt particles.

In chapter 5, for the evaluation as PEFC, MEAs were prepared with MCFs based cathodes. With MCF with 4-5 nm mesopores, current-voltage (I-V) performance resulted in slightly low in comparison to a conventional electroatalyst. However, after the further enlargement in mesopore diameter to 6-7 nm, the improvement in I-V performance was found, the current density reached to 615 mA/cm^2 at 0.6 V, which was almost the same current density as the conventional MEA. However, in order to further improve I-V performance, especially to reduce concentration overvoltage, it was found that MCF-based powder was not appropriate to fully control the structure of catalyst layers.

Toward a problem in MCFs powder, MCF sheet was rather applied to the cathode. Pt deposited MCF sheet was first directly used as a cathode, but the I-V performance resulted in very low since the contact between the electrolyte membrane and MCF sheet was not good because of large inter-fiber pores of several micrometers. Then, conventional electrocatalyst powder was added to MCF sheet to partially fill up those inter-fiber pores. With this composite cathode, I-V performance was a lot improved, and slightly less than conventional I-V performance. On the other hand, ohmic resistance was improved than that of conventional MEA because of the sheet structure of MCF sheet. Furthermore, addition of conventional electrocatalyst powder to Pt deposited MCF sheet was tried. However, no improvement in I-V performance was obtained. The reason was probably because introduction of a proton conducting ionomer into MCF sheet was not successful, and further improvement on introduction methods was found to an issue to overcome for the further improvement.

In chapter 6, as conclusions, new findings though this study were summarized, and future outlook for further improving PEFC performance was discussed.

Acknowledgements

At first, I would like to express my sincere gratitude to my supervisor – *Professor Akari Hayashi*, for teaching and advising me in electrocatalyst research and writing this Ph. D. thesis and her continuous and extraordinary support in my life in Japan and doing research in Kyudai. I am glad and very proud that I could enter her research group for my doctoral research.

Besides my professor, I would like to thank the members of the dissertation committee, *Professor Tsuyohiko Fujigaya*, and *Professor Kohei Ito*, for their acceptance of acting as co-examiners and providing valuable comments for my thesis.

I am the deepest gratitude to *Professor Kazunari Sasaki* for providing me with such a great environment and characterization instruments for my research. Without his help, various characterizations in my thesis could be difficult to access.

I would like to thank *Associate Professor Masamichi Nishihara* and *Associate Professor Stephen M. Lyth* and other staff in I2CNER to give me an adviser as I started my research and helped me in various characterizations in I2CNER. The discussion from other research filed always help me to correct my research direction.

I would like to thank *Associate Professor Yusuke Shiratori* and *Assistant Professor Yuya Tachikawa* for giving me comments and suggestions during the PEFC seminars. Their constructive comments helped me to improve my scientific illustration and presentation skills.

I especially thank *Technician Staff Mrs. Mayumi Nagayama*, in Professor Hayashi's group to help me in the inventory and other supporting work in my daily experiment. I have greatly benefited my work efficiency from her support.

I would like to thank *Mr. Albert Mufundirwa*, *Dr. Marika Muto*, and *Mr. Bo Fu*. They gave lots of help about living in Fukuoka as a new coming international student. Whiteout their support, I can't get used to and start focusing on my research so quickly.

I thank my colleague and friends in the Advanced Hydrogen Energy System Laboratory, the Hydrogen Utilization Process Laboratory, and International Institute for Carbon-Neutral Energy Research (I2CNER) for their assistance during my studies. I especially want to thank *Dr. Zhiyun Noda* for her advice and support in my research. Also special thanks to *Mr. Yoshinori Nagai* for teaching me several useful skills in SEM/STEM observation, which became an essential tool in my study. Special thanks to *Mrs. Ayumi Zaitsu* for her continuing help in administrative duties.

I would like to thank the "Japan-Taiwan Exchange Association" for providing me a scholarship for my life and study at Kyushu University.

Finally, I would like to express my sincere gratitude to my family: my parents, y younger brother who always supports my decisions, and gives me strong encouragement in this 3-years study.
This thesis is dedicated to all of them.

Fukuoka, July 2020
HUANG Ting-Wei

Table of Contents

Chapter 1 : Introduction 1
1.1 Energy technology transition 1
1.2 Fuel cells 2
1.2.1 Alkaline fuel cells (AFCs) 3
1.2.2 Phosphoric acid fuel cells (PAFCs) 4
1.2.3 Molten carbonate fuel cells (MCFCs) 5
1.2.4 Solid oxide fuel cells (SOFCs) 6
1.3 Polymer electrolyte fuel cells (PEFCs) 7
1.3.1 History of PEFCs 7
1.3.2 Working principle of PEFC 7
1.3.3 Advantages and critical issues for PEFC 10
1.4 Carbon support in catalyst layer of PEFCs 12
1.4.1 Carbon support in general 12
1.4.2 Mesoporous carbon (MC) 13
1.4.3 Carbon nanofibers (CNFs) 14
1.5 Electrospinning deposition (ESD) in PEFCs 14
1.6 Objective 16
1.6.1 Background of this study 16
1.6.2 Object of this study 16
Chapter 2 : Experimental Method 26
2.1 Material syntheses 26
2.1.1 Chemicals used in this study 26
2.1.2 Synthesis of fundamental mesoporous carbon (MC) 26
2.1.3 Synthesis of mesoporous carbon fibers (MCFs) precursor solution for electrospinning deposition (ESD) 27
2.1.4 Synthesis of MCFs 29
2.1.5 Deposition of Pt onto MCFs 32
2.2 Characterizations methods 33
2.2.1 N_2 adsorption/desorption measurements 33
2.2.2 Scanning electron microscope (SEM)/scanning transmission electron microscope (STEM) observation 35
2.2.3 X-ray diffraction (XRD) analysis 36
2.2.4 Thermogravimetric analysis (TGA) 37
2.2.5 CHN elementary analysis 38
2.2.6 Focused ion beam (FIB)-SEM obsercation 39

2.3 Fundamental electrochemical characterization 39
2.3.1 Principle of a solution half-cell measurement 39
2.3.2 Preparation of a working electrode 41
2.3.3 Cycling voltammetry (CV) and linear sweep voltammetry (LSV) 41
2.3.4 Electrochemical active surface area (ECSA) 42
2.3.5 ORR measurements with rotating disk electrode (RDE) 44
2.3.6 Electrochemical double layer 46
2.3.7 Charge and discharge (CDC) curves 47
2.4 Preparation and evaluation of MEAs 48
2.4.1 Slurry preparation 48
2.4.2 Preparation of MEAs 49
2.4.3 Evaluation of MEAs 50
2.4.4 Separation of ohmic, activation, and concentration overvoltage 51
2.4.5 Evaluation of through plane electronic resistance 53
Chapter 3 : Synthesis and Characterization of MCFs 57
3.1 Syntheses of MCFs 57
3.1.1 MCFs made with different linear additives for ESD 57
3.1.2 MCFs made with different precursors/additive ratios 60
3.1.3 MCFs made with different pH conditions 61
3.1.4 MCFs made with higher concentration of precursors 63
3.2 Optimization of the calcination process for MCFs 64
3.2.1 Evaluation of decomposing temperate of as-spun MCFs 64
3.2.2 Evaluation of changes in crystallinity under different calcination conditions 64
3.2.3 Evaluation of changes in the C and H atomic percent under different calcination conditions 66
3.2.4 Evaluation of changes in mesoporosity under different calcination conditions 67
3.3 Characterization of MCFs 68
3.3.1 Observation of morphology of MCF-A, MCF-HC and MCF sheet 68
3.3.2 Evaluation of MCF-A thin films: resistance toward compression 71
3.3.3 Evaluation of MCF-A thin films: through plane electronic resistance 72
3.3.4 Evaluation of fundamental electrochemical properties of MCF-A 74
3.4 Conclusion 77
Chapter 4 : Characterization of Pt Deposited MCFs (Pt/MCFs) 80
4.1 Material characterization 80
4.1.1 Evaluation of the weight percentage of Pt on MCFs 80

4.1.2 Evaluation of morphology of Pt/MCFs....81
4.1.3 Evaluation of mesoporosity changes before and after Pt deposition....84
4.1.4 Evaluation of crystallinity....84
4.2 Electrochemical characterization....87
4.2.1 Evaluation of ECSA....87
4.2.2 Evaluation of ORR activity....88
4.3 Conclusion....90
Chapter 5 : Evaluation of MEAs Made by Pt/MCFs Cathodes....93
5.1 Evaluation of MEA made by MCF-A cathode....93
5.2 Evaluation of MEA made by Pt/MCF-HC cathode....96
5.3 Evaluation of MEAs made by MCF sheet cathode....98
5.4 Conclusion....103
Chapter 6 Conclusion and Future Outlook....106
6.1 Conclusion....106
6.2 Future outlook....107

List of Figures

Fig. 1.1 A schematic diagram of gas voltaic battery by Dr. William Grove. 2
Fig. 1.2 A schematic of working principle of AFCs. 3
Fig. 1.3 A schematic of working principle of a PAFC. 4
Fig. 1.4 A schematic of working principle of a MCFC. 5
Fig. 1.5 A schematic of working principle of a SOFC. 6
Fig. 1.6 A scheme diagram showing working principle of PEFCs. 8
Fig. 1.7 A typical IV performance curve of PEFCs. 10
Fig. 1.8 A schematic diagram of F127 micelles in MC precursors. 13
Fig. 1.9 A schematic drawing of controlled microstructure and macrostructure aimed in this study 17
Fig. 1.10 Research approach in this study. 18
Fig. 2.1 Molecular structure of PVA (a) and PVB (b). 27
Fig. 2.2 Molecular structures of resorcinol (a) and pholoroglucinol (b). 28
Fig. 2.3 A typical setup of vertical ESD devise 30
Fig. 2.4 A schemetic diagram showing interaction between the polymer solution and voltage charge during ESD. 30
Fig. 2.5 A actual photo of ESD instrument used in this study. 31
Fig. 2.6 Photos of as-spun fibers (a) and stabilized fibers (b), and an SEM image of carbonized fibers (c). 31
Fig. 2.7 A schematic of Pt deposition process. 32
Fig. 2.8 A schematic diagram of the Pt deposition process on MCF sheet. 33
Fig. 2.9 A schematic diagram of the multilayer adoption model. 35
Fig. 2.10 Schematic diagrams showing the working principle of SEM (a) and STEM (b). 36
Fig. 2.11 A schematic diagram showing principle of XRD. 37
Fig. 2.12 A photo of CHN analyzer. 38
Fig. 2.13 A diagram showing of 3-electrode half-cell setup. 39
Fig. 2.14 A scheme diagram of double junction Ag/AgCl electrode. 40
Fig. 2.15 CV potential waveform. 42
Fig. 2.16 A typical cyclic voltammogram for Pt/C in the acid electrolyte. 43
Fig. 2.17 A schematic diagram of RDE working principle. 44
Fig. 2.18 Typical LSVs with different rotation speeds (a) and corresponding Koutecky-Levich plots (b) of Pt/C. 46
Fig. 2.19 Typical CV curves showing electrochemical double layers of carbon materials with different surface area. 47

Fig. 2.20 Typical CDC curves for different carbon materials. 48
Fig. 2.21 Schematic drawing of the preparation procedure of Pt/KB-MCF sheet cathode. 50
Fig. 2.22 A schematic diagram of the assembly of a MEA and a holder designed by NEDO project. 51
Fig. 2.23 A typical Nyquist plot and the corresponding electric circuit for PEFC. 52
Fig. 2.24 A schematic diagram of a test cell for evaluation of through plane electronic resistance. 53
Fig. 3.1 (a) N_2 sorption isotherms and (b) BJH plots of MCF-PVA and MCF-PVB. 58
Fig. 3.2 Molecular formulas showing (a) F127, (b) PVA and (c) PVB and corresponding dipole moment (red arrow) caused by O-atoms. 59
Fig. 3.3 Schematic drawings showing possible molecular arrangements in fibers made by PVA (a) and PVB (b) during ESD. 59
Fig. 3.4 (a) N_2 sorption isotherms and (b) corresponding BJH plots of MCF-PVA and MCF-B. 60
Fig. 3.5 A schematic diagram of H-bonding between the Pluronic F127 and carbon precursor resin. 61
Fig. 3.6 (a) N_2 sorption isotherms and (b) corresponding BJH plots of MCF-A, MCF-WA and MCF-B 62
Fig. 3.7 (a) N_2 sorption isotherms and (b) corresponding BJH plots of MCF-HC, MCF-A and bulk MC. 63
Fig. 3.8 The TGA result of as–spun MCF-A and its 1st derivative to temperature. 64
Fig. 3.9 XRD patterns of MCF-A precursor fibers treated with different calcination conditions and Vulcan® XC-72 as a reference. 65
Fig. 3.10 (a) N_2 sorption isotherms and (b) corresponding BJH plots of MCF-A precursor fibers treated under different calcination conditions. 67
Fig. 3.11 (a) SEM, (b) high magnification SEM, and (c) TEM images of MCF-A. 69
Fig. 3.12 (a) SEM, (b) high magnification SEM, and (c) TEM images of MCF-HC 70
Fig. 3.13 (a) surface and (b) cross-sectional SEM images of a single MCF sheet (0.4 mgC/cm^2). 71
Fig. 3.14 Cross-sectional FIB-SEM observation before and after the compression test of (a) bulk MC and (b) 450 rpm ball-milled MCF-A thin layers. 72

Fig. 3.15 Through plane electric resistance of thin films made by different carbon samples. 73
Fig. 3.16 MCF with (a) 800-rpm ball-milling and (b) 450-rpm ball-milling. 73
Fig. 3.17 CVs of MCF-A, bulk MC, Vulcan® XC-72, and CNF. 74
Fig. 3.18 (a) CDC response of voltage under applying 25 μA and (b) discharge specific capacitance in different charging current for different carbon materials. 75
Fig. 3.19 CDC response of voltage of Vulcan XC-72 (a), CNF (b), MCF-A (c) and bulk MC (d) under different charging current. 76
Fig. 4.1 Changes in wt.% of various Pt/carbon materials obtained by TGA. 81
Fig. 4.2 SEM images of (a), (b) 14 wt.% Pt/MCF-PVA, (c), (d) 13 wt.% Pt/MCF-B, (e), (f) 26 wt.% Pt/bulk MC, and (g), (h) 28 wt.% Pt/MCF-A. 82
Fig. 4.3 SEM/STEM images of 28 wt.% Pt/MCF-A. 83
Fig. 4.4 STEM images of (a) 26 wt.% Pt/bulk MC and (b) 28 wt.% Pt/MCF-A. 84
Fig. 4.5 (a) BET isotherms and (b) corresponding BJH plots of MCF-A before and after Pt deposition. 84
Fig 4.6 XRD patterns of TKK 46 wt.% Pt/KB, 26 wt.% Pt/bulk MC and 28 wt.% Pt/MCF-A. 85
Fig. 4.7 STEM images of original Pt/MCF-A and modified Pt/MCF-A. 86
Fig. 4.8 (a) XRD patterns of original Pt/MCF-A and modified Pt/MCF-A, and (b) Pt particle size obtained from STEM images (bar with the range) and Pt(1 1 1) peak in XRD patterns (square). 86
Fig. 4.9 CVs of (a) Pt/MCF-PVA and Pt/MCF-B and (b) Pt/MCF-A, Pt/bulk MC and Pt/KB. 87
Fig. 4.10 LSV curves of Pt/MCF-PVA and Pt/MCF-B under 1600 rpm. 88
Fig. 4.11 (a) LSV curves of Pt/MC, Pt/MCF and Pt/KB under 1600 rpm and (b) the corresponding K-L plots at 0.9 V. 89
Fig. 5.1. IV performance of MEAs made with TKK 46 wt.% Pt/KB and 28 wt.% Pt/MCF-A cathodes. 93
Fig. 5.2. (a) Activation overvoltage, (b) ohmic overvoltage, and (c) concentration overvoltage separated from I-V curves of MEAs made with TKK 46 wt.% Pt/KB cathode and 28 wt.% Pt/MCF-A cathodes. 94
Fig. 5.3 IV performance of MEAs made with Pt/MCF-A with the different Nafion content. 95
Fig. 5.4. IV performance of MEAs made with Pt/MCF-HC, Pt/MCF-A and TKK Pt/KB cathodes. 96
Fig. 5.5 (a) Activation overvoltage, (b) ohmic overvoltage, and (c) concentration

overvoltage of MEAs made with 28 wt.% Pt/MCF-HC, 28 wt. % MCF-A and TKK 46 wt.% Pt/KB. 97
Fig. 5.6. IV performance of MEAs made with 28 wt.% Pt/MCF-HC, 46 wt.% Pt/KB-MCF sheet, and TKK 46 wt.% Pt/KB cathodes. 99
Fig. 5.7. (a) Ohmic overvoltage, (b) Nyquist plots obtained at 200 mA/cm^2, (c) activation overvoltage and (c) concentration overvoltage MEAs made with 46 wt.% Pt/KB-MCF sheet, 28 wt.% Pt/MCF-HC, and 46 wt.% Pt/KB cathodes..... 99
Fig. 5.8 IV performance of MEAs made with Pt/KB-Pt/MCF sheet, Pt/KB-MCF sheet and TKK Pt/KB cathodes. 100
Fig. 5.9 (a) Activation overvoltage, (b) ohmic overvoltage, (c) Nyquist plots obtained at 200 mA/cm^2, and (d) concentration overvoltage MEAs made with 46 wt.% Pt/KB-Pt/MCF sheet, 46 wt.% Pt/KB-MCF sheet, and TKK 46 wt.% Pt/KB cathodes. 101
Fig. 5.10 IV performance of MEAs made with 46 wt.% Pt/KB/Pt/MCF sheet, 46 wt.% Pt/KB/MCF sheet, TKK 46 wt.% Pt/KB (0.30 mgPt/cm^2), and TKK 46 wt.% Pt/KB (0.15 mgPt/cm^2) cathodes..... 102
Fig. 6.1 Schematic diagrams showing introduction of Nafion ionomer on MCF sheet by spray-printing process (a) and dip coating process (b). 108
Fig. 6.2 Schematic diagrams showing Pt deposition on MCF sheet by PVD process (a) and CVD process (b). 108
Fig. 6.3 A schematic diagram of co-axial electrospinning device. 109

List of Tables

Table 1.1 Different types of fuel cells.....3
Table 2.1 Specification of MEAs.....49
Table 3.1 CHN elemental analyze (H and C) of MCF-A precursor fibers treated with different temperature.....66
Table 4.1 Electrocatalysts evaluated in this section.....87

CHAPTER 1

Introduction

Chapter 1 : Introduction

1.1 Energy technology transition

Since the first Industrial Revolution in 1760, the power provided by steam engine replaced the human and animal forces in the industrial manufacturing system, and further led to the explosively growth in economic and population. Until now, the combustion of fossil fuels, from charcoal, gasoline, natural gas, to the shell oil, has become the major way to generate energy. Previously, products from the combustion of fossil fuel, NO_x and CO_2, were not considered as harmful things to our planet. However, there were various of evidences [1] proving that observable climate changes in the recent few decades are associated with the increasing of NO_x and CO_2 gases. In 2005, to deal with climate issues, temperature raising and acid rain, etc., the Kyoto Protocol [2] was established to control and eliminate the generation of greenhouse gases (GHGs), CO_2 and NO_x. From then on, the developing in alternating energy sources are receiving more interest in recent years.

Renewable energy is the way that collect energy from nature sources, such as sunlight, wind, rain, waves, and geothermal heat. Although they are naturally replenished on a human timescale, the intensity is frequently changing, which makes them difficult to combine into the electricity grid for the stable support. Some of countries use extra system to smooth the electricity fluctuation. In Australia, there are Tesla mega battery center [3], which is based on a large number of Li-ion battery stacks. In Taiwan, there is power-leveling [4], turning extra electricity into a storable media for re-using, such like pumping water into the water dam for the turbine generator. In Japan, hydrogen energy is focused on, “Re-energy” is the strategy to turn extra electricity into hydrogen and re-use it by using fuel cells [5].

Unlike other renewable energy system, setting up a hydrogen energy system doesn’t require the location selection. Therefore, it can be built in any place like the battery center. At the same time, the same volume of hydrogen gas stored in high pressure tank can generate more electricity than Li-ion batteries [6]. Considering re-using of hydrogen gas, fuel cells are the device that directly converts chemical energy from hydrogen gas into electricity with the high efficiency and low carbon emission way [7]. Details of different type of fuel cells are further introduced in next section.

1.2 Fuel cells

The fuel cell technology has been discovered since 1842 by Dr. William Grove, a British researcher. The first one fuel cell was named as the gas voltaic battery (cell design in detail was shown at Fig. 1.1), each cell consisted with two Pt wires, used as electrode and catalyst, and the electrolyte solution, the diluted sulfonic acid. Each Pt wire was placed into a glass tube which contained reactant gases, hydrogen and oxygen. Electricity was generated from the four connected systems by consuming reactant gas. This is first time human produce electricity from consuming gases. Since this gas voltaic battery consuming hydrogen and oxygen like a fuel, the "hydrogen fuel cells" is the most well-known name for this device.

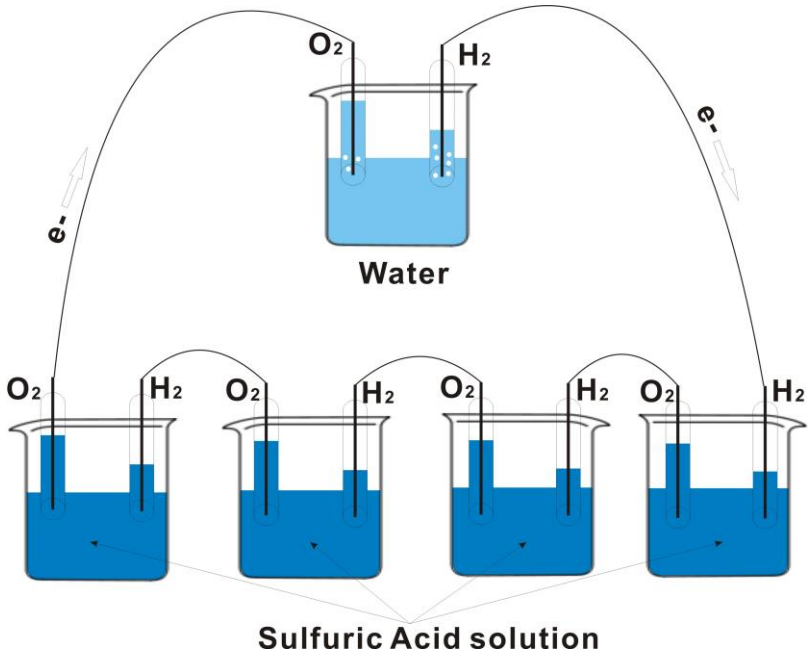

Fig. 1.1 A schematic diagram of gas voltaic battery by Dr. William Grove. [8]

From then, based on Dr. Grove's achievement, several different type of fuel cells were developed. Generally, the fundamental principle for all of them is the same, which is consuming hydrogen and oxygen, then generate electricity. Therefore, with different design in the electrolyte, different types of fuel cells can work in various conditions, and the selection in the fuel, electrode, catalyst and sealing material can be also different. There are six types of fuel cells with different working temperature; polymer electrolyte fuel cells (PEFCs, 80 ºC), alkaline fuel cells (AFC, 50 ºC -200 ºC), phosphoric acid fuel cells (PAFC, 80 ºC -90 ºC), molten carbonate fuel cells (630 ºC -650 ºC) and solid

oxide fuel cells (SOFC 600 ºC -1000 ºC). The working condition, fuel, electrolyte and catalyst of different type of fuel cells were summarized and are listed in Table 1.1. Different types of fuel cells were fully introduced individually in the following section.

Table 1.1 Different types of fuel cells

	electrolyte	fuel	catalyst	Working temperature (ºC)
PEFC	PEM	H_2	Pt	< 100
AFC	aqueous KOH	H_2	Ni, Ag	< 100
MCFC	carbonate salt	CH_4, H_2, CO	Ni-Cr/Ni-Al	~650
PAFC	liquid phosphoric acid	H_2, CH_4	Pt, Ru	~200
SOFC	solid oxide	CH_4, H_2, CO	Ni	550-950

1.2.1 Alkaline fuel cells (AFCs) [9]

AFCs are fuel cells which commonly use an aqueous alkaline solution as an electrolyte, such as potassium hydroxide (KOH) solution, and the typical structure is shown as Fig. 1.2. The first AFC was developed by Francis Thomas Bacon, a British inventor. NASA used alkaline fuel cells since the mid-1960s. It was used in Apollo-7 Space Shuttle as an electricity generator. Each electrode reactions and overall reaction are listed below.

Anode reaction : $H_2 + 2\ OH^- \rightarrow 2\ H_2O + 2\ e^-$

Cathode reaction : $1/2\ O_2 + H_2O + 2\ e^- \rightarrow 2\ OH^-$

Over all reaction : $H_2 + 1/2\ O_2 \rightarrow H_2O$

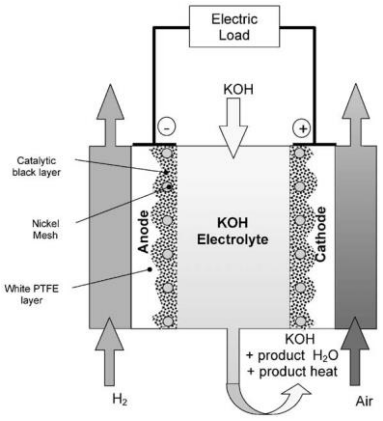

Fig. 1.2 A schematic of working principle of AFCs.
(Reproduced from ref. [9] with permission)

With a proper design in AFCs system, theoretical efficiency can reach 70 % with a working temperature below 100 ºC. Since the electrolyte is aqueous KOH solution, and Pt catalyst can be replaced by Ni-based or Cu-based alloy. Therefore, the building cost can be low. However, the electrolyte, which is alkaline solution, easily reacts with CO_2 gas and forms the metal-based chemical precipitation. Leading to the blockage in the porous media and then the low efficiency. The purification in the cathode fuel, such like removing CO_2 and NO_x gas or usage of pure oxygen is necessary for the system design.

1.2.2 Phosphoric acid fuel cells (PAFCs) [10]

PAFCs are fuel cells that use liquid phosphoric acid as an electrolyte, and the typical structure is shown as Fig. 1.3. The operating temperature of PAFC is typically between 150 °C and 200 °C. The operating temperature is found to be a compromise between the electrolyte conductivity (increase with increasing temperature) and the PAFC life time (decrease with increasing temperature). In contrast to AFCs, there is no fuel limitation in PAFCs system. Natural gas or petroleum gas with CO_2 content can be directly used as a fuel, and air can be directly used as oxidant in the cathode. The first commercial operating PAFCs power plant was built at 1970s. Until now, more than 500 PAFCs power plant are operating around the world. Each electrode reactions and overall reaction are listed below.

Anode reaction : $H_2(g) \rightarrow 2\ H^+ + 2\ e^-$

Cathode reaction : $1/2\ O_2(g) + 2\ H^+ + 2\ e^- \rightarrow H_2O$

Over all reaction : $H_2 + 1/2\ O_2 \rightarrow H_2O$

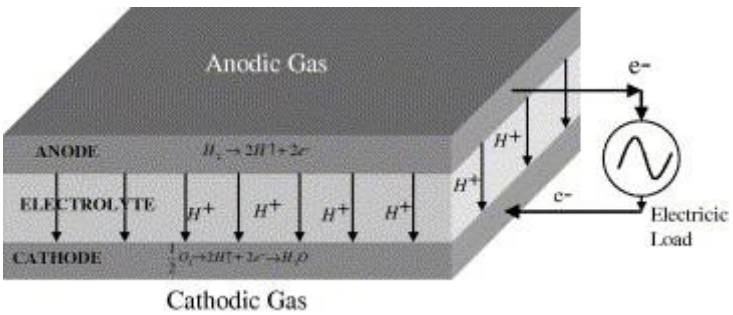

Fig. 1.3 A schematic of working principle of a PAFC.
(Reproduced from ref. [10] with permission)

The power efficiency of PAFCs stack can reach 40 % in practical operating, and

can further achieve 80 % in the total efficiency by combining with gas turbine. One major issue of PAFCs system is the catalyst poisoning. The usage of petroleum fuel in the cathode is accompanied with CO gas, which causes Pt catalyst poisoning. Pt-Ru alloy is used to deal with this issue.

1.2.3 Molten carbonate fuel cells (MCFCs) [11]

MCFCs are high-temperature fuel cells that operate at temperatures around 600 °C, and the typical structure is shown as Fig. 1.4. The molten carbonate salt is used as electrolyte. Like the acid-based electrolyte of PAFCs, there is almost no limitation in the fuel selection in MCFCs. Natural gas and biogas can be used as fuels for MCFCs. Because of the high operating temperature, catalysts are not limited in Pt-based metals. Ni-based non noble metal can be used as a catalyst. Each electrode reactions and overall reaction are listed as below. Hydrogen from fuel reacts with carbonate ions in the electrolyte, and then generates carbon dioxide and water in the anode. In the cathode reaction, oxygen reacts with carbon dioxide from the air, generates carbonate ions, and then turns into the molten carbonate salt.

Anode reaction : $H_2(g)+CO_3^{2-} \rightarrow H_2O + CO_2 + 2\ e^-$

Cathode reaction : $1/2\ O_2(g) + CO_2 + 2\ e^- \rightarrow CO_3^{2-}$

Over all reaction : $H_2 + 1/2\ O_2 \rightarrow H_2O$

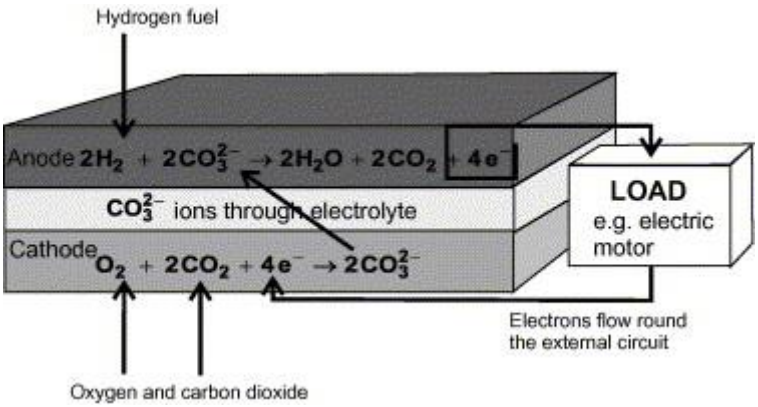

Fig. 1.4 A schematic of working principle of a MCFC.
(Reproduced from ref. [11] with permission)

Because of the high operation temperature, PAFCs can reach 60% efficiency, considerably higher than the 37–42% efficiencies of PAFCs plant. By combining with

the gas turbine, the total heat efficiency can further reach to as high as 85 %.

MCFCs don't require an external reformer to convert petroleum fuels to hydrogen. Due to the high operating temperatures, these fuels are internally converted to hydrogen within the fuel cell system.

1.2.4 Solid oxide fuel cells (SOFCs) [12] [13]

SOFCs are fuel cells that use ZrO-based materials as the electrolyte, and the typical structure is shown as Fig. 1.5. The electrolyte start showing oxygen ionic conductivity over 500 ºC. Further heating to over 800 ºC is necessary to achieve the usable ionic conductivity. Because of the high operation temperature, SOFCs neither have limitation in fuel selection nor need Pt as a catalyst. SOFCs can achieve high efficiency with Ni-based catalyst. Recycling of the waste heat leads to the highest efficiency among all fuel cells. Each electrode reactions and overall reaction are listed below.

Anode reaction : $H_2 + O^{2-} \rightarrow H_2O + 2\ e^-$

Cathode reaction : $1/2\ O_2 + 2\ e^- \rightarrow O^{2-}$

Over all reaction : $H_2 + 1/2\ O_2 \rightarrow H_2O$

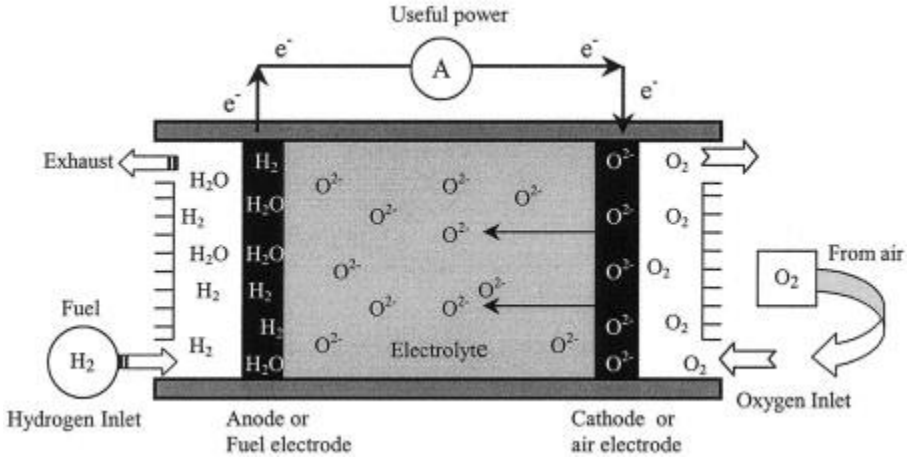

Fig. 1.5 A schematic of working principle of a SOFC.
(Reproduced from ref. [12] with permission)

All components of SOFCs, including the anode, cathode and electrolyte, are mainly consisted of ion conductive ceramics. The electrode in the anode is usually made with high electronic conductive metallic Ni. In the cathode side, the electrode is usually

made with highly stable perovskite type ceramic, such as $La_{0.6}Sr_{0.4}Co_{0.2}Fe_{0.8}O_x$-based material.

1.3 Polymer electrolyte fuel cells (PEFCs)

1.3.1 History of PEFCs

PEFCs is a type of fuel cells using a polymer electrolyte membrane. In 1960s, Dr. Thomas Grubb and Dr. Leonard Niedrach from General Electric [14] developed PEFCs for NASA's piloted space program in order to increase the duration of the power source. In the GE's model, a sulfonated polystyrene membranes was used as an electrolyte. After 1966, a membrane with high durability and low electronic resistance, Nafion®, was developed by Dr. Walther Grot at DuPont, and then Nafion® became the most widely used polymer electrolyte membrane until now.

In the beginning, PEFCs was designed as power supply only for the special purpose, the cost price was extremely high owing to the large amount of usage of noble metal catalysts. In Japan, PEFCs have been commercialized as residential fuel cells since 2011 [15] and fuel cell vehicles [16] since 2016.

1.3.2 Working principle of PEFC

The fundamental design of a typical PEFC single cell is shown as Fig. 1.6. A single cell consists of two current collectors (bipolar plates), two gas flow channel plates, and one membrane electrode assembly (MEA). MEA is made with two gas diffusion layers (two pieces of carbon paper), two catalyst layers, and proton exchange membrane (PEM, Nafion). The total thickness for a typical MEA is about 100 μm. Within a MEA, the gas diffusion layers work as micro-flow channels to provide uniform diffusion of reactant gases, and also work as a current collector for conducting the electricity from the catalyst layer. Half-cell reactions in the anode and the cathode and the total reaction are describe as follow;

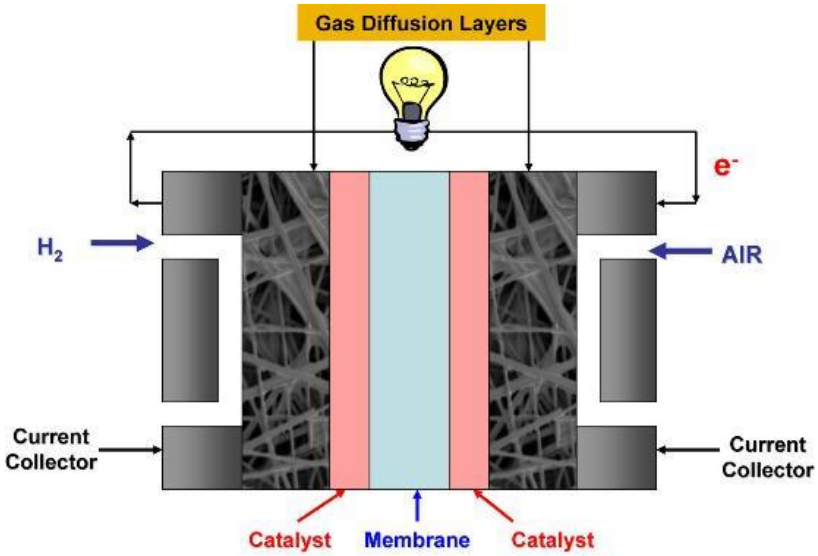

Fig. 1.6 A scheme diagram showing working principle of PEFCs.

Anode reaction : $H_2 \rightarrow 2\ H^+ + 2\ e^-$

Cathode reaction : $1/2\ O_2 + 2\ H^+ + 2\ e^- \rightarrow H_2O$

Overall reaction : $H_2 + 1/2\ O_2 \rightarrow H_2O$

First, in the anode, hydrogen oxidation reaction (HOR) makes the hydrogen gas oxidized to two protons and two electrons. Protons transport to the cathode through PEM, and electrons can be collected and utilized as electricity. In the cathode, protons came through PEM and electrons from the external electricity circuit react with oxygen and then generate water and heat, which is called oxygen reduction reaction (ORR). In the total reaction, hydrogen and oxygen are consumed and then water and heat are produced.

The possible energy generates from hydrogen fuel can be explained by using Nernst theory. According to the theory, for a electrochemical reaction $Ox + ne^- \rightarrow Red$, the changing in Gibbs free energy (ΔG) is described as eq. (1.1).

$$\Delta G = \Delta G^0 + RT\ \ln Q_r \qquad (1.1)$$

, where ΔG^0 is the changing in Gibbs free energy under the standard state condition,

R is universal gas constant, 8.314 J K^{-1} mol^{-1},

T is temperature in Kelvin, and

Q_r is the reaction quotient, also addressed as $\alpha_{red}/\ \alpha_{ox}$, where α is the chemical activity for the relevant species).

The cell potential E also associated with the electrochemical reaction is defined as

the decrease in Gibbs free energy per coulomb of charge transferred, leading to the relationship as describe in eq. (1.2).

$$\Delta G = -nFE \tag{1.2}$$

, where E is the theoretical cell open-circuit-voltage (OCV, V) from the reactant and product,

n is the number of transfer electron for generating a water molecular (n = 2 in this reaction), and

F is the Faraday constant (96500 C mol^{-1}).

The eq. (1.1) can be further expressed as eq. (1.3).

$$E = E^0 - \frac{RT}{2F} \ln \frac{\alpha_{red}}{\alpha_{ox}} \tag{1.3}$$

Under the steady state condition, eq. (1.3) can be written as

$$E = E^0 - \frac{RT}{2F} \ln \frac{P_{H_2} {P_{O_2}}^{1/2}}{P_{H_2O}} \tag{1.4}$$

for the fuel cell

, where p is the partial pressure of each element in the fuel cell.

The reversible potential (E^0) can be correlated with working temperature (K) by eq. (1.5).

$$E^0 = 1.518 - 1.542 \times 10^{-3}T + 9.52 \times 10^{-5}T \times \ln T + 9.84 \times 10^{-8}T^2 \tag{1.5}$$

When PEFCs operate at 80 ºC, the fuel gases in the anode and the cathode are pure hydrogen and oxygen, respectively, and the saturated water vapor pressure at 80 ºC is 0.467 atm, according to eq. (1.5), the reversible potential becomes 1.183 V. However, in the practical fuel cell, measured OCV is usually lower than the theoretical OCV, suggesting to the voltage drop caused by internal crossover of fuel gas or electrons. The OCV measured experimentally is usually between 0.9 to 1.0 V.

Fig. 1.7 shows a typical IV performance curve of PEFCs. Along with increasing in the current output, the decrease in cell voltage can easily be found. The voltage drop in the IV curve can be divided into 3 regions. Rapid drop in high voltage zone is called activation overvoltage (or activation polarization). Linear drop in the middle voltage area is called ohmic overvoltage (or ohmic polarization). Another rapid drop in the low voltage region is called concentration overvoltage (or mass transfer loss, concentration polarization).

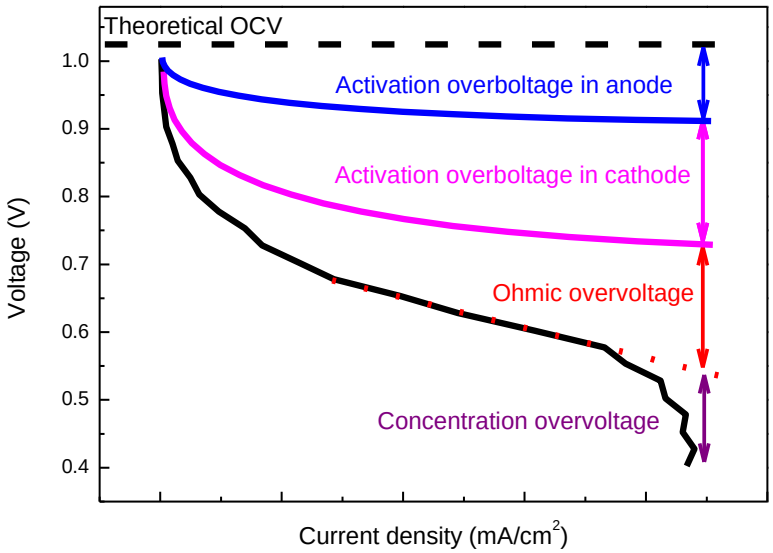

Fig. 1.7 A typical IV performance curve of PEFCs.

In the activation overvoltage region, the voltage drop is dominated by the activation energy of the electrochemical reaction, which is used to overcome the reaction energy barrier.

Ohmic overvoltage comes from electronic resistance of components of MEAs. Among components in MEAs, the resistance from PEM takes the largest part of total ohmic resistance because of electronic insulator. According to the study [17], Nafion 212 membrane operating under 80 ºC with RH. 98% has a proton conductivity of 98 mS-cm. Along with the membrane thickness of Nafion 212 (50 μm), the theoretical ohmic resistance of PEM is about 51 mΩ.

Regarding to the concentration overvoltage, the deficiency of reactants on the catalyst surface is a reason for this voltage drop. Also unsuccessful removal of produced water, flooding, is also the reason for concentration overvoltage.

1.3.3 Advantages and critical issues for PEFC

PEFCs have several advantages as power sources.

- Almost no pollutants are exhausted from PEFCs.
- Hydrogen fuel can be acquired from varies of sources.

- Easier system design is expected with solid membrane.
- Rapid start up/shut down is possible under the operation temperature of PEFCs below 100 ºC.

However, full worldwide commercialization of PEFCs, there are two major issues to be overcame, cost and durability.

- Cost

The building cost of a PEFC stack is usually come from MEA components [18] [19], which are made from the Nafion® membrane and electrocatalysts, Pt or Pt-related noble metal catalysts. In recent year, studies in replacing pure Pt catalyst with Co-based or Ni-based alloy [20] [21] or in developing no-precious metal catalysts [22] [23] get more and more attention.

Besides electrocatalysts themselves, improvement in PEFCs performance through controlling the structure of catalyst layers has been studies. Basically, to achieve high performance, designing 3-phase boundary (ionomer, Pt/Carbon, and reactant) within the catalyst layer is important. The conventional MEA preparation is based on the coating of ink slurry. The isolation of Pt particles due to the disordered structure of catalyst layers has been reported [24]. To achieve high performance MEA, the controlling in μm-scale structure is necessary.

- Durability

The electricity output of a PEFC stack decreases along with operating time mostly due to the degradation of catalyst layers, which comes from the corrosion of carbon supports and the loss of active surface area of Pt particles. According to the study [25], the enlargement in Pt particle size was found by TEM during the long time operation process. According to another study [26], the movement of Pt particles was directly observed during the accelerated degradation by using in-situ STEM. Therefore, the degradation of Pt catalyst can mainly be explained by migration, agglomeration, and detachment [27].

- Regarding to migration, due to the weak interaction between Pt particles and the supporting material, Pt particles tend to diffuse toward to the lower surface potential energy way. Small particles easily get close to each other to reduce the surface area.
- For agglomeration, with a same reason to the migration, the agglomeration of

Pt particles usually happens when Pt particles are ionized (dissolved) into the electrolyte during the electrochemical reaction. Pt ions tend to re-precipitate on other Pt particles, resulting in increase in the particle size.

- About detachment, as Pt particles reach a certain size, the interaction between the support and Pt particles becomes not enough, and leading the detachment of particles.

1.4 Carbon support in catalyst layer of PEFCs

1.4.1 Carbon support in general

Among the catalyst layer, a carbon support plays one of important roles to provide good electronic conductivity, good 3-phase boundary with Pt particles, and better resistance against the acidic environment for improving of the performance and durability of PEFCs.

As prominent supports for precious metal catalysts, carbon materials have various festinating features. In general, carbon materials can practically be used in both acidic and basic environments, and their large surface area leads to good dispersion of catalytic metal particles to improve the metal utilization [28][29][30]. These are essential properties as a catalyst support for PEFCs. In the past few decades, lots of commercial-available carbon substrates, such as activated carbon [31] and carbon black with large surface area and good electronic conductivity, were utilized as catalyst supports in PEFCs.

On the other hand, the working environment for PEFCs usually accompanies with high temperature, high humidity, low pH condition. Frequent voltage change is applied on the catalyst support. All these conditions lead to the corrosion of carbon supports.

Besides carbon corrosion, the weak interaction Pt particles metal and disordered μm-scale structure as catalyst layer are critical issues and the possible strategies were discussed as follows.

For the enhancement of increase in the interaction between the carbon support and Pt particles, introducing extra atoms, such as nitrogen atoms, as anchor points was considered, leading to the improvement in durability [32]. Also, when carbon materials are partially or fully graphitized, they increased electrical conductivity and durability against corrosion of carbon [33]. Adding extra coating layers, such like poly(diallyldimethylammonium chloride) [34], polybenzimidazole (PBI) [35], or Nafion ionomer [36], onto the surface of carbon and Pt particles led to increase in the durability and catalytic activity.

1.4.2 Mesoporous carbon (MC)

Among varies carbon materials, MC has been focused on because of several benefits, such as large surface area from the porous structure. For the synthesis of MC, it can mainly be divided into two different types of the template. There are several group working on synthesis of MC by using hard templates as precursor, such like micro silica balls [38], metal [39], or metal oxide [40]. With a hard template as a pore inducer, pores can be easily controlled by changing the template size. However, the extra process of removing the hard template is needed. For example, hydrofluoric acid is needed for removing of silica templates.

Another type is called a soft template method. Synthesis of mesoporous carbon via the organic-organic self-assembly process was developed by Dr. Tanaka [41]. Generally, this synthesis is based on the phase separation in mixture of hydrophobic and hydrophilic solution. In a normal case, hydrophilic molecules tend to stay close with other hydrophilic molecules. However, with adding surfactant molecules containing both hydrophilic and hydrophobic functional groups, the homogenous phase in the mixture solution can be achieved. Hydrophobic molecules and hydrophilic molecules can form stable micelles in the solution as shown in Fig. 1.8.

In the synthesis of mesoporous carbon, this kind of micelles made from hydrophilic carbon precursor molecular and hydrophobic surfactant phase is used as a pore inducer. After N_2 calcination process, the micelle core (blue area in the Fig. 1.8), mainly consisted of hydrophobic surfactant, is removed, the hydrophilic phase (brown area in the Fig. 1.8), consisted of resorcinol-formaldehyde, is carbonized, resulting in the mesoporous structure.

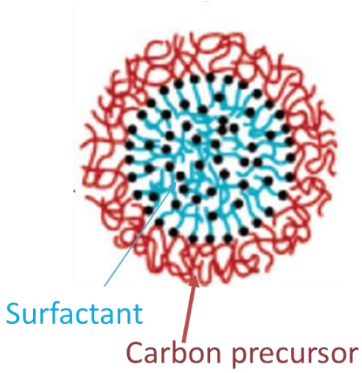

Fig. 1.8 A schematic diagram of F127 micelles in MC precursors.

1.4.3 Carbon nanofibers (CNFs)

For designing three dimensional structure of catalyst layers by carbon, the idea from controlling μm-scale electrode structure in supercapacitor [42] [43] and in Li-S battery [44] can be applied to catalysts of PEFCs. Fiber-like structure, such like carbon nanotube (CNT) and carbon fibers, can provide control of macrostructure of catalyst layers.

Despite the fact that CNF or CNT can provide a certain benefit on formation of three dimensional structure of catalyst layers because of the partially controlled fiber-like macrostructure, development of catalyst layers are still rely on the similar ink process used for other powder-based carbon materials. Consequently, disorderness of the macrostructure, such as the isolation of particles, cannot be avoided.

1.5 Electrospinning deposition (ESD) in PEFCs

Electrospinning deposition (ESD) is a technique that can produce fibers from the solution, and electronically conductive polymer fibers have been used as electrodes for various energy devices, such as fuel cells, solar cells, Li-ion batteries. It is reported that polyaniline nanofibers with Pt particle encapsulated were used as a catalyst for PEFC [45], and improved IV performance owing to increase in conductivity was achieved. ESD can also be used to produce metal fibers. Cu fibers made by ESD revealed the self-standing film with good elasticity and excellent electronic conductivity, and were used as electrodes for solar cell [46]. Furthermore, carbon fibers can also be achieved by using polymers with high carbon content ratio, such as polyacrylonitride, and high temperature carbonization, and the improved conductivity of ESD-made carbon fibers was also reported [47].

Since the precursor of MC materials, as known as the resorcinol-based resin, is often used as the precursor material of ESD-made carbon fibers [48], the possibility of making MC fibers by ESD has been considered. Wang et al.[49] provided a way to make carbon fibers with mesopores of 6 nm with the solution containing carbon and silica precursors, but an extra procedure of removing the silica hard template by HF was required. Ma et al. [50] provided a synthesis process of mesoporous carbon fibers, whose pore volume was easily tuned by changing the reactant ratio. However, the mesopore diameter from the KOH molecule was mostly below 1 nm, which was not suitable for the extra metal impregnation. Ozaki et al.[51] provided a synthesis method for making carbon fibers with mesopores, named as activated carbon fibers (ACF), by

using the polymer blend and a regular spinning process. The mesopores in the ACF were formed by the decomposition of the polymer blend of additive PVB, and the largest pores size reached 8 nm. However, without organic-organic self-assembly, the pores size derived by the polymer blend was hard to be controlled.

1.6 Objective

1.6.1 Background of this study

Durability issues of PEFCs have been focused on from the side of carbon support in Hayashi research group. In order to improve the durability of Pt on the carbon support, increase in the physical interaction between carbon and Pt particles have been started.

Since the mobility of particles is known to decrease when particles are deposited onto the surface with larger curvature both theoretically and experimentally [37], the same concept was applied by using mesoporous carbon (MC). Encapsulation of Pt into mesopores was tried in order to reduce the mobility of Pt particles.

Hayashi group started the fundamental research in utilizing the MC as catalyst support of PEFC since 2008 [52], such results indicated that Pt particles within mesopores had a certain level of ORR activity and had a potential to be used as catalyst in PEFC. Followed by studies in 2009, the well dispersion of Pt nanoparticles in MC [53] and the oxygen transport mechanism within mesopores [54] were found. Those results provided the cornerstone of the way of utilizing MC as a catalyst support in the cathode. In 2014, MEAs for PEFC was made with MC-supported catalyst in the cathode, and the improvement in IV performance after long-term durability test was also reported [55]. However, the initial current density at 0.6 V of MEA made with MC-based cathode was around 480 mA/cm^2, which was slightly low as comparing with MEA made with conventional TKK 46 wt.% Pt/KB cathode. The lower IV performance of MEA made with MC-based cathode mostly came from the disorder structure in μm-scale, resulting in higher ohmic resistance and mass transfer resistance [56]. Consequently, even though microstructure of the carbon support was successfully controlled, macrostructure of the catalyst layer was not successful and became an issue to be overcame.

1.6.2 Object of this study

Based on previous studies explained in the above, improvement on IV performance of MC with controlled microstructure and macrostructure, was aimed in this study, and a schematic image of the aimed structure is shown in Fig.1.9. As mentioned in section 1.4.3, the fiber structure provides good electronic conductivity and mechanical strength, three dimensional structure, and so fiber structure was combined with MC. In this study, development of MC fibers (MCFs) was aimed by combining the organic-organic self-assembly synthesis and ESD. Then, MCFs were

applied as the cathode of PEFC in order to improve IV performance.

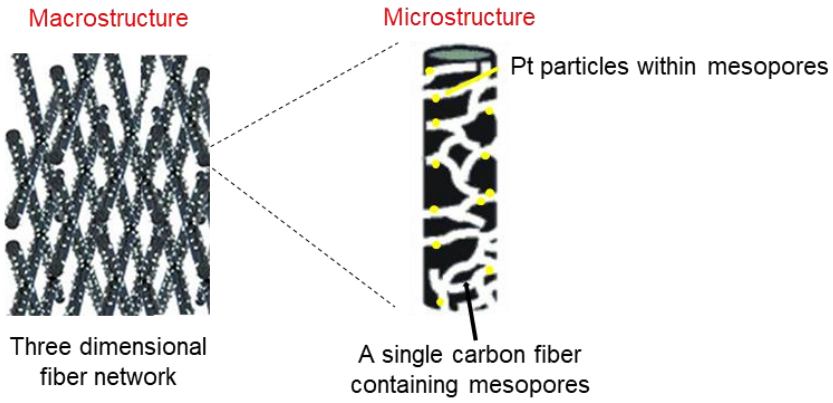

Fig. 1.9 A schematic drawing of controlled microstructure and macrostructure aimed in this study

The research approach are shown and explained in Fig. 1.10.

As a first step, optimization of synthesis process of MCFs as tried. ESD conditions, such as selecting the liner additive, reactant ratio, polymer concentration, working distance, working voltage and current, temperature, and humidity, were considered, while materials were fully characterized. The first goal was set to controlling of mesoporosity of MCFs, including mesopores volume and diameter.

For the next step, to utilize as a catalyst for PEFC, Pt deposition on MCFs materials was proceeded in both milled MCFs and MCF sheet. As primary characterizations, the amount of wt.% Pt and morphology of Pt/MCFs were evaluated. Also, fundamental electrochemical characterizations, including electrochemical active surface area (ECSA) and ORR activity, were evaluated. The second goal was set to obtaining comparative ORR activity to conventional TKK 46 wt.% Pt/KB catalyst.

As the last step of this study, MEAs made with milled Pt/MCFs catalysts were prepared and their IV performance was evaluated. Then, MCF sheet, without ball-milling, was introduced as the cathode catalyst layer, in order to achieve the final goal of this research: Developing the catalyst layer with controlled structure in both μm-scale and nm-scale for improving IV performance.

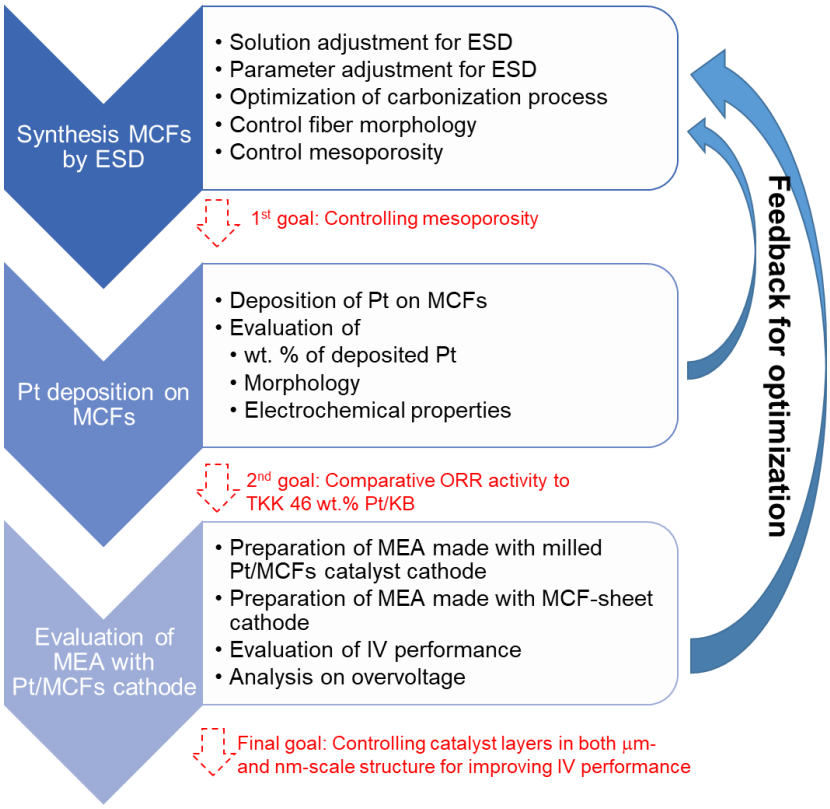

Fig. 1.10 Research approach in this study.

List of references

[1] P. M. Cox, R. A. Betts, C. D. Jones, S. A. Spall, I. J. Totterdell, Acceleration of global warming due to carbon-cycle feedbacks in a coupled climate model, Nature, **408**, 184-187 (2000).

[2] B. C. O'Neill, M. Oppenheimer, Dangerous climate impacts and the Kyoto protocol, Science,**14** (296), 1971-1972 (2002)

[3] K. Dinkler, J. Peterseim, Battery augmented biomass and waste power plants – A new approach to provide grid services, VGB PowerTech, **1/2,** 66-69 (2019).

[4] K. H. Yang, R. L. Hwang, Energy conservation of buildings in Taiwan, Pattern Recogn., **28** (10), 1483-1491 (1995).

[5] 環境省, 再エネ水素を活用した社会インフラの低炭素化促進事業, https://www.env.go.jp/air/car/lev/hydro_st.html, Accessed 2020/06/07 .

[6] C. K. Dyer, Fuel cells for portable applications, J. Power Sources, **106** (1), 31-34 (2002)

[7] R.O 'Hayre *et al.,* Fuel cell fundamentals, John Wiley & Sons, (2005).

[8] W.R. Grove, On a gaseous voltaic battery, The London, Edinburgh, and Dublin Philosophical Magazine and Journal of Science, **21** (140), 417-420 (1842).

[9] G.F. McLean, T. Niet, S. Prince-Richard, N. Djilali, An assessment of alkaline fuel cell technology, Int. J. of Hydrogen Energ. **27**, 507-526 (2002).

[10] N. Sammes, R. Bove, K. Stahl, Phosphoric acid fuel cells: Fundamentals and applications, Solid State and Mater. Sci., **8**, 372-378 (2004)

[11] A. L. Dicks, Molten carbonate fuel cells, Solid State and Mater. Sci., **8**, 379-383 (2004).

[12] A.B. Stambouli, E. Traversa, Solid oxide fuel cells (SOFCs): a review of an

environmentally clean and efficient source of energy, Renew. Sust. Energ. Rev., **6** (5), 433-455 (2002).

[13] S.C. Singhal, Advances in solid oxide fuel cell technology, Solid State Ionics, **135**, 305-313 (2000).

[14] M. L. Perry, T. F. Fuller, A historical perspective of fuel cell technology in the 20th century, J. Electrochem. Soc., **149** (7), S59-S67 (2002).

[15] S. Nižetić, I. Tolj, A.M. Papadopoulos, Hybrid energy fuel cell based system for household applications in a Mediterranean climate, Energ. Convers. Manage., **105**, 1037-1045 (2015)

[16] R. v. Helmolt, U. Eberle, Fuel cell vehicles: Status 2007, J. Power Source, **165**, 833-843 (2007).

[17] Y. Kim, Kr. Ketpang, S. Jaritphun, J. S. Park, S. Shanmugam, A polyoxometalate coupled graphene oxide– Nafion composite membrane for fuel cells operating at low relative humidity, J. Mater. Chem. A, **3**, 8148-8155 (2015).

[18] V. Mehta, J. S. Cooper, Review and analysis of PEM fuel cell design and manufacturing, J. Power Source, **114** (1), 32-53 (2003).

[19] A. Brouzgou, S.Q. Song, P. Tsiakaras, Low and non-platinum electrocatalysts for PEMFCs: Current status, challenges and prospects, Appl. Catal. B: Environ., **127**, 371-388 (2012).

[20] H. A. Gasteiger, S. S. Kocha, B. Sompalli, F. T. Wagner, Activity benchmarks and requirements for Pt, Pt-alloy, and non-Pt oxygen reduction catalysts for PEMFCs, Appl. Catal. B: Environ., **56**, 9-35 (2005)

[21] B. Wang, Recent development of non-platinum catalysts for oxygen reduction reaction, J. Power Source, **152**, 1-15 (2005).

[22] P. H. Matter, L. Zhang, U. S. Ozkan, The role of nanostructure in nitrogen-containing carbon catalysts for the oxygen reduction reaction, J. Catal., **239**, 83-96 (2006).

[23] Z. Chen, D. Higgins, A. Yu, L. Zhang, J. Zhang, A review on non-precious metal electrocatalysts for PEM fuel cells, Energy Environ. Sci., **4**, 3167-3192 (2011).

[24] C. Wang, M. Waje, X. Wang, Ja. M. Tang, R. C. Haddon, Y. Yan, Proton exchange membrane fuel cells with carbon nanotube based electrodes, Nano Lett., **4** (2), 345-348 (2004).

[25] Y. Zhai, H. Zhang, D. Xing, Z.-G. Shao, The stability of Pt/C catalyst in H3PO4/PBI PEMFC during high temperature life test, J. Power Source, **164**, 126-133 (2007)

[26] A. Hayashi, Studies on degradation mechanism of electrocatalysts for fuel cells through in-situ sem/stem observation, Hitachi Review, **65** (7), 196-200 (2016).

[27] J. Wu, X. Z. Yuan, J. J. Martin, H. Wang, J. Zhang, J. Shen, S. Wu, W. Merida, A review of PEM fuel cell durability: Degradation mechanisms and mitigation strategies, J. Power Source, **184**, 104-119 (2008).

[28] E. Auer, A. Freund, J. Pietsch, T. Tacke, Carbons as supports for industrial precious metal catalysts, Appl. Catal. A: Gen., **173**, 259-271 (1998).

[29] F. Rodriguez-Reinoso, The role of carbon materials in heterogeneous catalysis, Carbon, **36 (**3), 159-175 (1998).

[30] P. Serp, M. Corrias, P. Kalck, Carbon nanotubes and nanofibers in catalysis, Appl. Catal. A: Gen., **253**, 337-358 (2003).

[31] H. Jiintgen, Activated carbon as catalyst support: A review of new research results, Fuel, **65**, 1436-1446 (1986).

[32] H. Lv, N. Cheng, S. Mu, M. Pan, Heat-treated multi-walled carbon nanotubes as durable supports for PEM fuel cell catalysts, Electrochim. Acta, **58**, 736-742 (2011).

[33] Y. Shao, G. Yin, Y. Gao, Understanding and approaches for the durability issues of Pt-based catalysts for PEM fuel cell, J. Power Source, **171**, 558-566 (2007).

[34] Y. Shao, S. Zhang, R. Kou, X. Wang, C. Wang, S. Dai, V. Viswanathan, J. Liu, Y. Wang, Y. Lina, Noncovalently functionalized graphitic mesoporous carbon as a stable support of Pt nanoparticles for oxygen reduction, J. Power Source, **195**, 1805-1811 (2010).

[35] M. R. Berber, I. H. Hafez, T. Fujigaya, N. Nakashima, Durability analysis of polymer-coated pristine carbon nanotube-based fuel cell electrocatalysts under non-humidified conditions, Mater. Chem. A, **2**, 19053-19059 (2014)

[36] N. Cheng, S. Mu, M. Pan, P. P. Edwards, Improved lifetime of PEM fuel cell catalysts through polymer stabilization, Electrochem. Commun., **11**, 1610-1614 (2009).

[37] A. Staykov, Y. Ooishi, T. Ishihara, Immobilizing metal nanoparticles on single wall nanotubes. effect of surface curvature, J. Phys. Chem. C, **118**, 8907−8916 (2014).

[38] J. Lee, S. Han, T. Hyeon, Synthesis of new nanoporous carbon materials using nanostructured silica materials as templates, J. Mater. Chem., **14**, 478-186 (2004).

[39] Y. Huang, S. Hu, S. Zuo, Z. Xu, C. Hana, J. Shen, Mesoporous carbon materials prepared from carbohydrates with a metal chloride template, J. Mater. Chem., **19**, 7759–7764 (2009).

[40] B. Xu, L. Peng, G. Wang, G. Cao, F. Wu, Easy synthesis of mesoporous carbon using nano-CaCO3 as template, Carbon, **48**, 2361-2380 (2010).

[41] S. Tanaka, N. Nishiyama, Y. Egashira, K. Ueyama, Synthesis of ordered

mesoporous carbons with channel structure from an organic–organic nanocomposite, Chem. Commun., 2125–2127 (2005).

[42] Q. Wang, J. Yan, Z. Fan, Carbon materials for high volumetric performance supercapacitors: design, progress, challenges and opportunities, Energy Environ. Sci., **9**, 729-762 (2016).

[43] L. L. Zhang, X. S. Zhao, Carbon-based materials as supercapacitor electrodes, Chem. Soc. Rev., **38**, 2520–2531 (2009).

[44] J. Liang, Z.-H. Sun, F. Li, H.-M. Cheng, Carbon materials for Li–S batteries: Functional evolution and performance improvement, Energy Storage Mater., **2**, 76-106 (2016).

[45] V. Thavasi, G. Singh, and S. Ramakrishna, Electrospun nanofibers in energy and environmental applications, Energy Environ. Sci., **1**, 205-221 (2008).

[46] Hui Wu *et al.*, Electrospun metal nanofiber webs as high-performance transparent electrode, Nano Lett., **10**, 4242-4248 (2010).

[47] M. Inagaki, Y. Yang, F. Kang, Carbon nanofibers prepared via electrospinning, Adv. Mater., **24**, 2547-2566 (2012).

[48] Y. Badhe and K. Balasubramanian, Nanoencapsulated core and shell electrospun fibers of resorcinol formaldehyde, Ind. Eng. Chem. Res., **54**, 7614-7622 (2015).

[49] H. Wang, C. Zhang, Z. Chen, H. K. Liu, Z. Guo, Large-scale synthesis of ordered mesoporous carbon fiber and its application as cathode material for lithium–sulfur batteries, Carbon, **81**, 782-787 (2015).

[50] C. Ma, Y. Song, J. Shi, D. Zhang, X. Zha, M. Zhong, Q. Guo, L. Liu, Preparation and one-step activation of microporous carbon nanofibers for use as supercapacitor electrodes, Carbon, **51**, 290-300 (2013).

[51] J. Ozaki, N. Endo, W. Ohizumi, K. Igarashi, M. Nakahara, A. Oya, Novel preparation method for the production of mesoporous carbon fiber from a polymer blend, Carbon, **35** (7), 1031-1033 (1997).

[52] A. Hayashi, H. Notsu, K. Kimijima, J. Miyamoto, I. Yagi, Preparation of Pt/mesoporous carbon (MC) electrode catalyst and its reactivity toward oxygen reduction, Electrochim. Acta, **53**, 6117-6125 (2008).

[53] A. Hayashi, K. Kimijima, J. Miyamoto, I. Yagi, Direct observation of well-dispersed pt nanoparticles inside the pores of mesoporous carbon through the cross section of pt/mesoporous carbon particles, Chem. Lett., **38** (4), 346-347 (2009).

[54] A. Hayashi, K. Kimijima, J. Miyamoto, I. Yagi, Oxygen transfer and storage processes inside the mesopores of platinum-deposited mesoporous carbon catalyst thin-layer electrode, J. Phys. Chem. C, **113**, 12149–12153 (2009).

[55] Y. Minamida, Z. Noda, A. Hayashi, Development of MEAs with Pt/mesoporous carbon as a cathode catalyst, ECS Transactions, **64** (3), 137-144 (2014).

[56] 南田靖人、修士論文（H26 年）

CHAPTER 2

Experimental Method

Chapter 2 : Experimental Method

Introduction

In this chapter, experimental procedures used in this study were fully introduced. This chapter was separated into four sections, 2.1 material synthesis, 2.2 characterization methods, 2.3 fundamental electrochemical characterization, and 2.4 preparation and evaluation of membrane electrode assemblies (MEAs)

2.1 Material syntheses

2.1.1 Chemicals used in this study

All the chemicals were used as received without further purification. Resorcinol, phloroglucinol dihydrate, ethanol (99.5 purity), 5 M HCl, triethyl orthoacetate (EOA), formaldehyde solution, 2-propanol, sodium hydroxide (tablet), 20 % ammonia solution, 99.5% dichloromethane and 2-propanol (IPA), and 5 % Nafion® dispersion solution (DE520 CS type) were purchased from WAKO. Mowiol® 40-88 (Polyvinyl alcohol, PVA), Pluronic® F127, Vulcan® XC-72 carbon black and carbon nanofibers (CNF, 100 nm diameter and 10-20 mm length), Platinum(II) acetylacetonate, hexafluoro-2-propanol (hfp), 0.1 M $HClO_4$ and polyvinyl butyral (PVB, viscosity 200 mPa S) were obtained from SIGMA-ALDRICH. TEC10E50E (46 wt.% Pt/KB) was obtained from TKK Corp,. MilliQ water was used in all the experiments.

2.1.2 Synthesis of fundamental mesoporous carbon (MC)

The synthesis of MC was based on self-assembly between a co-block polymer, Pluronic F127, and a carbon precursor, resorcinol-formaldehyde resin. First, a solvent, 4.35 g of water, 5.75 g of Ethanol and 150 μl of 5M HCl were fully mixed at room temperature. Then, 1.65 g of resorcinol flake, 0.945 g of Pluronic F127, and 1.35 g of formaldehyde solution were added into the solvent in order after reagents were fully dissolved. Then, 1.35 ml of EOA was added into the solution. The solution was further mixed at 60 ºC for 3h, and then dried at room temperature overnight. At the end, the residential solution turned into bright yellow.

The solution was further dried at 105 ºC in the oven. The obtained dried solid was heated under N_2 with the heating rate of 1 ºC/min, at 400 ºC for 3h, and also at 800 ºC, for 6 h. The resulting black sample was ball-milled into μm-scale size powder to use as

a reference sample.

2.1.3 Synthesis of mesoporous carbon fibers (MCFs) precursor solution for electrospinning deposition (ESD)

2.1.3.1 MCF precursor solution with different linear additive

In order to keep the surface tension, against the strong electrostatic force during ESD. Two different commercial-available linear polymers, the polyvinyl alcohol (PVA) and the polyvinyl butyral (PVB), were used as additives to MCF precursor solution. The monomer structure of PVA and PVB are shown in Fig 2.1(a) and Fig 2.1(b), respectively.

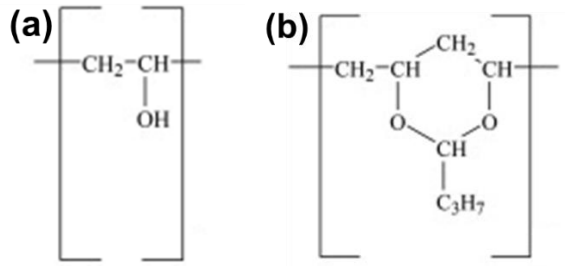

Fig. 2.1 Molecular structure of PVA (a) and PVB (b).

The first precursor solution was mixed with PVA. A typical synthesis was described as follows. First steps were the same as those of MC. The 4.35 g of water, 5.75 g of ethanol, and 150 μl of 5M HCl were fully mixed at room temperature as a solvent. Then, 1.65 g of resorcinol, 0.95 g of F127, and 1.35 g of formaldehyde solution were added into the solvent in order. Then, 1.10 g of pure PVA powder was mixed into the solution. This solution was mixed under room temperature until the PVA was fully dissolved.

The second precursor solution was mixed with PVB, similar to addition of PVA. The 1.00 g of PVB powder was mixed into the solution at room temperature until the PVB was fully dissolved.

2.1.3.2 MCF precursor solution with increase in the surfactant ratio

In addition to a typical synthesis of the precursor solution in the previous section, the weight ratio of surfactant F127/ carbon precursors was significantly increased and the weight ratio of PVA was decreased to a half. In order to obtain a stable solution,

NaOH was rather used instead of HCl. The 13 wt.% PVA solution was separately prepared by dissolving 2.60 g of PVA into 17.40 g of MilliQ water under stirring at 85 ºC for 4 h and cooled down before the use. Then, the 1.74 g of water, 2.30 g of ethanol and 187.5 µl of 1M NaOH solution were fully mixed at room temperature as a solvent. Then, 0.578 g of resorcinol, 0.80 g of F127, and 0.630 g of formaldehyde solution were added into the solvent in order. After this solution was fully mixed at 50 ºC for 80 min, 2.40 g of separately prepared 13 wt.% PVA solution was added. The solution was further mixed at 60 ºC for 1 h. The obtained precursor solution was named as MCF-B precursor solution since pH value of solution became 7.6.

2.1.3.3 MCF precursor solution with different pH conditions

MCF precursor solutions with different pH were prepared. Since in the acidic condition with HCl, the polymerization rate of the resorcinol-formaldehyde resin was significantly slower than that in the basic condition with NaOH, a slightly different chemical was used. Phloroglucinol, which molecular structure is shown in Fig 2.2 (b), has one extra hydroxyl group on its benzene ring comparing to resorcinol as shown in Fig 2.2 (a), and this extra OH group has been known to help increasing the polymerization rate even with low pH condition [1]. Therefore, phloroglucinol was used instead of resorcinol.

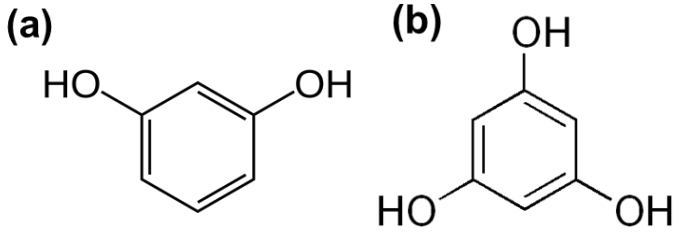

Fig. 2.2 Molecular structures of resorcinol (a) and pholoroglucinol (b).

Resorcinol was replaced by the same mole of phloroglucinol dihydrate. The 0.64 g phloroglucinol dihydrate, 0.60 g of Pluronic® F127, 0.36 g of formaldehyde solution, and 0.36 ml EOA were added in order into the solvent containing 1.20 g water, 3.45 g of ethanol, and 112.5 µl of 5 M HCl under stirring at 45 ºC for 35 min. Then, 2.70 g of PVA solution was added into the solution and continuously stirred at 45 ºC for 30 min. This precursor solution was named as MCF-A precursor solution since pH value of the solution became 3.8.

Also, in the other process, 0.60 g of phloroglucinol dihydrate, 0.60 g of Pluronic®

F127, 0.33 g of formaldehyde solution, and 0.47 ml EOA were added in order into the solvent containing 1.60 g water, 2.30 g of ethanol, and 75 μl of 5M HCl under stirring at 40 ºC, for 30 min. Then, 4.8 g of 13 wt% PVA solution and 375 μl of ammonia solution were further added and kept being stirred at 40 ºC for 30 min. This precursor solution was named as MCF-WA precursor solution since pH of the solution became 4.6.

2.1.3.4 MCF precursor solution with increase in the concentration of precursors

Typical synthesis process was based on MCF-A synthesis. Increase in the precursor concentration was also tried with the adjustment of pH. Into the solvent containing 0.60 g water and 1.73 g ethanol, 112.5 μl 5M HCl, 0.64 g phloroglucinal dihydrate, 0.60 g Pluronic® F127, 0.36 g formaldehyde, and 0.36 ml EOA were added. After mixing the resulting solution at 45 ºC for 25 min, the solution turned into bright yellow color, indicating the completion of preliminary polymerization. Then, 1.65 g of 13 wt% PVA solution was added into the solution and mixed at 45 ºC for 10 min. The obtained precursor solution was named as MCF-HC.

2.1.4 Synthesis of MCFs

2.1.4.1 ESD process

ESD is a conventional method to making polymer solution into fibers. A typical setup of vertical ESD devise is shown as Fig. 2.3. A typical device of ESD equips with a high voltage source, a grounded metal plate, a metal needle conducting high voltage, and a syringe containing polymer solutions.

During ESD, the interaction between polymer solution and high voltage is shown as Fig. 2.4. With increasing in working voltage, the polymer solution is charged by high voltage and turns into Tylor Cone owing to the strong electrostatic force against the surface tension. Once the charge voltage higher than critical voltage (V_c), polymer solution ejects from the Tylor Cone and becomes fibers. To keep the surface tension during ESD, additional large molecules of linear polymers are required in the most cases.

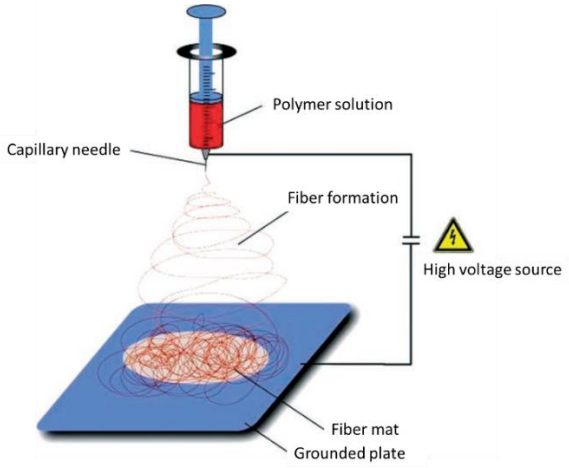

Fig. 2.3 A typical setup of vertical ESD devise [2]

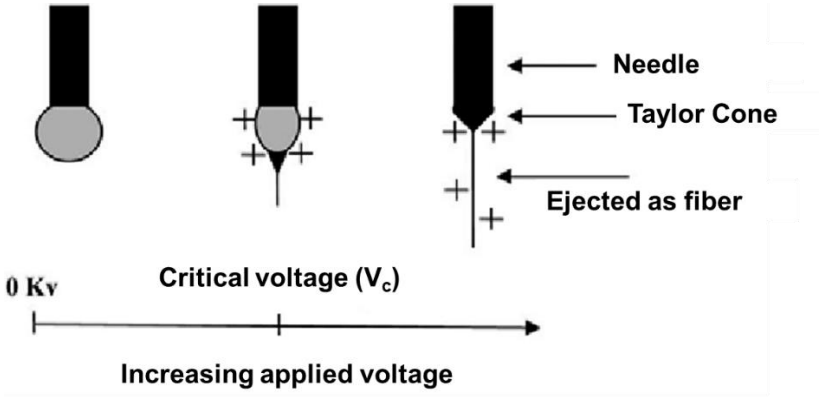

Fig. 2.4 A schemetic diagram showing interaction between the polymer solution and voltage charge during ESD.

The actual instrument setup of ESD process used in this study is shown as Fig. 2.5. The precursor solution was placed in a 8 ml disposable syringe (as seen at the left in Fig. 2.5). One end of a silicon rubber tube with internal diameter of 0.3 cm was attached to the tip of the syringe, and the other end of the silicon tube was connected to a 27G (diameter: 0.25 mm) needle by a metal adaptor. The needle was set to the holder (blue holder in Fig. 2.5) connected to ESD high voltage power supply (HVU 30P100 made by MECC) The holder with the needle was vertically arranged to the grounded aluminum foil with a distance of 20 cm. The foil stayed on a hot plate kept at 45-50 ^{o}C in order to evaporate solvents and enhance polymerization of fibers during the ESD process. The humidity was controlled to below RH 40%. The precursor solution in the syringe further filled up the silicon tube and needle by pushing a plunger of the syringe.

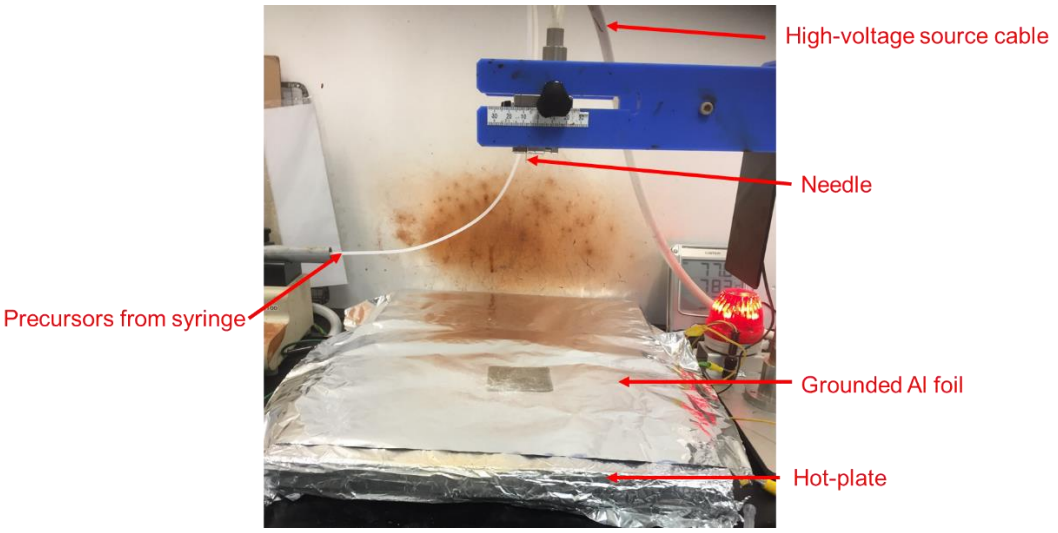

Fig. 2.5 A actual photo of ESD instrument used in this study.

After completing setting up of ESD process, MCF precursor solutions were spun by applying a potential difference of + 20 kV to +25 kV under the flow of the precursor solution at 2 ml/h, which was controlled by a syringe pump (KDS 100 made by KD Scientific, at the left side of Fig. 2.5).

2.1.4.2 Heat treatment

Fibers as-spun by ESD were further stabilized by a post heat treatment since fibers were pearl white or bright yellow as seen Fig. 2.6 (a) stayed under in low polymerization degree. Without a post heat treatment of stabilization, the fiber structure easily crushed during the carbonization process. In order to complete the polymerization process, step-by-step heating at 50 ºC for 3 h, at 110 ºC for 5 h, and then 170 ºC for 5 h in the air was performed. Stabilized fibers were turned into brown as shown in Fig. 2.6 (b).

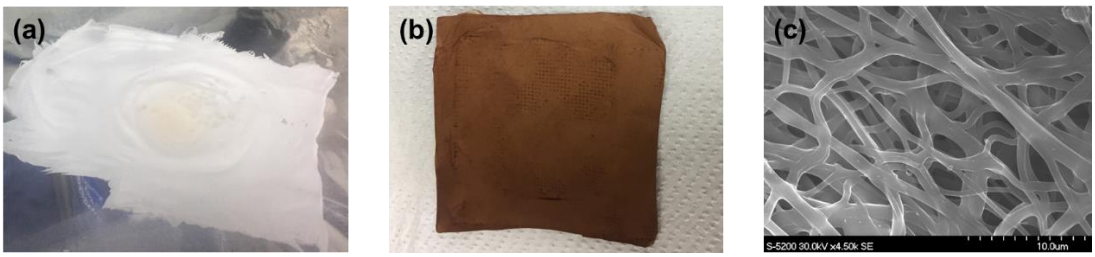

Fig. 2.6 Photos of as-spun fibers (a) and stabilized fibers (b), and an SEM image of carbonized fibers (c).

Stabilized fibers were calcined through the similar heat treatment process to MC bulk as explained in section 2.1.2. Typically, they were heated up to 400 ºC with the rate of 1 ºC/min, kept at 400 ºC for 3h, further heated up to 800 ºC with the rate of 1 ºC/min, and kept for 6 h under N_2 atmosphere. An SEM image of carbonized fibers are shown in Fig 2.6 (c).

2.1.5 Deposition of Pt onto MCFs

Before the deposition of Pt nanoparticles, bulk MC and MCFs were ball-milled (450 rpm for 2 h, and 800 rpm for 2 h) into μm-scale size particles. Pt nanoparticles were deposited using a method of reduction of $Pt(acac)_2$ precursors. A deposition procedure was described as Fig. 2.7. First, 105 mg of carbon powder was mixed with $Pt(acac)_2$ solution, which was made from dissolving 108.54 mg of $Pt(acac)_2$ into the appropriated amount of dichloromethane, under ultrasonic vibration. After fully mixed, the solution was continuously sonicated at 50 ºC for 1 h and further sonicated until completing evaporation of the solvent.

The residential black powder with yellow spots was heated with a heating rate of 1 ºC/min, and heat treated at 210 ºC for 3h and 240 ºC for 3 h under N_2 atmosphere. Pt deposited bulk MC and MCFs were named as Pt/MC and Pt/MCFs, respectively.

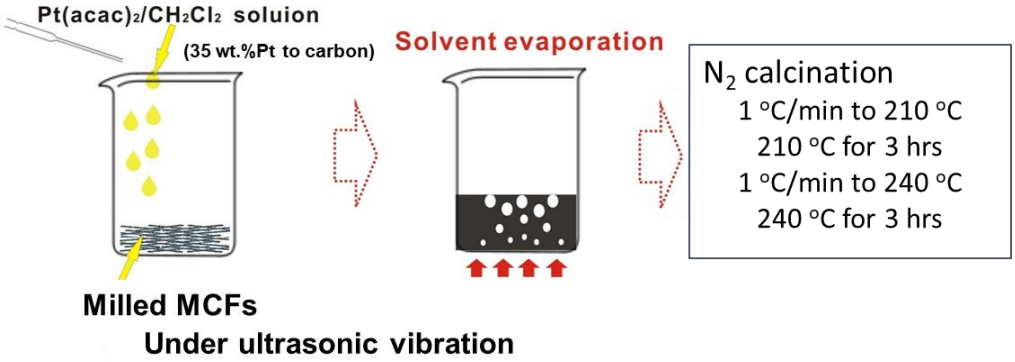

Fig. 2.7 A schematic of Pt deposition process.

Pt deposition directly on MCF sheet was also tried. Pt deposition process schematically explained in Fig. 2.8. MCF sheet (0.8 mgC/cm^2) was placed into the Pt precursor/CH_2Cl_2 solution under the ultrasonic vibration. Then, the solvent was evaporated by heating up to 50 ºC under ultrasonic vibration. After full evaporation of the solvent, 1-2 ml of CH_2Cl_2 was re-added, and the solvent was evaporated again. This

process was repeated for 3 times to achieved the high wt.% Pt deposition. Heat treatment was the same for other MCFs

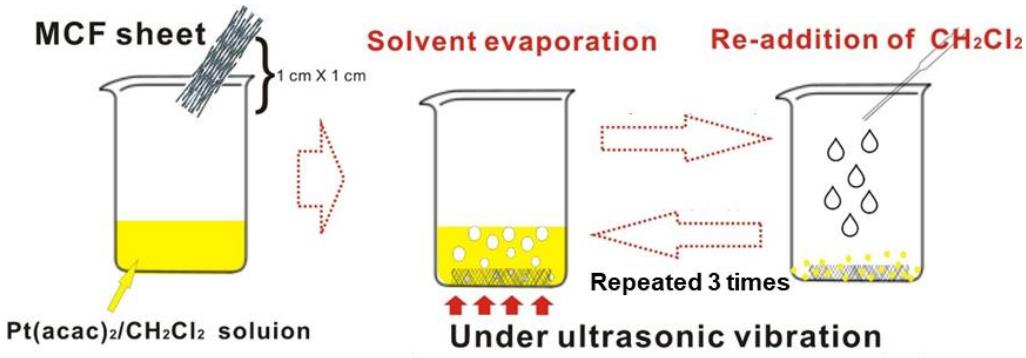

Fig. 2.8 A schematic diagram of the Pt deposition process on MCF sheet.

In addition to the typical heating procedure, modified heat treatment was also tried. In the modified calcination process, the heat treatment at 240 °C was removed in order to see passible reduction in Pt particle size.

2.2 Characterizations methods

2.2.1 N_2 adsorption/desorption measurements

The porosity is often one of major criteria for materials used in electrochemical device [3]. Therefore, evaluation of porosity of MCFs, including the pore volume and pore diameter, was performed using N_2 adsorption/desorption measurements.

The N_2 adsorption/desorption measurement is a technique used to evaluate the amount of adsorbed N_2 gas. Based on the theory of evaporation, at the liquid-gas two-phase interface, the evaporation/condensation process reaches the steady state when the gas pressure reaches saturation of vapor pressure, which means the amount of gas molecules adsorbed on the surface of samples (n) can be obtained from the value of the steady state vapor pressure (p). The same idea is used for N_2 adsorption/desorption measurements. According to BET theory [4], with changing in relative pressure (p/p0), the gas adsorption behavior is shown as Fig. 2.9.

When the adoption behavior of gas molecules on the solid surface in the low pressure region ($p/p_0 < 0.35$) follows a monolayer adsorption theory model provided by Brunauer, Emmett, and Teller [4], following 3 hypotheses become true: (i) the surface is energetically homogenous; (ii) there is no lateral interaction between adsorbed molecules; (iii) the adsorption energies in the second and all higher layers are equal to

condensation energy of adsorption. The BET equation can be derived as follow (2.1).

$$\frac{p}{n(p_0-p)}S_a = \frac{1}{n_m c} + \frac{c-1}{n_m c \times \frac{p}{p_0}} \quad (2.1)$$

, where n_m is the amount of adsorbed molecules in the monolayer state,

c is the condensation factor of the adsorbed molecules,

n is the amount of absorbed gas in the steady state gas pressure of p.

In equation (2.1), $p/\{v(p_0-p)\}$ and $\{(c-1)/(v_m c\ p/p_0)\}$ varies by changing the value of p/p_0. If making plot with values of $p/\{v(p_0-p)\}$ and p/p_0, a linear relationship can be found, which is called as a BET plot [4]. The linear interaction with y axis can brings out the value of $n_m c$, and then, the value of n_m can be obtained. The specific surface area (S_a) can be obtained by equation (2.2),

$$S_a = \frac{n_m \times N}{V_m} \quad (2.2)$$

, where N is Avogadro constant,

V_m is the molar volume of the adsorbed gas.

Also, the mesoporosity can be evaluated in the stage 4, where condensation of adsorbed molecules occurs in the Fig. 2.9. The amount of adsorbed molecules is used to derive the size of pores by using BJH (Barret Joyner Halenda) model [5]. In this model, it is assumed that all pores on the solid surface are cylindrical, and the pore with different radius (r_k) is filled up under different relative pressure. The relation between r_k and relative pressure p/p_0 can be derived from Kelvin equation (2.3).

$$\ln\left(\frac{p}{p_0}\right) = -\frac{2\gamma V_m}{RT\ r_k} \quad (2.3)$$

, where γ is the surface tension of adsorbed molecules in the condensed phase (liquid),

V_m is the mole volume of adsorbed molecules in liquid phase,

r_k is the size of pores.

Such mesoporosity obtained from BJH analysis can be divided into different groups with their pore size, such as microporous (pore size < 2 nm), mesoporous (2–50 nm), and macroporous (>50 nm) structure.

In this study, all samples were pre-treated at 200 °C under vacuum for 3 h in order to remove water and organic residuals. BELSORP-mini II-VS (BEL Japan®) was used for N_2 adsorption/ desorption measurements. A sample was cooled in liquid N_2 (-196

°C) and N_2 gas was filled into the sample tube. The total surface area was calculated by using BET model using the data in the low pressure region, and pore diameter and pores size distribution were calculated from BJH model.

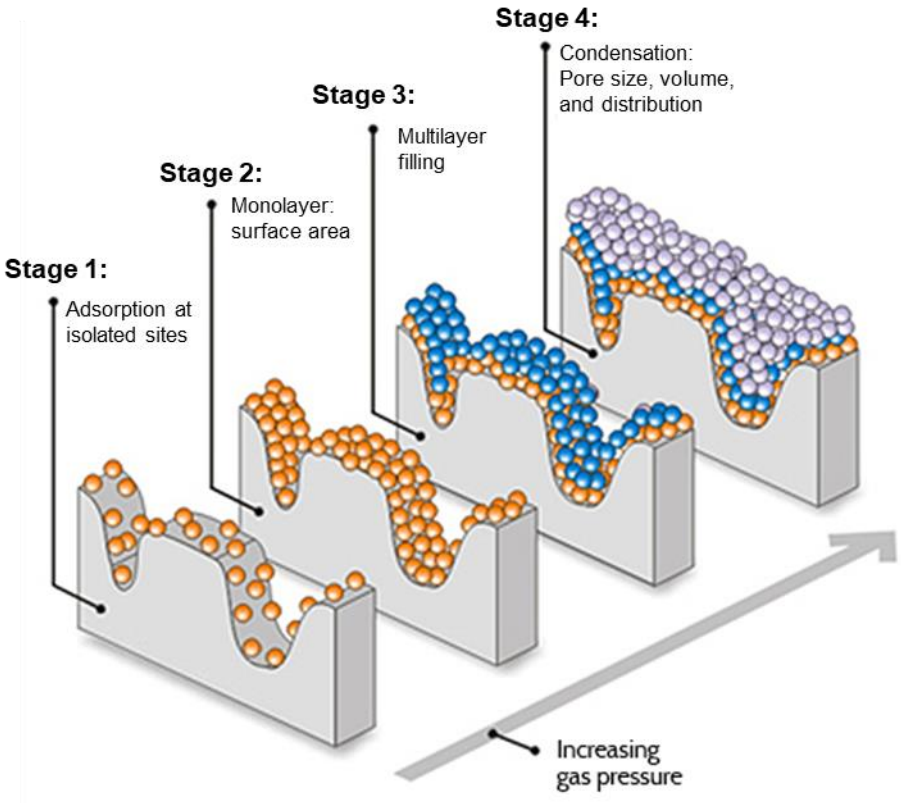

Fig. 2.9 A schematic diagram of the multilayer adoption model.
(Reproduced from ref. [5] with permission)

2.2.2 Scanning electron microscope (SEM)/scanning transmission electron microscope (STEM) observation

Direct observation of surface morphology and inner pore structure of materials is important in addition to indirect methods such as N_2 adsorption measurements. In this research, SEM was used to check the macrostructure and surface morphology of samples. STEM was used to check the porous structure and distribution of Pt particles.

The SEM can produce images by scanning the surface of a sample by using a focused electron beam. As shown in Fig. 2.10 (a), when a sample is hit by a high energy electron beam, the secondary electron, the back field emission electron, and the X-ray emitted from the sample surface are collected by the detector for various of analyses. Especially elemental analysis can be performed by energy dispersive X-ray

spectroscopy (EDS). In normal SEM images, bright sites of the image represent the solid part, and dark sites represent open space like pores that don't reflect the electron.

The working principle of STEM is explained in Fig. 2.10 (b). A high energy electron beam is accelerated under vacuum and transmits the specimen. In the image obtained from transmitted electrons, bright sites represent open space like pores, which is opposed to SEM images. Since de Broglie wavelength of electrons is small, STEM has an ability to image at very high resolution, and the detection of an individual atom is also possible.

In this study, FE-SEM SU-9000 from Hitachi Co., Ltd. equipped with an EDX detector and a transmission mode was used. For the typical sample preparation, a sample was milled into small particles and mixed with ethanol to make the diluted suspension. The suspension was drop coated onto a carbon-coated copper mesh, and the mesh was dried in the oven at 100 ºC for 3 h to remove the solvent. For SEM observation, the accelerated voltage of electron beam was set between 15 kV to 30 kV. For STEM observation, the accelerated voltage of electron beam was set to 30 kV.

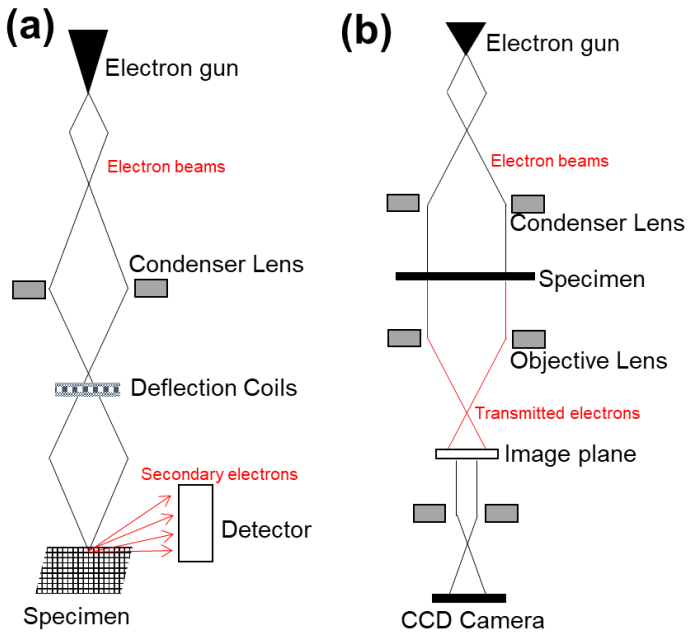

Fig. 2.10 Schematic diagrams showing the working principle of SEM (a) and STEM (b).

2.2.3 X-ray diffraction (XRD) analysis

XRD is a non-destructive X-ray analytical technique and is often used for

characterization of the crystalline structure of materials, including inter-atomic spacing, inter-planar spacing, and the crystalline size [6]. This technique is based on constructive interference of monochromatic X-ray diffracted from crystalline samples. The principle of XRD is shown in Fig. 2.11. The difference in the optical path length between the X-ray diffracted by the first atomic plane and the second atomic plane causes constructive interference, and further leads to the difference in the intensity of diffracted X-ray. The relation between the wavelength and diffraction angle fits in the Bragg's law, which is expressed in equation (2.4). According equation (2.4), the position of atoms in the crystal lattice can be determined by measuring the angle and intensity of diffracted beams.

$$n\lambda = 2d \sin\theta \tag{2.4}$$

, where n is a positive integer,

λ is the wavelength of X-ray,

d is the spacing between crystalline interlayers,

θ is the diffraction angle between incident X-ray and scattering planes.

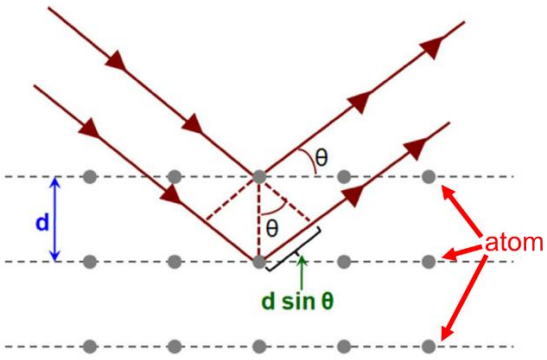

Fig. 2.11 A schematic diagram showing principle of XRD.

In this study, RINT Ultima III /PSA from Rigaku with X-ray source of CuKα (λ=1.54 Å) was used for XRD measurements. Samples were prepared as powder and placed onto a glass holder, and XRD patterns were recorded at a scan rate of 2θ =0.2 °/min with diffractometer operating at 3 kW (30 mA; 40 kV).

2.2.4 Thermogravimetric analysis (TGA)

TGA is a useful method to know decomposition temperature of materials and understand the nature of materials. Thermal analysis based on changing in mass of

samples on the time and temperature change is possible. In this study, ThermoPlus TG8120 from Rigaku was used for TGA. Air and N_2 were used as ambient gases for analyzing polymer decomposition and deposited Pt percentage on carbon supports, respectively.

2.2.5 CHN elementary analysis

For analyzing the degree of carbonization, carbon, hydrogen, and nitrogen, CHN, elementary analysis is one of the useful methods to find out the atomic ratio of C, H and N within samples. [7]

This analytical method is based on a differential thermal conductivity method. The sample is completely burned under the He and O_2 ambient atmosphere within a combustion furnace with CuO filled. The sample is converted to H_2O, CO_2, NO_x gases, and other residential compounds. NO_x gas is reduced to N_2 by Cu at a reduction furnace. The other gases except for H_2O, CO_2, and N_2 are removed by absorbers in the combustion or reduction furnace. Amounts of H_2O, CO_2, and N_2 gases are detected by individual thermal conductivity detector and converted into the content ratio of C, H and N atom.

In this study, Yanaco CHN Corder MT-5, MT-6 manufactured by Yanaco Apparatus Development Laboratory Co., Ltd. was used for CHN elemental analysis. The weight of sample was pre-measured by an ultra-micro balance, the Mettler Toledo XP2U. The measurement service was provided by the service center of the elementary analysis of organic compounds, Faculty of Science, Kyushu University.

Fig. 2.12 A photo of CHN analyzer.

2.2.6 Focused ion beam (FIB)-SEM obsercation

FIB-SEM is a SEM equipped with high energy Ga-ion beam, it is commonly used for fabrication of a sample in order to make an ultra-thin specimen, for example, for TEM observation. In this study, FIB-SEM Helios NanoLab 600i manufactured by Thermo Fisher Scientific K. K. was used for cross-sectional observation of catalyst layers. The ion beam current for rough fabrication and fine fabrication were chosen to 9.4 nA, and 0.4 nA, respectively. After the fine fabrication, cross-sectional morphology and thickness of catalyst layers were evaluated by SEM with high resolution.

2.3 Fundamental electrochemical characterization

2.3.1 Principle of a solution half-cell measurement

A half-cell measurement in the liquid electrolyte is important for fundamental electrochemical characterization of electrocatalysts. In addition, only a few mg of materials are required, which is an advantage on initial characterizing materials. The setup requires three electrodes, working, counter and reference electrodes, and a liquid electrolyte, as shown in Fig. 2.13.

To proceed electrochemical reactions, two electrodes, working electrode and counter electrode are the standard requirement. However, since reactions at both electrodes take place simultaneously, a reference electrode is required to control the potential at the working electrode. Therefore, the three electrode system has been developed [8].

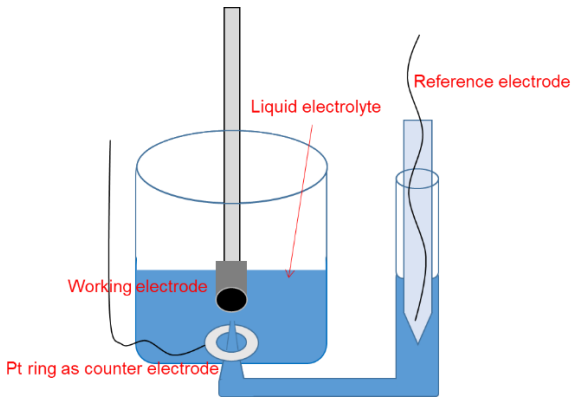

Fig. 2.13 A diagram showing of 3-electrode half-cell setup.

The reference electrode usually has a stable solid-solution chemical interface. In

this study, a common silver/ silver chloride electrode (Ag/AgCl) was used as a reference electrode. The structure of Ag/AgCl electrode used in this study is described in Fig. 2.14, which is designed as a double junction type. A silver wire with AgCl is placed in saturated potassium chloride (KCl) solution within the inner junction tube, which is connected to the outer junction tube through a ceramic tip. The solution with a ceramic tip in the outer junction tube works as a salt bridge and prevents direct contamination from chloride ions on the working electrode. The outer junction tube usually is filled with saturated KCl when it isn't in use and filled with the same solution as the electrolyte, such as 0.1 M $HClO_4$, when it is in use, to minimize internal resistance. The obtained voltage was re-calculated to the standard potential against a reversible hydrogen electrode (vs. RHE) in this study.

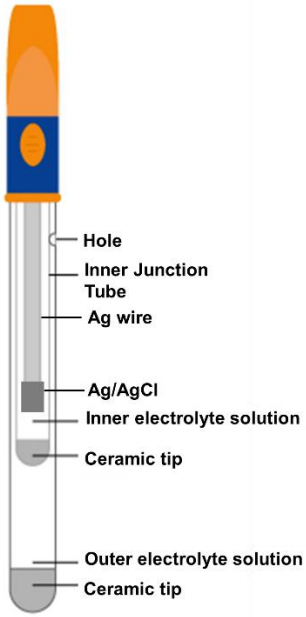

Fig. 2.14 A scheme diagram of double junction Ag/AgCl electrode.

The working electrode, can be separated into two parts, catalysts themselves and a substrate for catalyst loading. A method of preparation of a working electrode with catalysts is explained in detail in the next section 2.3.2. A substrate electrode should not be involved in reactions by itself except for transferring electrons. In this research, a glassy carbon (GC disk, Tokai Fine Carbon Co., Ltd.) with the diameter of 5 mm was used as a substrate electrode. Although GC is composed of carbon similar to our MC and MCFs, the surface area of GC small like less than 10 cm^2/g, resulted in almost no effect on electrochemical measurements of our materials.

The counter electrode allows current flow without generating high resistant. Therefore, materials with high electronic conductivity and high durability are required. In this study, the platinum plate with the outer diameter of 1.5 cm and the inner diameter of 1 cm was used as a counter electrode.

2.3.2 Preparation of a working electrode

In this study, Pt/MCFs, Pt/MC and commercial available TKK TEC10E50E (Pt/KB) catalysts were used. Working electrodes are basically prepared by drop casting of the slurry containing catalysts. Pt loading was set to 17.3 μg/cm^2, which was followed by the protocol from NEDO [9].

For the typical slurry preparation of Pt/MC and Pt/MCFs, 7.50 mg of the powder sample was dissolved into 5.32 ml of IPA and 0.50 ml of H_2O. The solution was fully mixed by using ultra-sonication with ice-bath to prevent increase in the temperature. For Pt/KB catalyst, the amount of the catalyst powder was reduced to 4.3 mg, but the solvent was kept to the same, such as 5.32 ml of IPA and 0.5 ml of H_2O. After the slurry preparation, 10 μl of the slurry were drop-casted onto a GC disk by using micro-pipette, and the coated GC disk was dried in the air overnight.

Besides electrocatalysts, various carbon materials were electrochemically evaluated. For preparation of working electrodes in this case, the typical slurry containing MC, MCFs, CNF or XC-72 was prepared in the following. The 6 mg of carbon powder was mixed with 3 ml of IPA. Then the slurry was fully mixed by using ultra-sonication with ice-bath to prevent increase in the temperature. After the slurry preparation, 10 μl of the slurry (containing 20 μg of carbon) were drop-casted onto a GC disk by using micro-pipette, and the coated GC disk was dried in the air overnight.

2.3.3 Cycling voltammetry (CV) and linear sweep voltammetry (LSV)

CV [8] is an electrochemical technique measuring the current generated by electrochemical reactions under the voltage cycling. In a typical CV, after the set potential is reached, the potential on the working electrode is ramped in the opposite direction to return to the initial potential, as described in Fig. 2.15. The current passed through the working electrode is plotted versus the applied voltage to give the cyclic voltammogram. LSV is a similar technique, but the potential sweep is only one direction.

In this study, potentiostat / galvanostat HZ-7000 manufactured by HOKUTO

DENKO was used to record the signals measured from three-electrode half-cell setup. The 0.1 M of $HClO_4$ was used as an electrolyte for all electrochemical evaluations in this study. All measurements were done at room temperature.

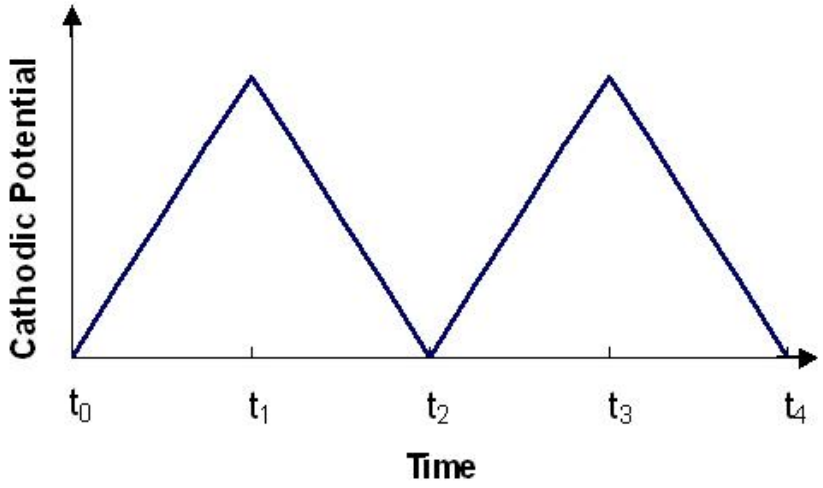

Fig. 2.15 CV potential waveform.

2.3.4 Electrochemical active surface area (ECSA)

A typical cyclic voltammogram for Pt/C catalyst in the acid electrolyte is shown in Fig. 2.16 [8]. The calculation of ECSA of Pt is based on adsorption and desorption of H atom on the Pt metal surface, which can be seen between 0 and 0.4 V (vs RHE). Within that voltage range, the peak with the positive current represents the desorption of H atoms, where the integration of the curve represents the desorption charge (Q_{des}). From the Q_{des}, ECSA can be calculated based on the electronic charge when one hydrogen atom is adsorbed per Pt atom, which is 210 C/m^2 [10]. The calculation of ECSA can be list as equation (2.5).

$$\mathrm{ECSA} = \frac{\text{Desorption charge from peak integration } Q_{des}(C)}{210\ \left(\frac{C}{m^2}\right) \times total\ Pt\ loading\ (g)} \qquad (2.5)$$

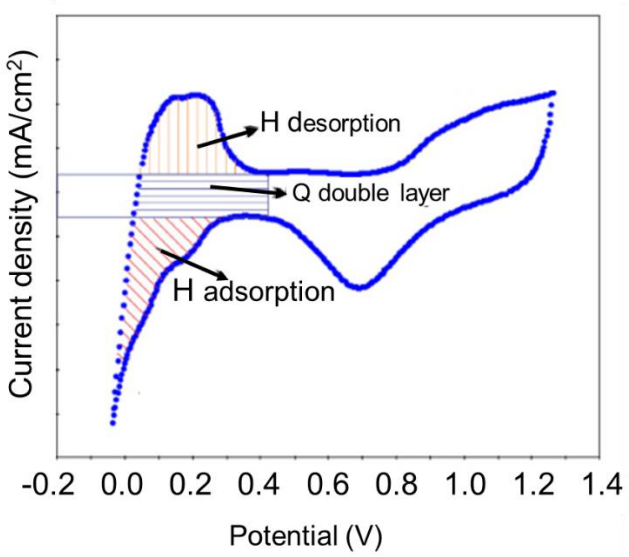

Fig. 2.16 A typical cyclic voltammogram for Pt/C in the acid electrolyte.

In this study, to evaluate ECSA of Pt in electrocatalysts, the voltage was cycled between 0.05 and 1.2 V (vs. RHE). After the electrochemical cleaning of Pt surface by cycling 50 times at 50 mV/s in the N_2 saturated electrolyte, additional 5 stable cycles were obtained at 20 mV/s to calculate ECSA.

2.3.5 ORR measurements with rotating disk electrode (RDE)

Measurements using RDE is a conventional method to study the mechanism of electrochemical reactions and to determine their kinetic parameters. The working principle of RDE is shown as Fig. 2.17. By controlling the mass transport speed of species arriving and leaving from the working electrode surface through the change in rotation speed of the working electrode, a quantitative analysis of ORR activity of catalysts is possible.

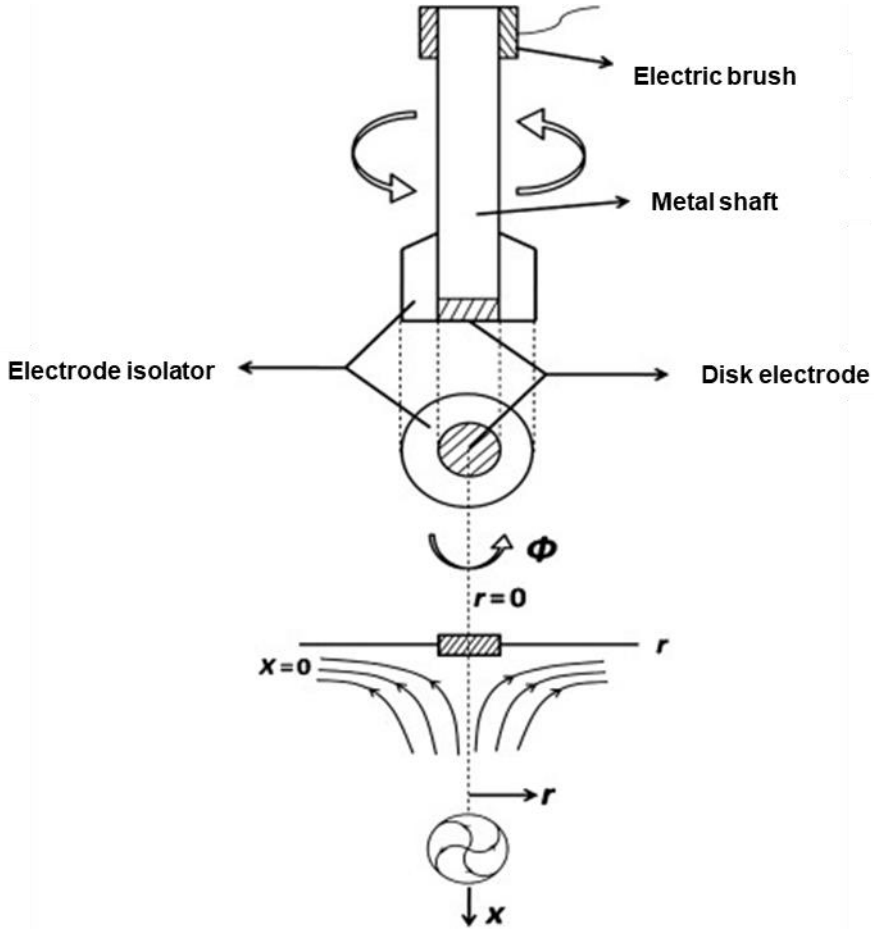

Fig. 2.17 A schematic diagram of RDE working principle.

In this study, LSV measurements were performed with different rotational speeds of RDE at a scan rate of 20 mV/s in the O_2 saturated electrolyte.

According to the Koutecky-Levich theory [11], the current measured with RDE system can be divided into dynamic terms and kinetic terms, as shown in equation (2.6).

$$\frac{1}{i_m} = \frac{1}{i_k} + \frac{1}{i_d} \quad (2.6)$$

, where i_m is the current density measured by LSV,

i_k is the kinetic current density based on the catalytic reaction,

i_d is the dynamic current density, which is also called as the limiting current based on the diffusion of reactants and products.

The i_d term can be further expressed as equation (2.7)

$$0.62\ nFD_o^{2/3}\nu^{-1/6}\omega^{1/2}C_o^0 \quad (2.7)$$

, where n is the number of exchanged electrons,

F is Faraday constant,

D_o is the diffusion constant of oxidant in the electrolyte,

ν is the viscosity of electrolyte,

C_o is the concentration of oxidant.

The i_k does not depends on the rotating speed ω and is the current under the infinite rotational speed, where mass transfer effect is eliminated. In practical, LSV curves with different rotating speed should be obtained as shown in Fig. 2.18 (a). Then, by using the current in the region of $i_k > i_d$, usually between 0.8-0.9 V (vs. RHE), the Koutecky-Levich plot as shown in Fig. 2.18 (b) can be obtained. The intersect of linear fitted lines to the Y-axis is $1/i_k$. Once i_k is found, ORR mass activity can be further calculated by dividing by the mass of Pt.

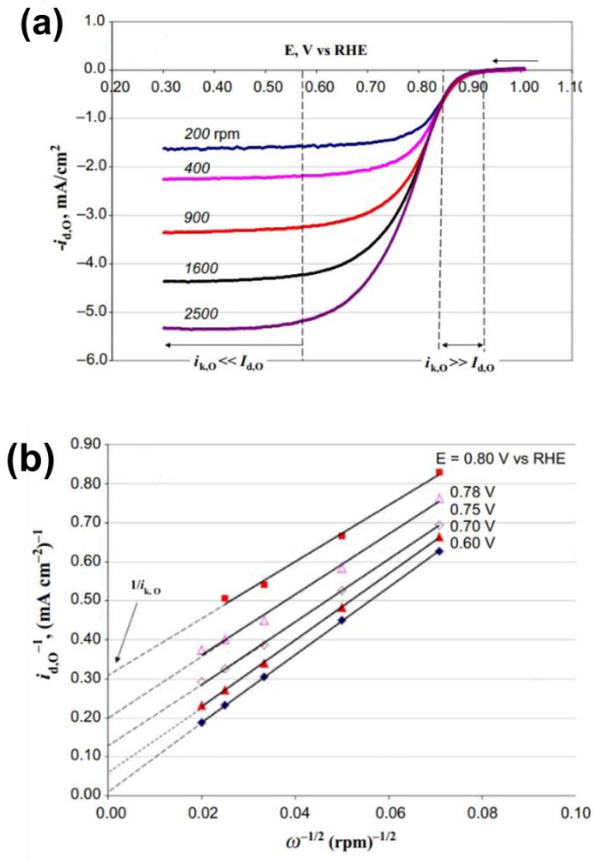

Fig. 2.18 Typical LSVs with different rotation speeds (a) and corresponding Koutecky-Levich plots (b) of Pt/C.

2.3.6 Electrochemical double layer

CV is also a useful technique to estimate the active surface area of carbon materials themselves. In the research field of supercapacitance [12], the active surface area of carbon is highly related to the thickness of the electrochemical double layer. Electrochemical double layer capacitance (EDLC) quantitatively represents the charge stored in carbon materials. Fig. 2.19 shows typical CV curves of three carbon materials with different surface area. The capacitance is quantitatively described as specific capacitance C (F/g), and C can be calculated by equation (2.8)

$$\mathrm{C}\ \ (\mathrm{F/g}) = \frac{Q_{st}(C)}{\Delta V\ \ (V) \times total\ \ C\ \ loading\ \ (g)} \tag{2.8}$$

, where Q_{st} is the average charge during the charging and discharging process,

ΔV is the voltage window of the double layer region.

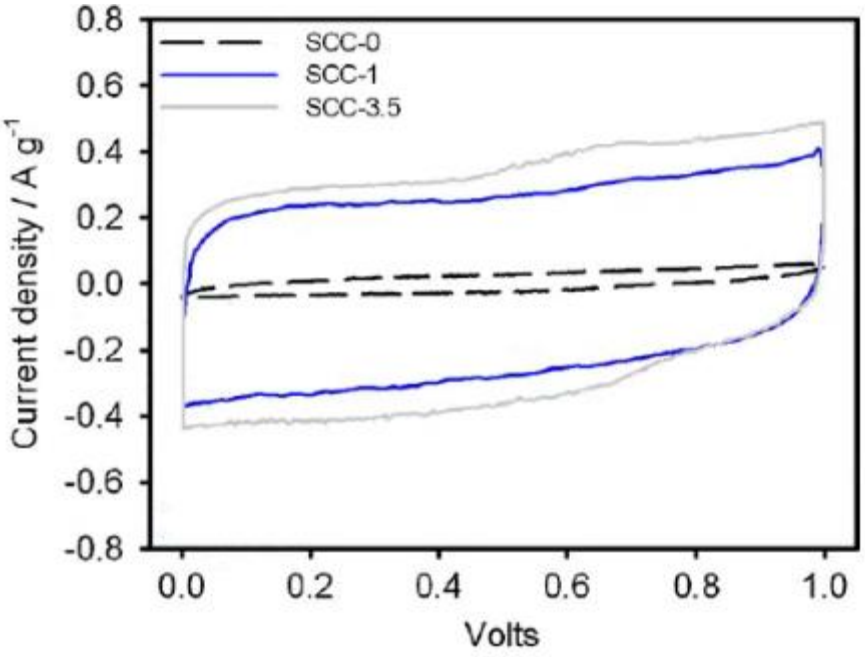

Fig. 2.19 Typical CV curves showing electrochemical double layers of carbon materials with different surface area.

2.3.7 Charge and discharge (CDC) curves

CDC is a technique that is often used to evaluate the performance of capacitance of carbon materials. Unlike CV and LSV, which control the voltage to draw the voltammogram, CDC controls the current. With the set current, the voltage on the working electrode is kept increasing until the set potential is reached. Then, the potential on the working electrode is scanned to the opposite direction with a set current with the negative value in order to return to the bottom limit of the potential. Typical CDC curves are shown as Fig.2.20.

In this study, CDC curves were obtained after CV measurements test in N_2 saturated electrolyte. The values of charge and discharge current were set to 100 μA, 50 μA, 25 μA, 20 μA, and 10 μA. The discharge specific capacitance (C_{des}) can be calculated from the discharge curves by the following equation (2.9):

$$C_{des} = \frac{I\Delta t}{m\Delta V} \tag{2.9}$$

, where I (A) is the discharge current,

Δt (s) is the discharge time consumed in the potential range of ΔV,

m (g) is mass of the active materials (or mass of the total electrode materials),

ΔV (V) is the potential range.

The energy density (E) and power density (P) that can be stored in the capacitance were calculated by the following equations (2.10) (2.11):

$$E = \frac{C(\Delta V)^2}{2} \quad (2.10)$$

$$P = \frac{E}{\Delta t} \quad (2.11)$$

, where C is the specific capacitance of the active materials,

ΔV is the potential range of discharge.

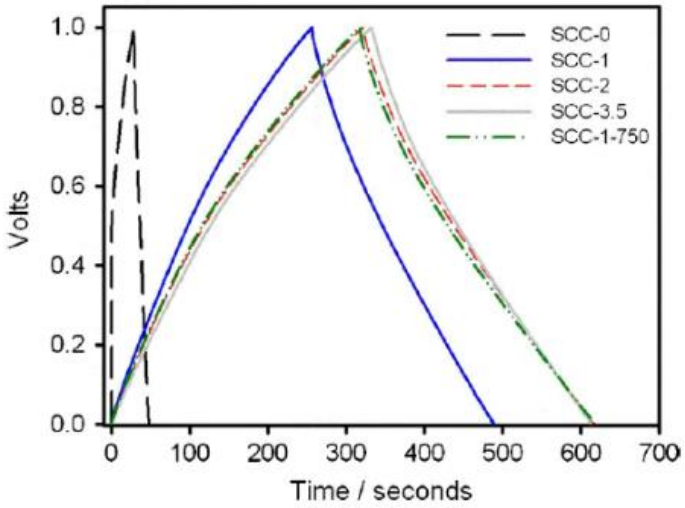

Fig. 2.20 Typical CDC curves for different carbon materials.

2.4 Preparation and evaluation of MEAs

2.4.1 Slurry preparation

The slurry containing the electrocatalyst and ionomer was prepared in the following steps. A powder electrocatalyst was weighted out and first mixed with a small amount of water in order to prevent for the electrocatalyst reacting with a next solvent, ethanol, violently. Then, ethanol and 5 wt.% Nafion® solution were further added. The solid content in the solution was controlled to under 3 wt.%, and the Nafion® ratio in the solid content was controlled to 28 wt.%. The solid content ratio can be calculated by a following equation (2.12).

$$\text{Solid content (\%) in the solution} = \frac{m + V_{nafion} \times d_{nafion} \times 0.05}{m + V_{nafion} \times d_{nafion} + V_{ethanol} \times d_{ethanol} + V_{water} \times d_{water}} \quad (2.12)$$

, where m is mass of the electrocatalyst powder (g),

V is volume of the liquid (ml),

d is density of the liquid (g/ml), d_{Nafion} : 0.93 g/ml, $d_{ethanol}$: 0.79 g/ml.

In this study, 0.105 g of electrocatalyst powder was mixed with 487 μl of water, 4500 μl of ethanol and 878 μl of 5 wt.% Nafion® solution. The solution was fully mixed by using ultra-sonication for 30 min with ice-bath to prevent the temperature raising.

For the slurry preparation of mesoporous carbon samples, an extra process was added to successfully encapsulate the Nafion ionomer into mesopores. First, 878 μl of 5 wt.% Nafion® solution was mixed with 2-3 ml of hexafluoro-2-propanol and ultra-sonicated until the solution turned into clear. Then, the Nafion solution was dropped into 0.105 g of Pt/MCF catalyst powder under ultrasonic vibration. The slurry was further ultra-sonicated and heated at 50 ºC for 2 h and further dried at 105 ºC in the oven for solvent evaporation. The resulting black powder was mixed with 487 μl of ethanol and 4500 μl of water as the ink slurry for spray printing.

2.4.2 Preparation of MEAs

MEAs were prepared by spray printing of the slurry explained in section 2.4.1 onto the both sides of Nafion 212 membrane. The specification of MEAs is listed in Table 2.1. The weight of the spray printed electrode was determined by measuring the weight of two pieces of carbon paper, which were also spray printed near the electrode.

The obtained MEAs were further hot-press at 132 ºC, near the glass-transition temperature of Nafion, with a pressure of 0.3 kN for 190 s.

Table 2.1 Specification of MEAs

Electrolyte	Nafion® 212
Anode catalyst layer	TKK TEC10E50E (0.3 mg/cm^2 Pt)
Cathode catalyst layer	TKK TEC10E50E, Pt/MCF, (0.3 mg/cm^2 Pt)
Reactive area	1 cm^2 square
Diffusion layer in anode/cathode	Carbon paper TGP-I-060

For the last part of this study, the composite cathode of TKK Pt/KB and MCF sheet and Pt/MCF sheet cathode were developed. The preparation procedure of the composite

cathode, Pt/KB-MCF sheet is explained as Fig. 2.21. First, Pt/KB catalyst layer was spray-printed on the Nafion membrane using Pt/KB slurry explained in the previous section to get the total Pt loading of 0.15 mg/cm^2. Then, a MCF-sheet (0.8 mgC/cm^2) was covered onto the spray printed Pt/KB layer. Then, the second layer of Pt/KB was spray-printed to get the total Pt loading of 0.15 mg/cm^2. Therefore, the total Pt loading of this composite cathode became 0.3 mg/cm^2.

For preparation of Pt/MCF sheet cathode, most of the processes were the same for Pt/KB-MCF sheet cathode. After spray printing 0.1 mgNafion/cm^2 using 2 wt.% Nafion/ethanol solution, Pt/MCF sheet (2.2 mgC/cm^2, 0.3 mgPt/cm^2) was placed on that. Then, Nafion layer (0.1 mgNafion/cm^2) was spray-printed on Pt/MCF sheet.

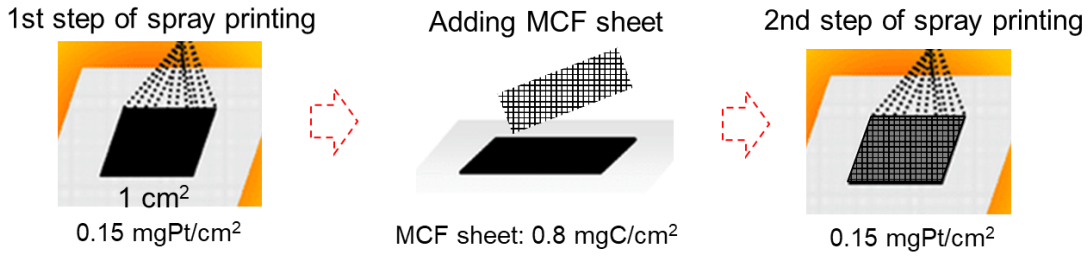

Fig. 2.21 Schematic drawing of the preparation procedure of Pt/KB-MCF sheet cathode.

2.4.3 Evaluation of MEAs

For electrochemical evaluation, MEAs were placed in a holder-designed by NEDO with two pieces of carbon paper (TGP I-060), as gas diffusion layers, two gaskets, two flow channel plates and two current collector sheets. Six screws were used for tightening with a torque force of 2 N-m. A schematic drawing of the assembly is shown in Fig. 2.22.

The resulting assembly was placed in the oven controlled to 80 ºC to evaluate electrochemical characterization. Gas lines were connected to the holder and their temperature was controlled to 120 ºC. The flow rates of H_2 and air were set at 139 sccm and 332 sccm, respectively.

The OCV was measured for 5 mins after supplying H_2 and air for 30 mins, and then, the voltage was set at 0.6 V for 4 h the for the pre-conditioning. After the preconditioning, impedance was measured under the conditions of 50 mA/cm^2, 100 mA/cm^2 and 200 mA/cm^2, with the change in frequency from 0.1 Hz to 100 kHz. The I-V curve was measured from 0 mA to 800 mA with the increasing rate of 0.5 mA/s.

For the Tafel evaluation, I-V curve was separately recorded from 0 mA to 100 mA with the increasing rate of 0.1 mA/s.

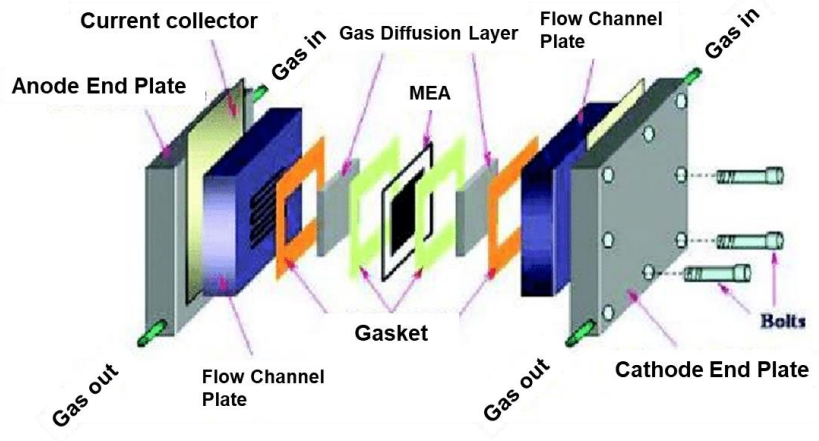

Fig. 2.22 A schematic diagram of the assembly of a MEA and a holder designed by NEDO project.

2.4.4 Separation of ohmic, activation, and concentration overvoltage

The electrochemical impedance spectroscopy (EIS) is an important technique to separately analyze the individual overvoltage. For EIS, the voltage sin wave ($V(t)= V_0Cos(\omega t)$) is applied, then, $I(t)=I_0Cos\ (\omega t-\theta)$ is obtained by varying frequency, ω. The corresponding impedance is expressed as $Z=Z_0(Cos\ \theta+jSin\ \theta)=Z_r+Z_i=Z'+Z''$. A plot made with Z' as X-axis and Z'' as Y-axis is called Nyquist plot. A typical Nyquist plot and its electrical circuits diagram are shown in Fig. 2.23.

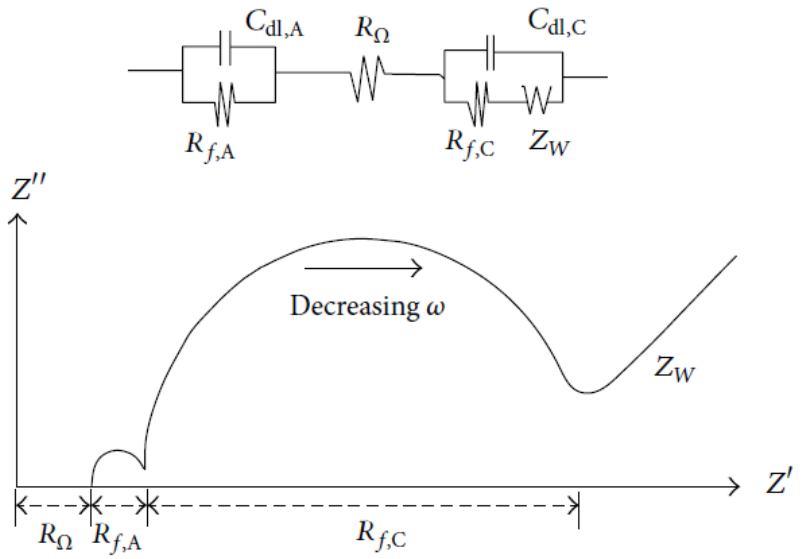

Fig. 2.23 A typical Nyquist plot and the corresponding electric circuit for PEFC.

The separation of each overpotential from the I-V curve is explained in the following,

1. Ohmic resistance (R_{Ohm}) is obtained from the first intersect point of the X-axis of Nyquist plot measured at a certain current density, for example, 200 mA/cm^2.
2. IR-free voltage is obtained by $V_{ir\text{-}free} = V_{meas.} + i_{meas.} \times R_{Ohm}$.
3. The liner regression analysis of the Tafel plot ($V_{ir\text{-}free}$ vs. log(i)) is performed. From the obtained linear line, V_{tafel} is calculated.
4. Activation overvoltage is obtained by $V_{act.}$ = 1.17 (theoretical OCV) - V_{tafel}.
5. Ohmic resistance is obtained by $V_{ohm.} = i_{meas.} \times R_{Ohm}$.
6. Concentration overvoltage is obtained by $V_{con.} = V_{tafel} - V_{ir\text{-}free}$.

2.4.5 Evaluation of through plane electronic resistance

In order to measure the through plane electronic resistance of carbon materials, the setup as is described in Fig. 2.24 was used in this study. Two pieces of 25 BC carbon paper (1 cm × 1 cm) with spray-printed carbon thin film (1.5 mgC/cm^2) were assembled with one piece of TPI H-090 carbon paper (1 cm × 1 cm), and then, the carbon assembly was placed into a same cell holder used for MEA evaluation. The impedance of the assembled cell was measured under the conditions of 0 V, with the amplitude 0.05 V and the change in frequency from 0.1 Hz to 100 kHz. The value of intersect point to the Re Z was recorded as the through plane electronic resistance for all samples.

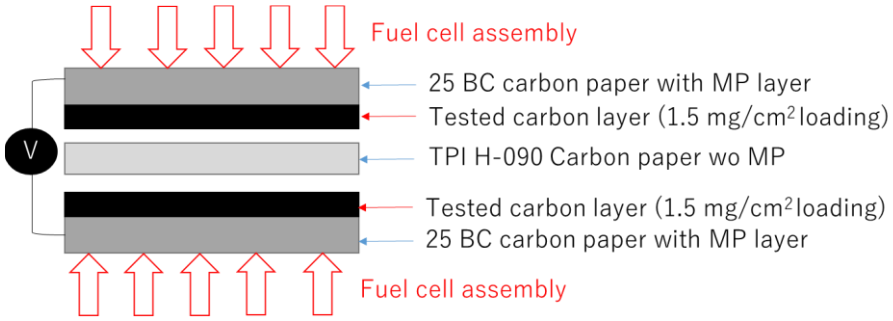

Fig. 2.24 A schematic diagram of a test cell for evaluation of through plane electronic resistance.

List of references

[1] R.B. Durairaj, Resorcinol Based Resins and Applications. In: Resorcinol Chemistry, Technology and Applications, Springer, Berlin, 2005, pp. 179-261.

[2] A. Greiner, J. H. Wendorff, Electrospinning: A Fascinating Method for the Preparation of Ultrathin Fibers, Angew. Chem. Int. Ed., **46**, 5670-5703 (2007).

[3] C. M. A. Parlett, K. Wilson, A. F. Lee, Hierarchical porous materials: catalytic applications, Chem. Soc. Rev., 42, 3876-3893 (2013).

[4] S. Brunauer, P. H. Emmett, E. Teller, Adsorption of gases in multimolecular layers, J. Am. Chem. Soc., **60** (2), 309–319 (1938).

[5] E. P. Barrett, L. G. Joyner, P. P. Halenda, The determination of pore volume and area distributions in porous substances. I. computations from nitrogen isotherms, J. Am. Chem. Soc., **73** (1), 373–380 (1951).

[6] W. H. Bragg, The reflection of X-rays by Crystals, Nature, **91**, 477 (1913).

[7] I. Matejovic, Determination of carbon, hydrogen, and nitrogen in soils by automated elemental analysis (dry combustion method), Commun. Soil Sci. Plant Anal., **24** (17&18), 2213-2222 (1993)

[8] J. F. Rusling, S. L. Suib, Characterizing materials with cyclic voltammetry, Adv. Mater., **6** (12), 922-930 (1994).

[9] 固体高分子形燃料電池実用化推進技術開発基盤技術開発「セル評価解析の共通基盤技術」セル評価解析プロトコル , NEDO (2014)..

[10] J. M. D. Rodríguez, J. A. H. Melián, J. P. Peña, Determination of the real surface area of pt electrodes by hydrogen adsorption using cyclic voltammetry, J. Chem. Educ., **77** (9), 1195-1197 (2000)

[11] J. Masa, C. Batchelor-McAuley, W. Schuhmann, R. G. Compton, Koutecky–

Levich analysis applied to nanoparticle modified rotating disk electrodes: Electrocatalysis or misinterpretation? Nano Research, **7** (1): 71–78 (2014).

[12] W. G. Pell, B.E. Conway, Analysis of power limitations at porous supercapacitor electrodes under cyclic voltammetry modulation and dc charge, J. Power Sources, **96** (1), 57-67 (2001).

CHAPTER 3

Synthesis and Characterization of MCFs

Chapter 3 : Synthesis and Characterization of MCFs

Introduction

In this chapter, synthesis and characterization of MCFs were fully introduced. This chapter was divided into three sections; 3.1 Syntheses of MCFs, 3.2 Optimization of the calcination process for MCFs, and 3.3 Characterization of MCFs.

3.1 Syntheses of MCFs

3.1.1 MCFs made with different linear additives for ESD

MCFs made with two different linear additives, PVA and PVB, were synthesized as the process mentioned in section 2.1.3.1 and section 2.1.4. N_2 sorption/ desorption isotherms and corresponding BJH plots of MCFs made with PVA and PVB, named as MCF-PVA and MCF-PVB, are shown in Fig. 3.1 (a) and Fig. 3.1 (b), respectively.

As shown in Fig. 3.1 (a), the adsorbed gas volume (V_a) of MCF-PVB significantly increased below the relative gas pressure of 0.1 p/p_0, indicating the presence of the large amount of micropores, where diameter < 2 nm. Such micropores contributed to increase BET surface area, such as 435 m^2/g. Regarding to MCF-PVA, although Va of MCF-PVA didn't increase much in the low relative gas pressure region, leading to relative low BET surface area of 223 m^2/g, a step of increase in V_a from 0.5 to 0.8 p/p_0 was found, indicating the existence of mesopores. The BJH pore distribution (Fig. 3.1 (b)) revealed the existence of mesopores with the range of 4 to 10 nm, only for MCF-PVA.

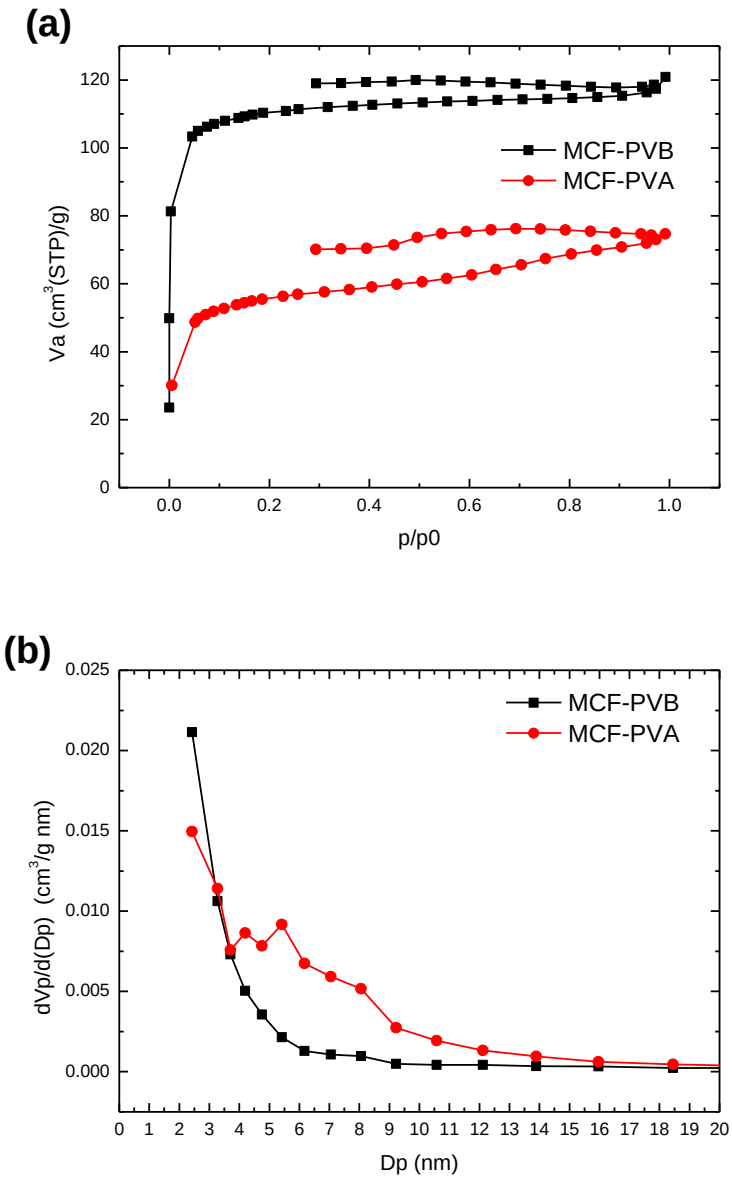

Fig. 3.1 (a) N_2 sorption isotherms and (b) BJH plots of MCF-PVA and MCF-PVB.

The reason for this difference in the mesoporosity is most likely related to the molecular interaction within the precursor solution and the electrostatic force induced by the high voltage during the ESD process. According to the literature [1], the molecules that bring negative charge tend to move toward the surface of fibers because of the positive voltage charge during the ESD process. This phenomenon is due to the electrostatic force. In this study, the partial polymerized resorcinol-formaldehyde resin, Pluronic F127, PVA and PVB are major molecules in the precursor solution. Since the resorcinol-formaldehyde resin is a three-dimensional polymer and its partial charge

within the polymer can be self-balanced, other three linear polymers, Pluronic F127, PVA and PVB in the precursor solution were focused. Although the movement of these linear polymers during ESD process could not be evaluated directly, the dipole moment caused by O-atoms in the molecules were considered, in this study.

Molecular formulas of Pluronic F127, PVA, and PVB with the dipole moment caused by O-atoms are shown in Fig. 3.2 (a), Fig.3.2 (b) and Fig. 3.2 (c), respectively. In case of PVB and Pluronic F127, each O-atom is bonded with two C-atoms, resulting in the similar molecular dipole moment. When the voltage from ESD is applied to these two molecules, electrostatic force generated from these two results in the same. The arrangement of Pluronic F127 results in rather linear chains than micelles as shown in Fig 3.3. Consequently, the mesopores formed from the decomposition of F127 can be very small.

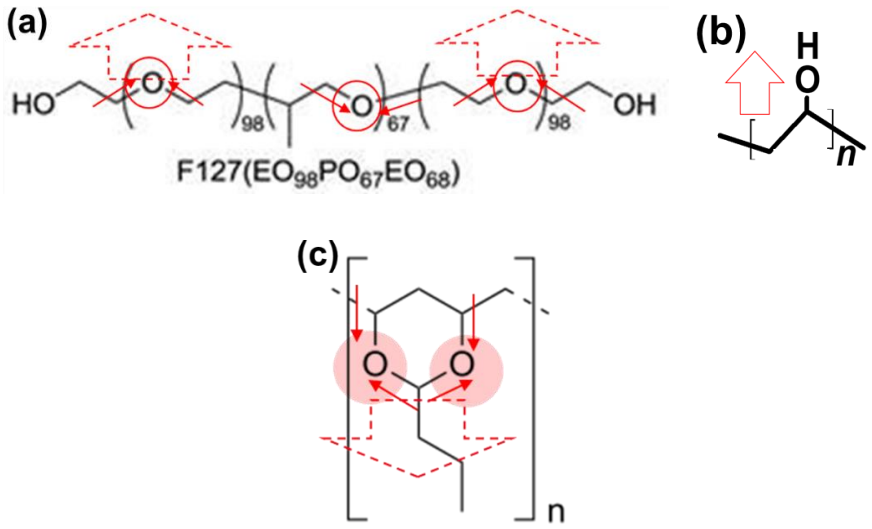

Fig. 3.2 Molecular formulas showing (a) F127, (b) PVA and (c) PVB and corresponding dipole moment (red arrow) caused by O-atoms.

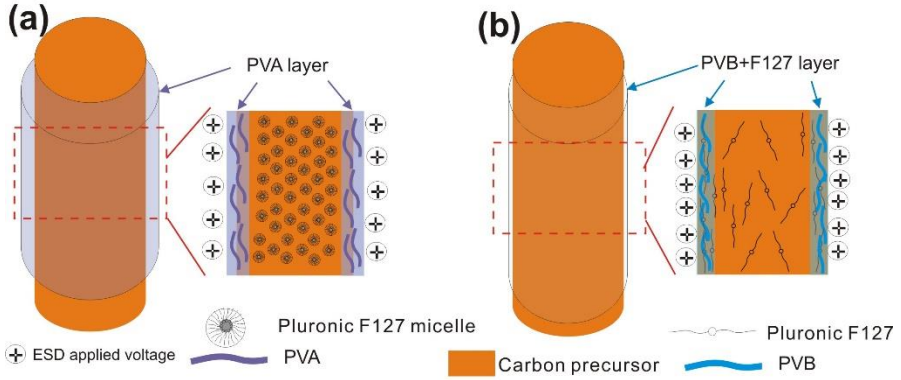

Fig. 3.3 Schematic drawings showing possible molecular arrangements in fibers made by PVA (a) and PVB (b) during ESD.

On the other hand, in case of PVA as shown in Fig. 3.2 (b), each O-atom is bonded with a C-atom and a H-atom and forms a hydroxyl group. Molecular dipole moment caused by the hydroxyl group becomes larger comparing to other two cases. Therefore, it is possible for PVA to form a protection layer that can prevent Pluronic F127 to be linear owing to the applied high voltage and Pluronic F127 micelles can be still survived. A same shielding effect by PVA layer in ESD process has also been reported by others [2].

3.1.2 MCFs made with different precursors/additive ratios

MCFs made with two different precursors/additive ratios were compared. In the previous section, MCFs with PVA were synthesized, and the ratio among carbon precursor resin, F127 and PVA was 2:1:1. Then, MCF-B was synthesized with the ratio of 1:1:1 as described in section 2.1.3.1 and section 2.1.4. The N_2 sorption isotherms and corresponding BJH plots are shown in Fig. 3.4 (a) and Fig. 3.4 (b), respectively.

As shown in Fig. 3.4 (a), the shape of N_2 sorption isotherms was similar between MCF-PVA and MCF-B although the first increase in N_2 adsorption was more significant with MCF-B in the low p/p_0 region. As mentioned in the previous chapter, this indicated MCF-B has more micropores, resulting in higher surface area, 670 m^2/g. In terms of mesopore volume, MCF-B had the significantly larger mesopore volume estimated the area under the curve in Fig. 3.4 (b) comparing to MCF-PVA.

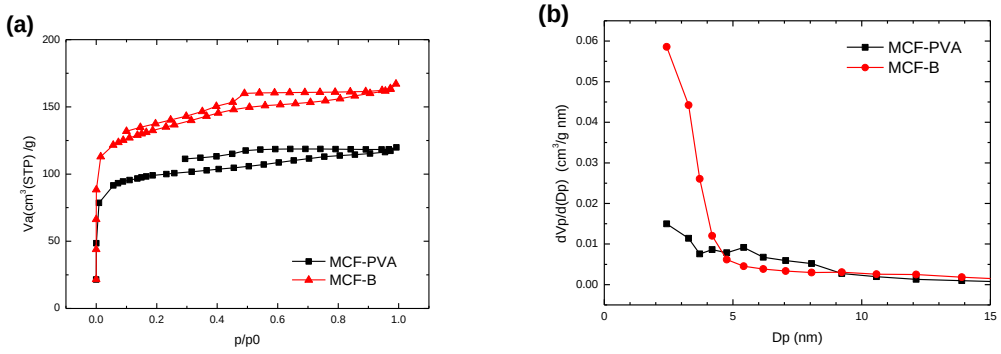

Fig. 3.4 (a) N_2 sorption isotherms and (b) corresponding BJH plots of MCF-PVA and MCF-B.

According to the literature [3], the bonding force between the surfactant and carbon precursor resin is mainly the hydrogen bonding, as shown in Fig. 3.5. In our case, the formation of H-bonding was not limited between the carbon precursor resin and Pluronc F127 surfactant and H-bonding was formed between Pluronic F127 surfactant and PVA. Therefore, the increase in precursor/additive ratio led to increase in the pores volume.

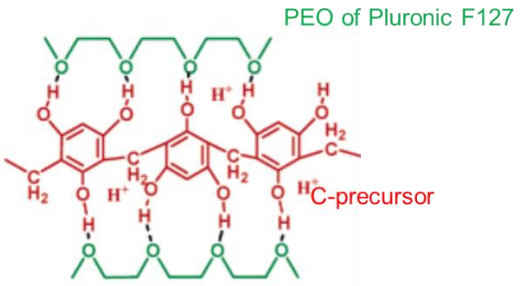

Fig. 3.5 A schematic diagram of H-bonding between the Pluronic F127 and carbon precursor resin.

3.1.3 MCFs made with different pH conditions

Three different MCFs made from precursor solutions with different pH, MCF-A, MCF-WA, and MCF-B, were made as described in section 2.1.3.

N_2 adsorption/desorption measurements were performed for MCF-A, MCF-WA and MCF-B, and N_2 sorption isotherms and corresponding BJH plots are shown in Fig. 3.6 (a) and Fig. 3.6 (b), respectively. All types of MCFs showed the type IV isotherm, indicating a mesoporous structure. The values of main pore diameters were 4-5 nm, 3-4 nm and 2-3 nm for MCF-A, MCF-WA, and MCF-B, respectively. Therefore, pore diameter decreased along with increase in pH of the precursor solution. Regarding BET surface area, MCF-A, MCF-WA and MCF-B revealed 370 m^2/g, 340 m^2/g, and 670 m^2/g, respectively. The increase in BET surface area for MCF-B was mostly likely owing to increase in micropores.

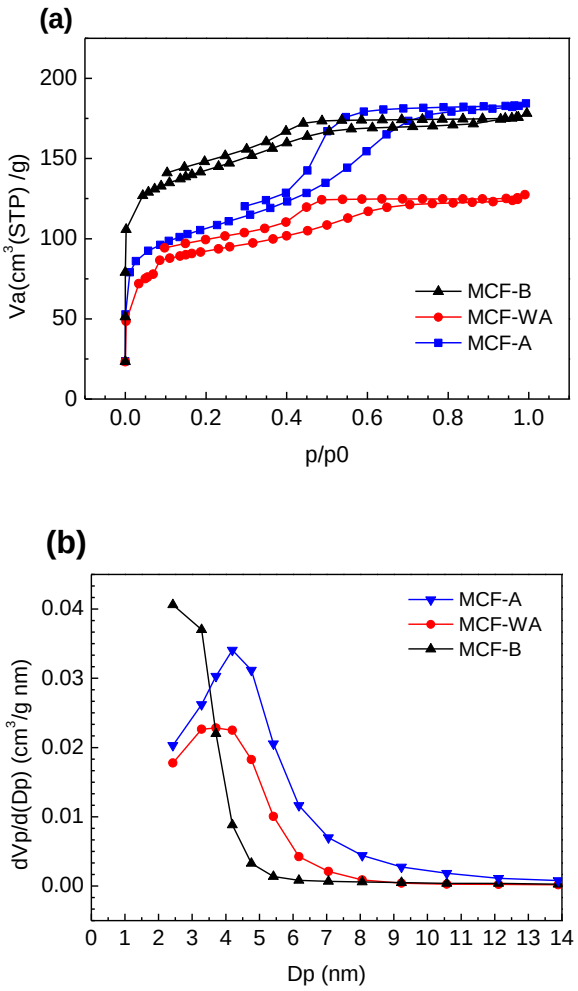

Fig. 3.6 (a) N_2 sorption isotherms and (b) corresponding BJH plots of MCF-A, MCF-WA and MCF-B.

According to Tanaka et al. [4], the size of mesopores is mainly determined by the size of surfactant micelles. Since the bonding between surfactant micelles and carbon precursors mainly consisted of hydrogen bondings as shown in Fig. 3.5, decrease in the number of hydrogen bondings in the basic condition was expected, which led to crushing of the micelles during ESD and then resulted in smaller pores.

In our purpose, MCFs should be designed to have larger mesopores in order to utilize them as supporting space of catalyst particles with a dimeter of 2-3 nm, in terms of good transportation of reactants and products. Since the further increase in acidity of the MCF precursor solution increased instability of the ESD process because of partially hydrolyzed of PVA [5], MCF-A with the largest pore diameter was chosen for further optimization of synthetic conditions and characterization in this chapter.

3.1.4 MCFs made with higher concentration of precursors

MCFs with higher concentration of precursors, MCF-HC, was made as described in section 2.1.3.4 and 2.1.4. N_2 adsorption/desorption measurement was performed for MCF-HC, and N_2 isotherms and corresponding BJH plot are shown with those of MCF-A and bulk MC are shown in Fig. 3.7.

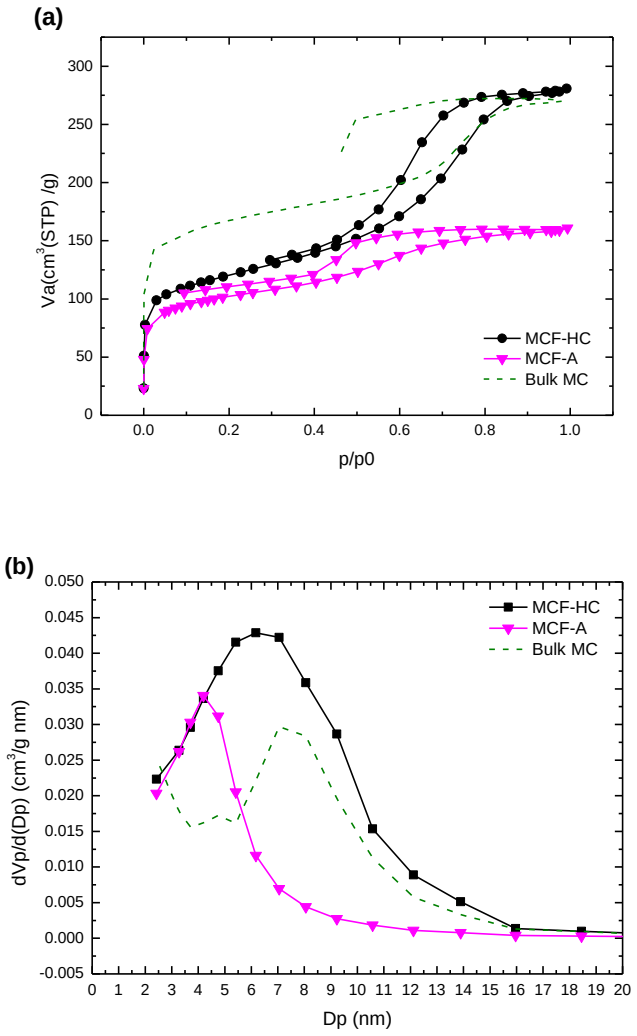

Fig. 3.7 (a) N_2 sorption isotherms and (b) corresponding BJH plots of MCF-HC, MCF-A and bulk MC.

According to the BJH plots, the major pore size of MCF-HC resulted in 6-7 nm, which was larger than the pore size of MCF-A and closer to the pore size of bulk MC. BET surface area of MCF-HC resulted in 427 m^2/g. In terms of mesopore volume,

MCF-HC had the largest mesopore volume estimated the area under the curve in Fig. 3.7 (b) among MCFs. Although the MCF-HC showed largest pore volume and diameter, the synthesis of MCF-HC was relatively difficult due to the higher polymer concentration. MCF-A was rather used for the following optimization process.

3.2 Optimization of the calcination process for MCFs

3.2.1 Evaluation of decomposing temperate of as-spun MCFs

TGA was performed for as-spun MCF-A under 150 sccm of N_2 and is shown in Fig. 3.8 with the corresponding 1st derivative curve. The inflection point in the 1st derivative curve represents the starting or ending points of decomposition reactions as seen in Fig. 3.8. The 1st derivative curve showed two main inflection points at 220 ^oC and 385 ^oC, where decomposing processes were started. These decomposition processes included decomposition of carbon precursors (carbonization of fibers), decomposition of PVA binder, and decomposition of Pluronic F127 (formation of mesopores). In order to understand the decomposition process occurred in these two temperature regions, 240 ^oC and 400 ^oC were used in the following characterization.

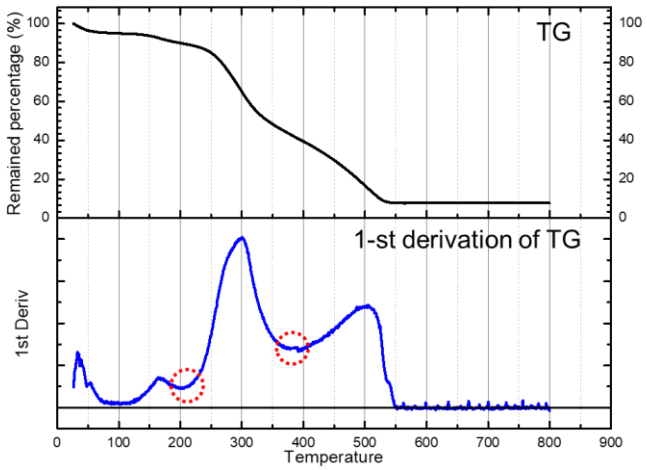

Fig. 3.8 The TGA result of as–spun MCF-A and its 1st derivative to temperature.

3.2.2 Evaluation of changes in crystallinity under different calcination conditions

For evaluation of the crystallinity, XRD was analyzed for MCF-A precursor fibers heat treated at 240 ^oC-3 h, 240 ^oC-3 h +400 ^oC-3 h, and 240 ^oC-3 h +400 ^oC-3 h +800 ^oC-3 h under N_2, and XRD patterns are shown in Fig. 3.9. Vulcan® XC-72, a common

carbon black material, was also evaluated as a reference. The obtained relatively broad peaks with low intensity were typical features of the amorphous structure of carbon materials. As shown in Fig. 3.9, Vulcan® XC-72 showed two prominent peaks at 24.5º (major) and 43.5º, indicating C (1 1 1) and C (2 0 0), respectively. The sample treated at 240 ºC only showed one major peak at 20.5º, where the C(1 1 1) plane was slightly shifted. Because of the incomplete carbonization at 240 ºC, lots of non-carbon atoms were still left, leading to larger d-spacing of carbon. With increasing the temperature of N_2 calcination, the major peak started shifting to larger 2θ. After additional N_2 calcination at 800 ºC calcination, the major peak was shifted to 22.0º, and the secondary peak started showing up at 43.5º, indicating that MCF-A heat treated at 800 ºC finally got the graphite-like structure.

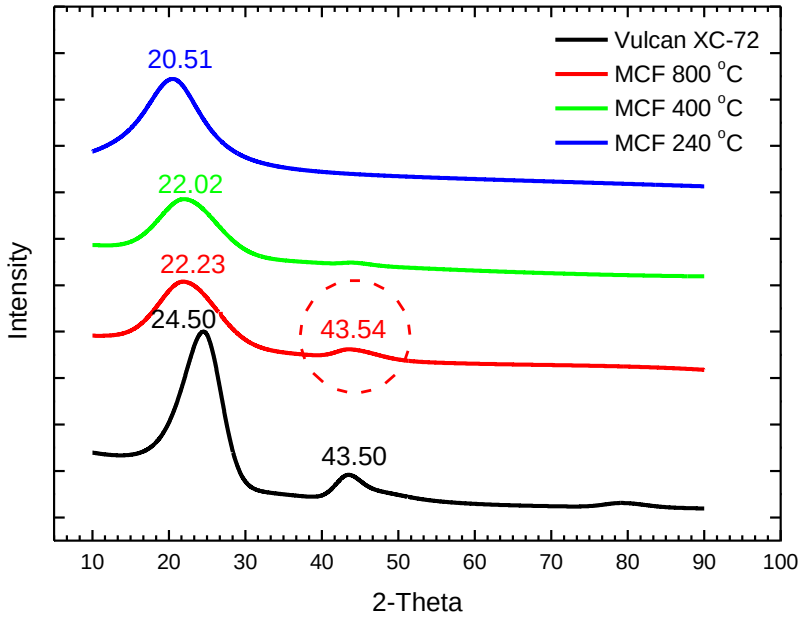

Fig. 3.9 XRD patterns of MCF-A precursor fibers treated with different calcination conditions and Vulcan® XC-72 as a reference.

3.2.3 Evaluation of changes in the C and H atomic percent under different calcination conditions

In order to evaluate C and H atomic percent, CHN analyses of MCF-A precursor fibers heat treated at different temperature were performed and their atomic percent of H and C are listed in Table 3.1. Here, in addition to heat-treatment up to 400 ºC and 800 ºC, samples treated up to 700 ºC and up to 900 ºC were also analyzed. As a result, the atomic percent of H decreased along with the increase in the calcination temperature. The atomic percent of C kept increasing until the calcination temperature reached to 800 ºC. Since further increase in carbon atomic ratio was not seen at 900 ºC, the calcination process up to 800 ºC was chosen as a carbonization condition in this study.

Table 3.1 CHN elemental analyze (H and C) of MCF-A precursor fibers treated with different temperature.

Heat treatment	H atom(%)	C atom (%)
None	6.29	57.90
240 ºC	6.96	59.05
240 ºC +400 ºC	4.03	76.63
240 ºC +400 ºC +700 ºC	1.21	81.24
240 ºC +400 ºC +700 ºC +800 ºC	0.91	86.8
240 ºC +400 ºC +700 ºC +800 ºC +900 ºC	0.76	86.16

3.2.4 Evaluation of changes in mesoporosity under different calcination conditions

In order to evaluate the mesoporosity, N_2 sorption measurements were performed for MCF-A precursor fibers heat treated at different temperature. Since the MCF-A heat treated at 240 ºC didn't show any mesopores. N_2 adsorption/desorption isotherms and corresponding BJH pore distribution of MCF-A precursor fibers treated at 400 ºC, 400 ºC +700 ºC, and 400 ºC +700 ºC +800 ºC are shown as Fig. 3.10.

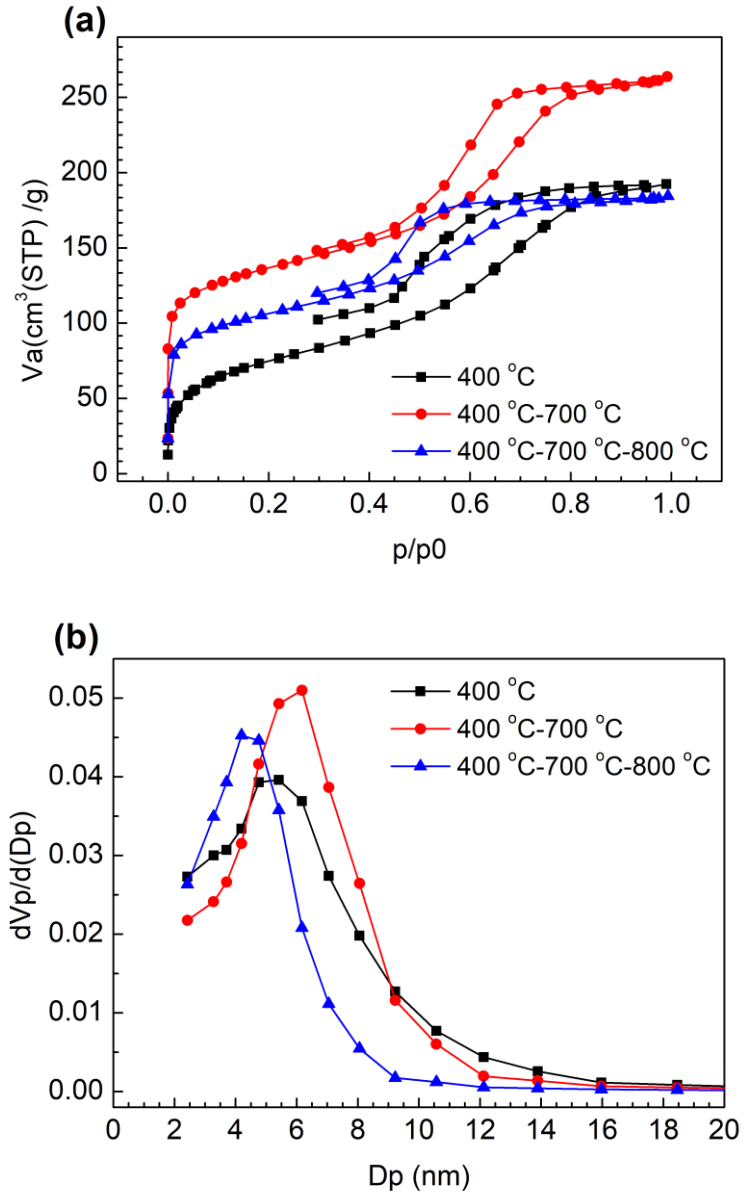

Fig. 3.10 (a) N_2 sorption isotherms and (b) corresponding BJH plots of MCF-A precursor fibers treated under different calcination conditions.

MCF-A precursor fibers treated at 400 ºC started adsorbing N_2, and the corresponding BET specific surface area and main pore diameter were 240 m^2/g and 5-6 nm, respectively. With the heat treatment with additional 700 ºC calcination, BET surface area and main pore diameter further increased to 490 m^2/g and 6-7 nm, respectively.

On the other hand, with further additional 800 ºC calcination, BET surface area and main pore diameter decreased to 380 m^2/g and 4-5 nm, respectively. This is probably owing to shrinkage by further removal of H and O atoms, which was also partly found from the CHN elemental analysis in the previous section. However, comparing to MCF-A obtained by direct heating from 400 ºC to 800 ºC as shown in Fig. 3.7, even though the main pore diameter did not change much, the pore volume roughly estimated by the area under the curve, was rather found to decrease when heating to 800 ºC directly from 400 ºC. Although pore diameter was larger with the heat treatment up to 700 ºC, higher carbonization degree obtained from further heating to 800 ºC was rather important as an electrocatalyst support for our study, and so the heat treatment up to 800 ºC was chosen in this study.

Based on the above results, carbonization of precursor fibers was optimized in the following; The first step is heating to 400 ºC with the rate of 2 ºC/min and keeping at 400 ºC for 3 h, the second step is heating to 700 ºC with the rate of 2 ºC /min and keeping at 700 ºC for 3 h, and then the final step is heating to 800 ºC with the rate of 1 ºC /min and keeping at 800 ºC for 6 h.

3.3 Characterization of MCFs

3.3.1 Observation of morphology of MCF-A, MCF-HC and MCF sheet

Morphology of MCF-A was evaluated by SEM and TEM and is shown in Fig. 3.11. As shown in Fig. 3.11 (a), the diameter of fibers was within the range from 500 nm to 2 μm. With high magnification imaging as shown in Fig. 3.11 (b), mesopores with the diameter around 4-5 nm were clearly observed on the surface of fibers with a random arrangement. These results proved that mesopores generated by our process were opened pore toward the fiber surface and usable as a catalyst metal support. In addition to the random arrangement of pores on the surface, as seen in Fig. 3.11 (c), hexagonally ordered mesopores were rather confirmed in the TEM image. The resulting size of pore diameter was well matched to that obtained from N_2 adsorption measurements.

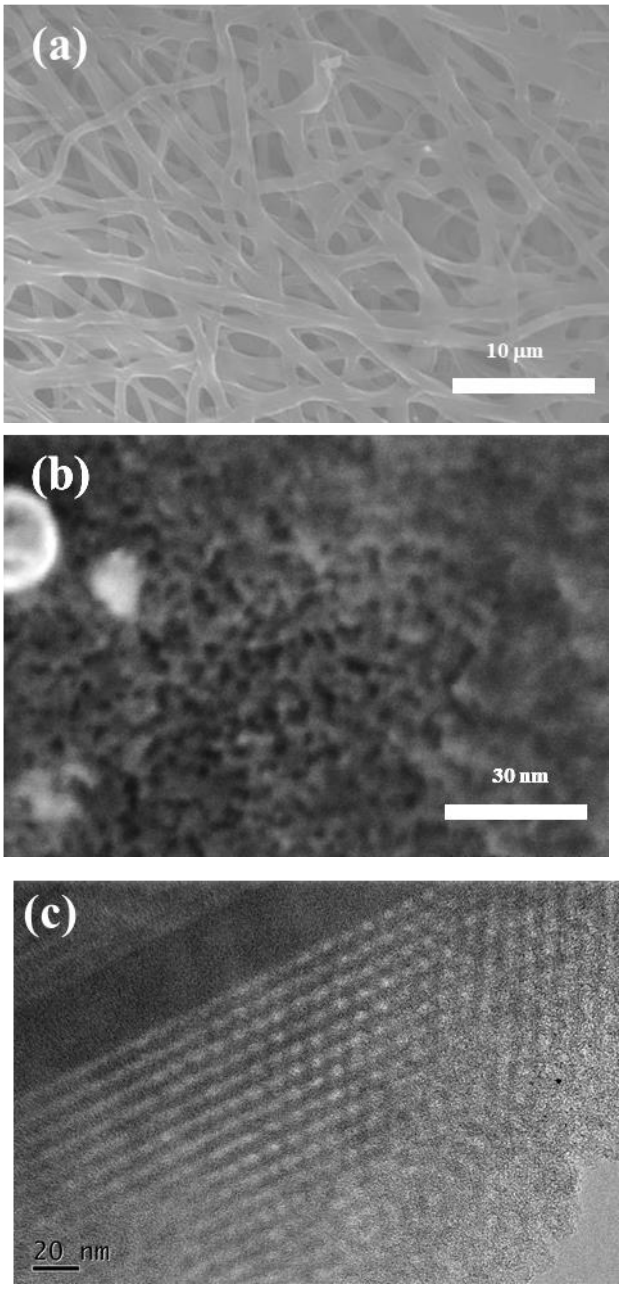

Fig. 3.11 (a) SEM, (b) high magnification SEM, and (c) TEM images of MCF-A.

Similarly, morphology of MCF-HC was evaluated and is shown in Fig. 3.12. As seen in he Fig. 3.12 (a), the fiber diameter of MCF-HC was from 0.5 to 2 μm. With the high-resolution image in blue-circled area shown in Fig. 3.12 (b), mesopore were easily found on the surface of fibers. According to the STEM image of MCF-HC in red-circled area shown in Fig. 3.12 (c), the arrangement of mesopores was found to have the hexagonal arrangement, and the pore diameter was around 6 nm, which was matched to the that obtained from N_2 adsorption measurements.

Similar morphology was also observed for other MCFs. Although, the size of mesopores was different among types of MCFs, those pores was three dimensionally connected.

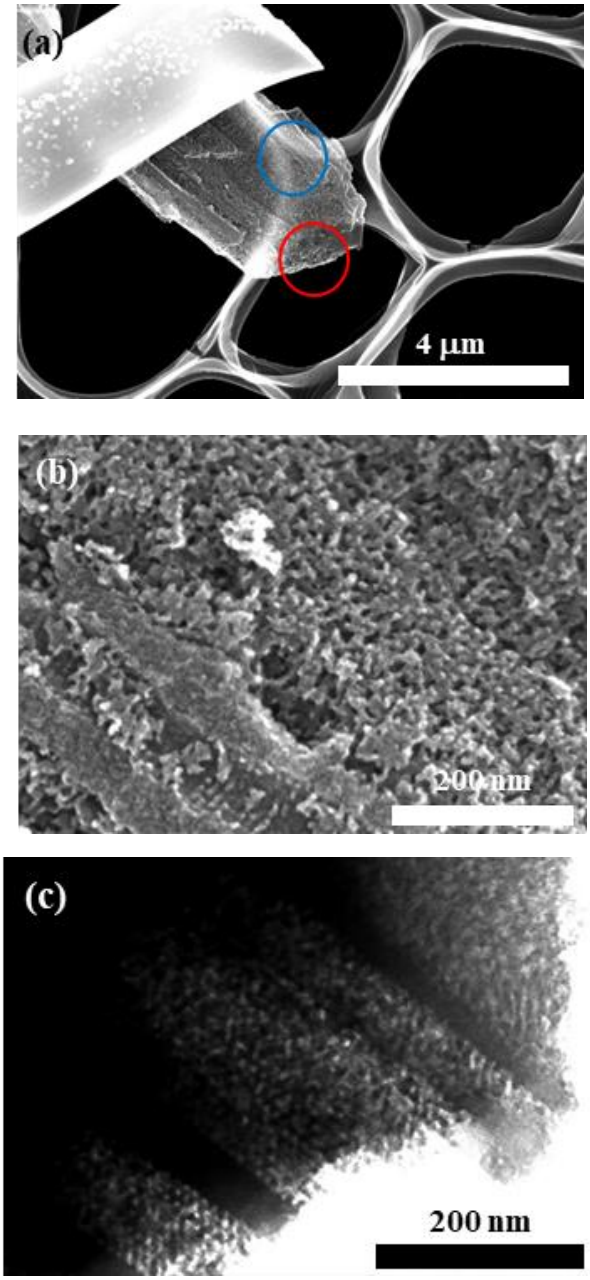

Fig. 3.12 (a) SEM, (b) high magnification SEM, and (c) TEM images of MCF-HC.

Furthermore, morphology of a single MCF-HC sheet (named just as MCF sheet) was evaluated and surface and cross-sectional views are shown in Fig. 3.13. Here, the sheet was 0.4 mgC/cm^2. From the Fig. 3.13 (a), fibers with 2-3 µm diameter and several µm pores were found from the surface SEM image, and the thickness of a single layer

MCF-sheet was found to be about 1-2 μm from the cross-sectional SEM image.

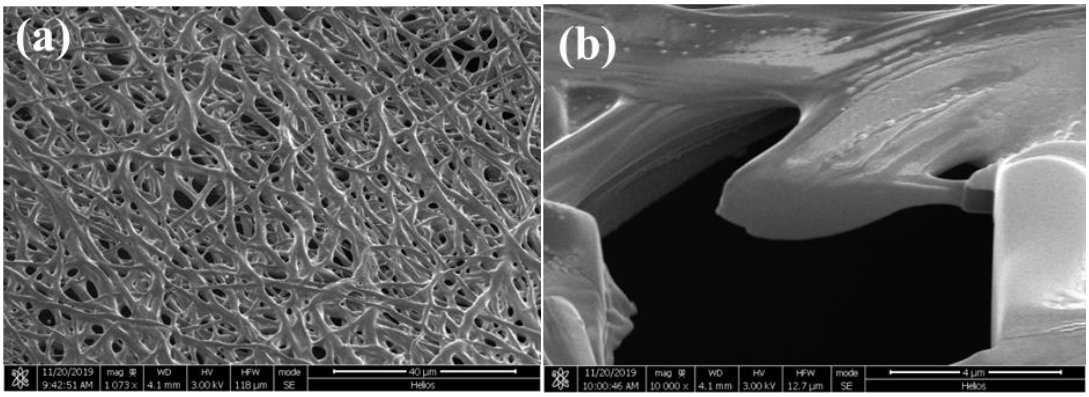

Fig. 3.13 (a) surface and (b) cross-sectional SEM images of a single MCF sheet (0.4 mgC/cm^2).

3.3.2 Evaluation of MCF-A thin films: resistance toward compression

Since the fiber structure is expected to have an advantage when MCF is applied to devices, MCF-A ball-milled at 450 rpm was spray-printed on the Nafion 212 membrane as a layer, and the resistance to compression of 251 N/cm^2 under a cell holder for regular current-voltage performance measurements was evaluated, as explained in section 2.4.3.

Similarly, the bulk MC layer was also prepared and evaluated. The cross-section of MCF-A layer and bulk MC layer were fabricated and observed using a FIB-SEM technique and are shown in Fig. 3.14. According to the thickness measured before and after the compression, the change in the MCF-A layer was about 11.5 % (17.1 to 14.8 μm) and resulted in lower than the change in MC layer, 14.3 % (15.0 to 13.3 μm).

The existence of fiber morphology most likely provided a certain elasticity in compression test, resulting in restoring more the thickness of MCF-A after the compression.

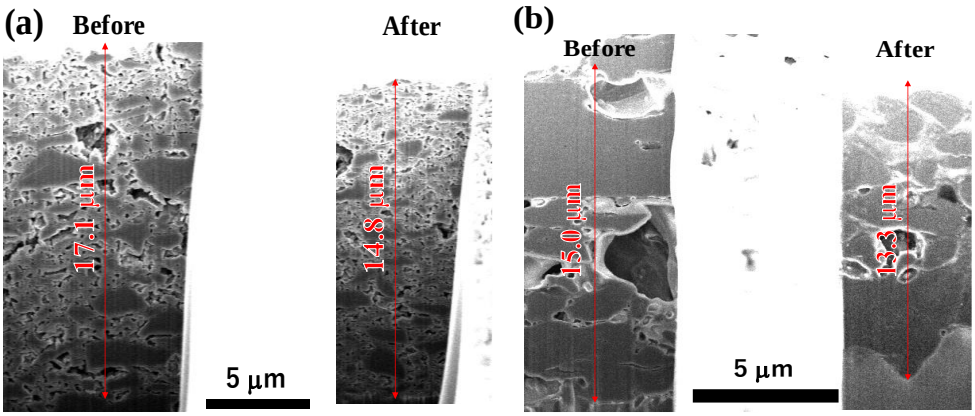

Fig. 3.14 Cross-sectional FIB-SEM observation before and after the compression test of (a) bulk MC and (b) 450 rpm ball-milled MCF-A thin layers.

3.3.3 Evaluation of MCF-A thin films: through plane electronic resistance

In order to evaluate expected increase in electric conductivity with fiber structure, the through-plane conductivity of MCF-A thin films was evaluated by spray-printing on the GDL 25 BC carbon paper as a layer. Detail of experiments were described in 2.4.5. The through-plane conductivity of both bulk MC and Vulcan® XC-72 thin films were also evaluated for the comparison. For MCF-A, three thin films, MCF-A ball-milled with 450 rpm (MCF-A-450), MCF-A ball-milled with 800 rpm (MCF-A-800), and MCF-A without ball milling (fine MCF-A) were evaluated. Obtained through-plane conductivity is shown in Fig. 3.15. Bulk MC and Vulcan® XC-72 both showed a +20 mΩ higher than the baseline, but MCF-A-800 and MCF-A-450 showed +12 mΩ and +8 mΩ, respectively. According SEM images shown in Fig. 3.16, MCF-A-450 (Fig. 3.16 (b)) was found to have longer fibers than MCF-A-800 (Fig. 3.16 (a)). Therefore, the diffence between MCF-A-450 and MCF-A-800 came from difference in the degree of the fiber structure. When the fiber structure more remained without ball-milling, through-plane conductivity of fine MCf-A resulted in the lowest resistance, +3 mΩ. Consequently, fiber structure was found to have an adavantage in electric condcutivity especially if fibers were longer and connected.

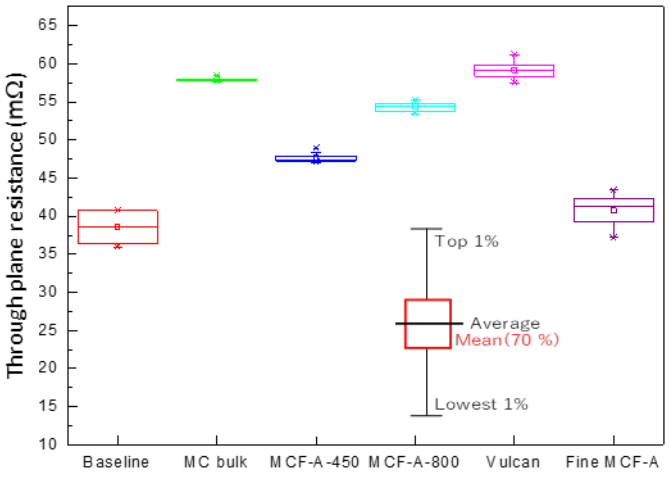

Fig. 3.15 Through plane electric resistance of thin films made by different carbon samples.

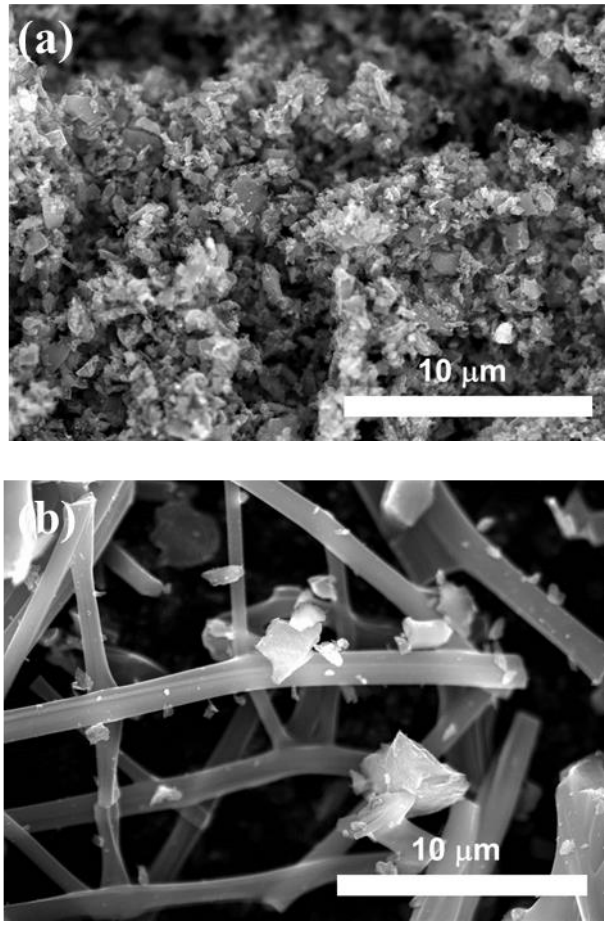

Fig. 3.16 MCF with (a) 800-rpm ball-milling and (b) 450-rpm ball-milling.

3.3.4 Evaluation of fundamental electrochemical properties of MCF-A

Electrochemical properties of MCF-A and other reference carbon materials were evaluated by CV and CDC measurements as described in section 2.3.6. CV curves were obtained within the voltage range from 0.05 V to 1.15 V (vs RHE) with the scan rate of 50 mV/s and shown in Fig. 3.17. All the CV curves had slightly-distorted rectangular shape. Some of them showed a broad peak around 0.7 V, resulting from the adsorption of O atom on the carbon surface. According to the literature [6], carbon materials derived from the phenolic resin have oxygen-containing functional groups on their surface and show the similar CV curve, acting as a pseudo-capacitor.

Specific capacitance (C_p) of MCF-A, MC, Vulcan® XC-72 and conventional CNF were 56.5 F/g, 62.4 F/g, 47.9 F/g and 15.6 F/g, respectively, based on the method of calculation as described in section 2.3.6. The order of C_p within four samples was found to be reasonable based on their BET surface area obtained from N_2 sorption measurements, 380 m^2/g, 600 m^2/g, 220 m^2/g, and 130 m^2/g, for MCF-A, MC, Vulcan® XC-72 and CNF, respectively. The reason of lowest C_p and BET surface area for CNF might be due to its defect-less structure of the particular sample in this study made from CVD process.

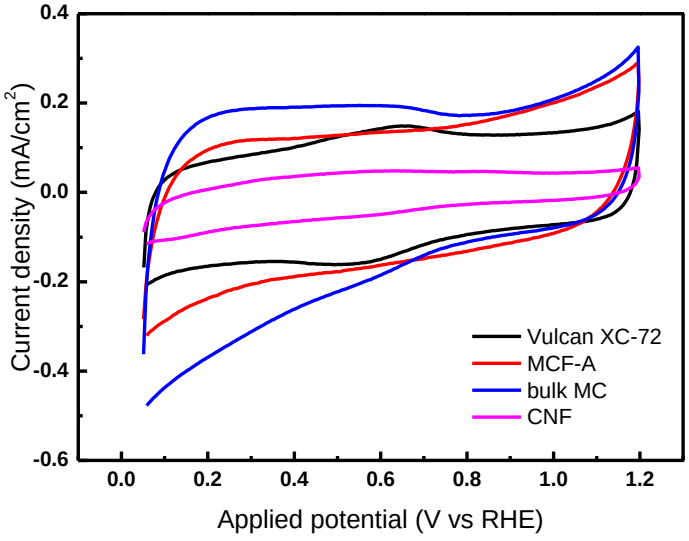

Fig. 3.17 CVs of MCF-A, bulk MC, Vulcan® XC-72, and CNF.

CDC measurements were performed by applying charging current of 25 μA for different carbon materials and are shown in Fig. 3.18 (a). Discharge specific capacitance (C_{des}) calculated in different charging current was also plotted in Fig. 3.18 (b). The C_{des} decreased with the increase in the charging current for all samples, which was a common feature of carbon based materials. CDC response of voltage under different charging current was further analyzed and is shown in Fig. 3.19. The hysteresis of voltage in the potential range near the end of a charging/ discharging process was found in the MCF-A and MC cases. Since increase in voltage during the CDC process was related to electron transfer resistance and ion diffusion resistance. The resulting hysteresis might be the feature of hydrophobic mesopores.

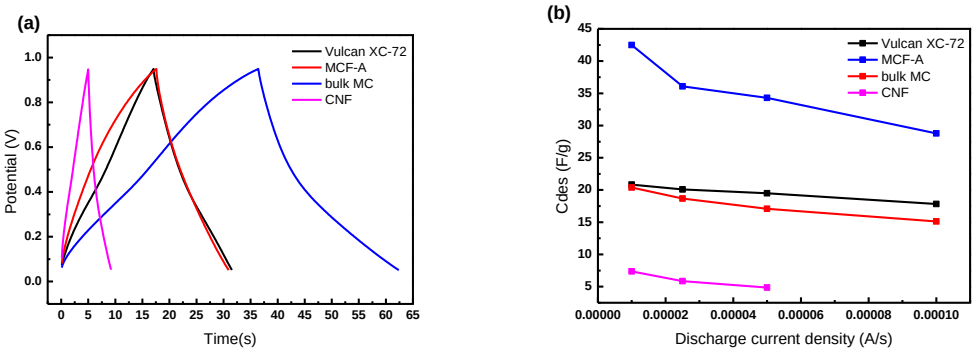

Fig. 3.18 (a) CDC response of voltage under applying 25 μA and (b) discharge specific capacitance in different charging current for different carbon materials.

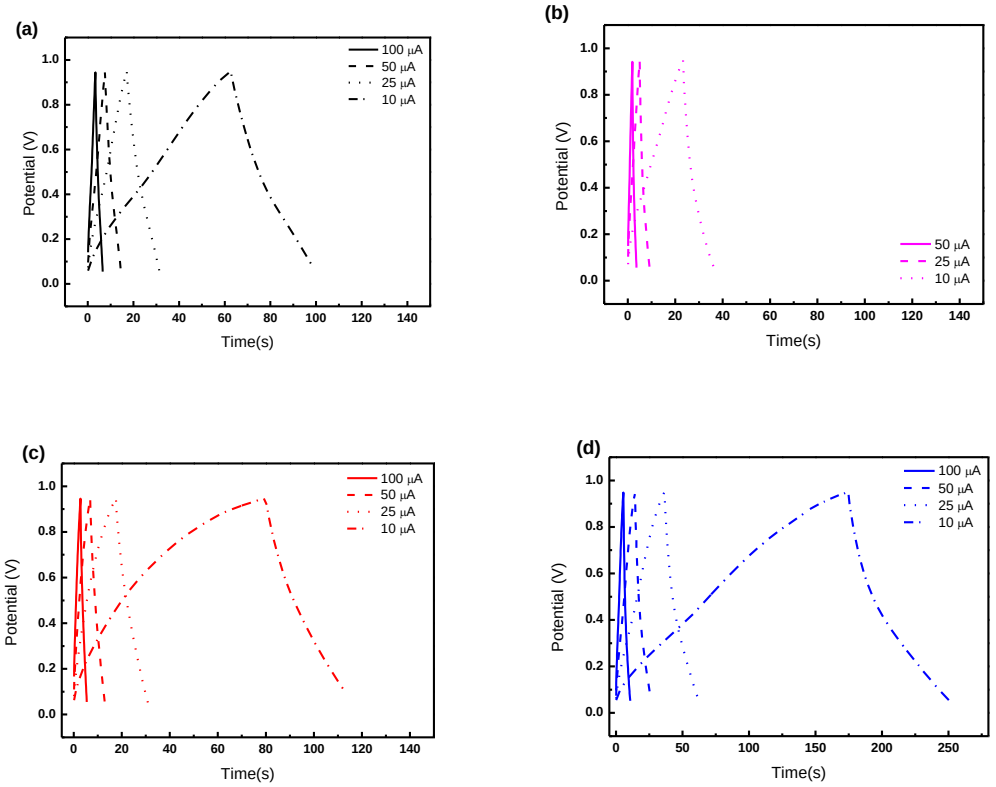

Fig. 3.19 CDC response of voltage of Vulcan XC-72 (a), CNF (b), MCF-A (c) and bulk MC (d) under different charging current.
X-axis for (a) (b) (c): 0~140 s, X-axis for (d): 0~275 s.

3.4 Conclusion

In this chapter, optimization of MCFs were fully performed in terms of mesoporosity and carbonization degree, while MCFs were characterized using several characterization methods. Optimum heat treatment condition was determined as following: The first step is heating to 400 ºC with the rate of 2 ºC/min and keeping at 400 ºC for 3 h, the second step is heating to 700 ºC with the rate of 2 ºC /min and keeping at 700 ºC for 3 h, and then the final step is heating to 800 ºC with the rate of 1 ºC /min and keeping at 800 ºC for 6 h.

Among varies MCFs synthesized in this study, MCF-A and MCF-HC were chosen as MCFs with large pores diameter and pore volume. With MCF-A, electrochemical characterization was performed. As a result, MCFs had better electric conductivity and better elasticity comparing to other powder-carbon materials.

List of references

[1] U. Stachewicz, C. A. Stone, C. R. Willis, A. H. Barber, Charge assisted tailoring of chemical functionality at electrospun nanofiber surfaces, J. Mater. Chem., 22, 22935-22941 (2012).

[2] Y. Badhe, K. Balasubramanian, Nanoencapsulated core and shell electrospun fibers of resorcinol formaldehyde, Ind. Eng. Chem. Res., 54, 7614-7622 (2015).

[3] C. Liang, S. Dai, Synthesis of mesoporous carbon materials via enhanced hydrogen-bonding interaction, J. Am. Chem. Soc., **128**, 5316-5317 (2006).

[4] S. Tanaka, A. Doi, N. Nakatani, Y. Katayama, Y. Miyake, Synthesis of ordered mesoporous carbon films, powders, and fibers by direct triblock-copolymer-templating method using an ethanol/water system, Carbon, **47**, 2688-2698 (2009).

[5] W. K. Son, J. H. Youk, T. S. Lee, W. H. Park, Effect of pH on electrospinning of poly(vinyl alcohol), Mater. Lett., **59**, 1571-1575 (2005).

[6] D. Tashima, E. Yamamoto, N. Kai, D. Fujikawa, G Sakai, M. Otsubo, T. Kijima, Double layer capacitance of high surface area carbon nanospheres derived from resorcinol–formaldehyde polymers, Carbon, **49**, 4848-4857 (2011).

CHAPTER 4

Characterization of Pt Deposited MCFs (Pt/MCFs)

Chapter 4 : Characterization of Pt Deposited MCFs (Pt/MCFs)

Introduction

In this chapter, characterization of Pt/MCFs were fully introduced. This chapter was separated into two major sections; 4.1 Material characterization, and 4.2 Electrochemical characterization.

4.1 Material characterization

4.1.1 Evaluation of the weight percentage of Pt on MCFs

Pt deposition on bulk MC and MCFs was as described in section 2.1.5. The wt. % deposition of Pt on supports, such as bulk MC, MCF-PVA, MCF-B, MCF-A, and MCF-HC, was evaluated by TGA. As mentioned in section 3.1.2, MCF-PVA and MCF-B had the similar pore diameter but the pore volume of MCF-B was 5–times larger than MCF-PVA. On the other hand, MCF-B and MCF-A had the similar pore volume but MCF-A had the larger pore diameter, 4.5 nm, than MCF-B, 2 nm. MCF-HC had largest pore diameter, 7 nm, and largest pore volume.

Changes in wt.% of Pt/Bulk MC, Pt/MCF-PVA, Pt/MCF-B, Pt/MCF-A, and Pt/MCF-HC along with increase in temperature is shown in Fig. 4.1. Pt/MCF-PVA and Pt/MCF-B had a similar residential wt.%, suggesting about 12-13 wt.% Pt deposition. On the other hand, Pt/MCF-A and Pt/MCF-HC showed much high wt.% Pt deposition, 28 wt.%, which was almost the same wt.% Pt in Pt/bulk MC.

However, the wt.% Pt deposition on MCF sheet was decreased to only 10-14 wt.%, about a half as the substrate was changed from the powder to the sheet. The low wt.% Pt deposition on MCF sheet might due to the poor diffusion of the Pt precursor solution into the three dimensional structure of fine fibers with the diameter of 1 to 2 μm.

Consequently, pore volume didn't influence on the amount of wt.% Pt deposition. However, pore diameter rather influenced on the amount of Pt deposition. With the larger pore diameter, wt.% Pt deposition increased most likely because the better diffusion of the Pt precursor solution within the mesopores during the synthesis.

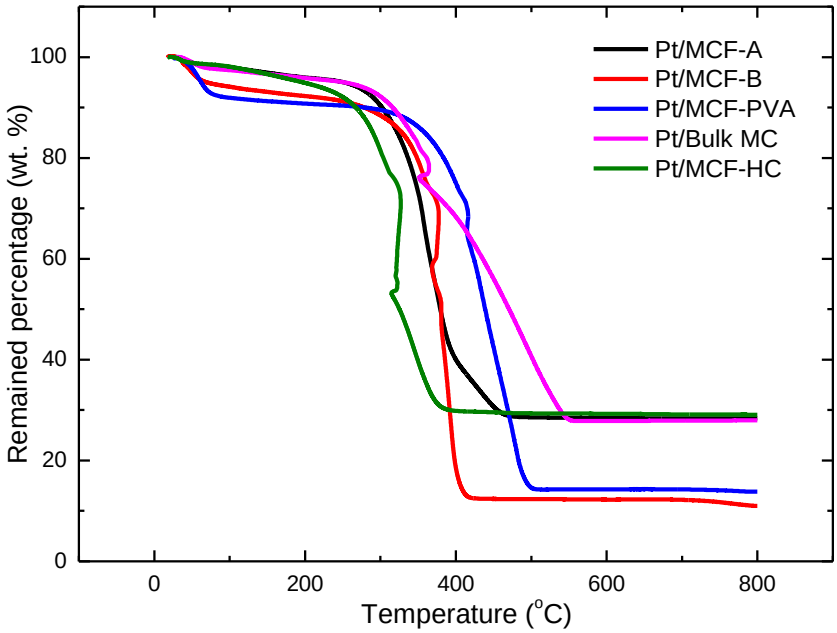

Fig. 4.1 Changes in wt.% of various Pt/carbon materials obtained by TGA.

4.1.2 Evaluation of morphology of Pt/MCFs

SEM observation of 14 wt.% Pt/MCF-PVA, 13 wt.% Pt/MCF-B, 28 wt.% Pt/MCF-A, and 26 wt.% Pt/bulk MC were done and are shown in Fig.4.2. As seen in Fig. 4.2 (b), serious agglomeration of Pt particles on the surface of fibers was seen in 14 wt.% Pt/MCF-PVA in comparing to 13 wt.% Pt/MCF-B as shown in Fig. 4.2 (d). In the Pt deposition process, pore structure usually worked as anchor point for Pt deposition. In this case, higher pore volume, represented that more pores were available as anchor points, led better dispersion of Pt particles.

On the other hand, 26 wt.% Pt/bulk MC and 28 wt.% Pt/MCF-A revealed the structure with mesopores and some Pt particles as shown in Fig. 4.2 (e), (f) and Fig. 4.2 (g), (h), respectively. Therefore, STEM observation was further performed for 26 wt.% Pt/bulk MC and 28 wt.% Pt/MCF-A.

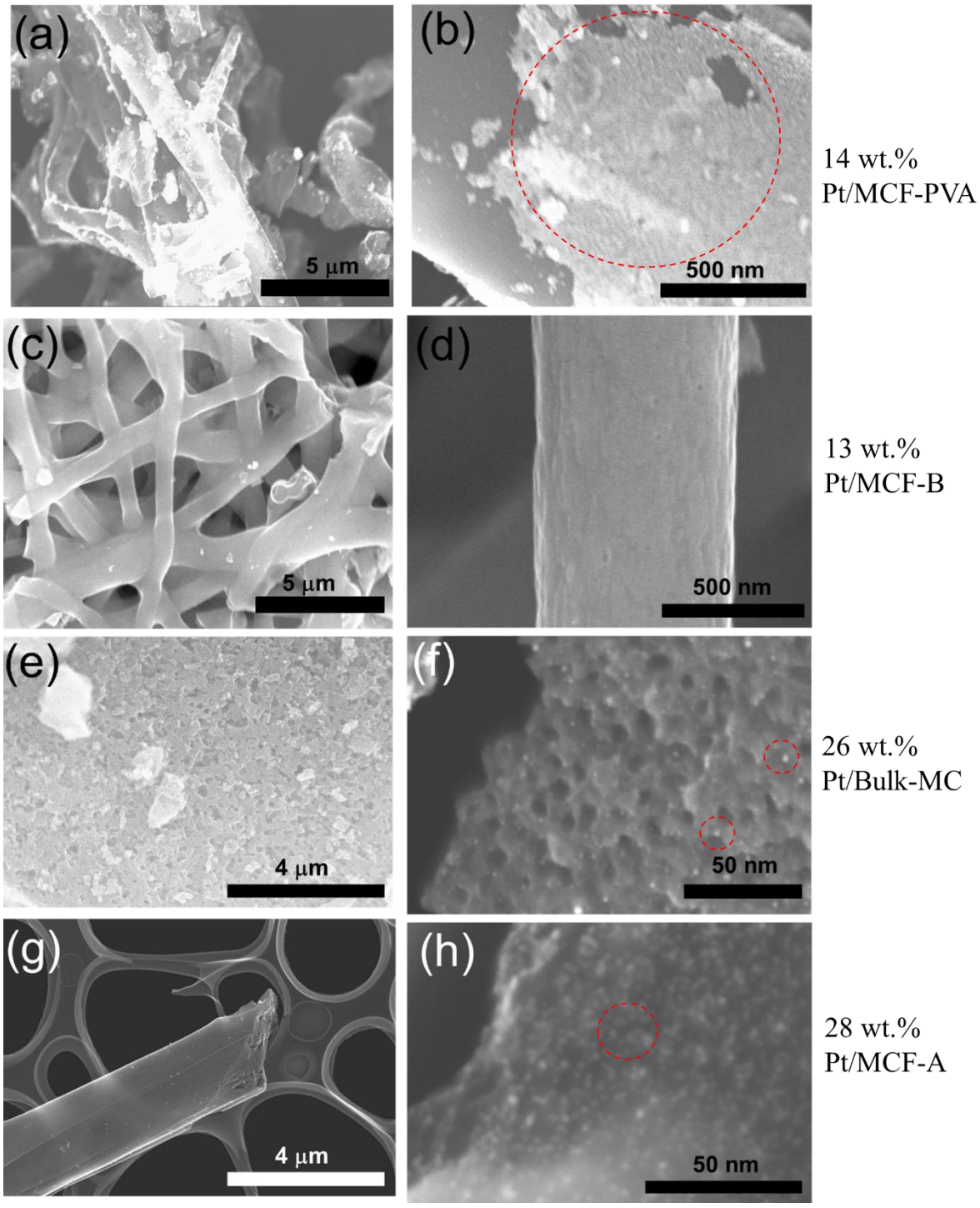

Fig. 4.2 SEM images of (a), (b) 14 wt.% Pt/MCF-PVA, (c), (d) 13 wt.% Pt/MCF-B, (e), (f) 26 wt.% Pt/bulk MC, and (g), (h) 28 wt.% Pt/MCF-A.
(a) (c) (e) (g): lower magnification. (b) (d) (f) (h): higher magnification.

SEM/STEM images of 28 wt.% Pt/MCF-A are shown in Fig. 4.3. From a transmitted image as shown in Fig. 4.3 (b), lots of Pt particles (black spots) were found. The number of Pt nanoparticles resulted in much less in the surface image than in the transmitted image. Furthermore, Pt particles were believed to be aligned along the channels since Pt nanoparticles showed parallel lines, as seen in Fig. 4.3 (b). Therefore, there were many Pt nanoparticles successfully encapsulated within the mesopores of fibers.

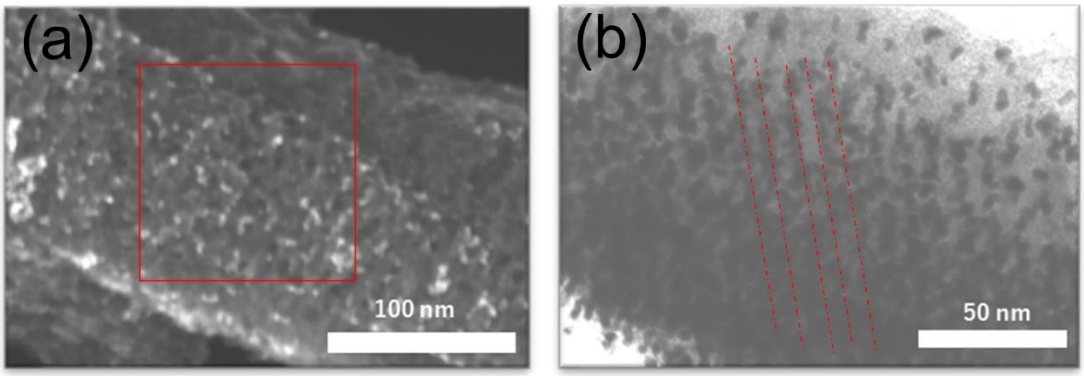

Fig. 4.3 SEM/STEM images of 28 wt.% Pt/MCF-A.

Similar morphology was observed for 28 wt.% Pt/MCF-HC, too. Therefore, Pt/MCF-A and Pt/MCF-HC had a highest deposited Pt wt. % and good dispersion of Pt particles among Pt/MCFs. Furthermore, the size of Pt particles in 28 wt.% Pt/MCF-A was evaluated by high resolution STEM as shown in Fig 4.4. For the similar observation was done for 26 wt.% Pt/bulk MC. The estimated average particle size for 26 wt.% Pt/bulk MC and 28 wt.% Pt/MCF-A were 3.2 nm and 4.0 nm, respectively. Resulting larger Pt particles size in 28 wt.% Pt/MCF-A might be due to the smaller mesopores of MCF-A. Agglomeration of Pt particles might due to the migration of one to the other, which was probably enhanced by increased heat transfer from the wall of mesopores with narrow channels during N_2 calcination process.

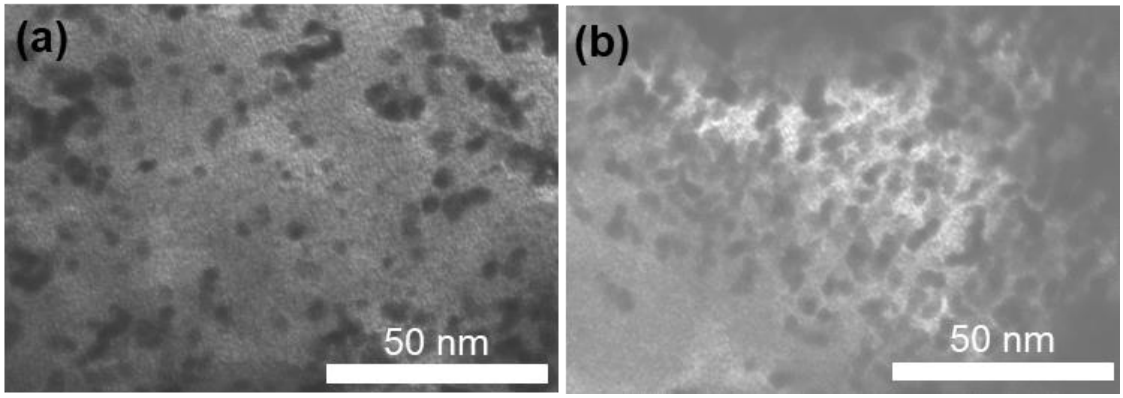

Fig. 4.4 STEM images of (a) 26 wt.% Pt/bulk MC and (b) 28 wt.% Pt/MCF-A.

4.1.3 Evaluation of mesoporosity changes before and after Pt deposition

In order to evaluate the change in mesoporosity before and after Pt deposition, 28 wt.% Pt/MCF-A was chosen among of Pt/MCFs, and N_2 adsorption/desorption measurements were performed. N_2 sorption isotherms and corresponding BJH plots of MCF-A and 28 wt.% Pt/MCF-A are shown in Fig. 4.5 (a) and Fig. 4.5 (b), respectively. After Pt deposition, the area under the pore distribution curve decreased, meaning that the pore volume decreased. This result also indicated that some Pt particles were successfully encapsulated within the mesopores.

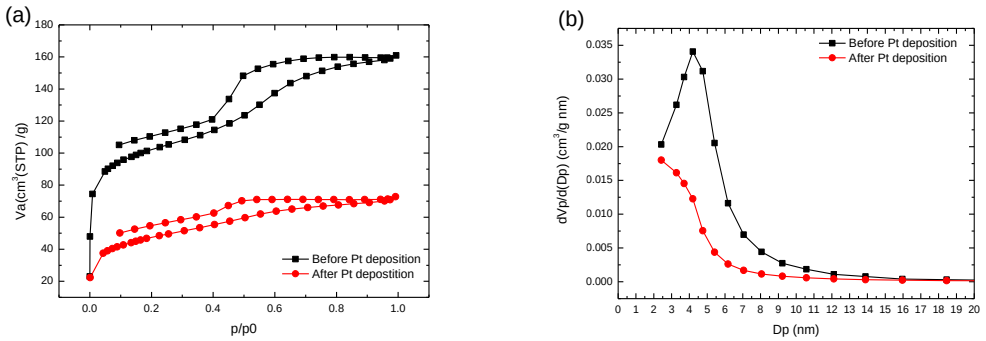

Fig. 4.5 (a) BET isotherms and (b) corresponding BJH plots of MCF-A before and after Pt deposition.

4.1.4 Evaluation of crystallinity

The Pt crystalline size was further evaluated by XRD. Fig. 4.6 indicates XRD patterns of 26 wt.% Pt/bulk MC, 28 wt.% Pt/MCF-A, and TKK 46 wt.% Pt/KB, which

was used as a reference. Regarding to Pt related peaks, four peaks at 39°, 45°, 68° and 82°, corresponding to (111), (200), (220), and (311), respectively, were seen for all samples. The Pt crystalline size was 3.2 nm, 3.0 nm and 2.1 nm for Pt/MCF, Pt/MC and Pt/KB, respectively, which was obtained from Pt (111) by using Scherrer's equation [1]. To be used as catalyst, the larger Pt particle size might lead lower surface area, but the further smaller particle size might also cause easier migration of Pt particles. The size of Pt particle size was controlled to between 2-3 nm in this study. Regarding the carbon related peak, C (111) peak was seen for Pt/MC samples, but this peak was not clear for Pt/KB. The reason was considered as that KB was amorphous and also Pt (111) was rather large owing to more Pt deposition like 46 wt.%.

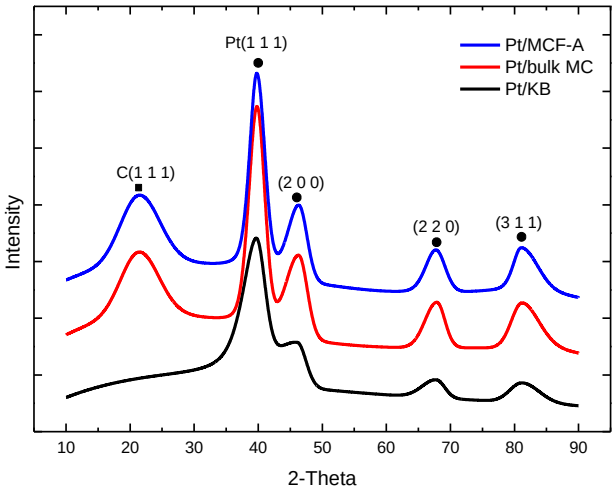

Fig 4.6 XRD patterns of TKK 46 wt.% Pt/KB, 26 wt.% Pt/bulk MC and 28 wt.% Pt/MCF-A.

Even though Pt particles of 28 wt.% Pt/MCF-A were larger in the STEM image in section 4.1.2, 26 wt.% Pt/bulk MC and 28 wt.% Pt/MCF-A had a similar Pt crystal size from XRD, which was 3.1 nm, suggesting that closely staying Pt particles in the narrow mesopores gave larger Pt particles images on STEM. Currently, the Pt particle size in Pt/MCF-A, 3.1 nm, was close to the diameter of the mesopores, 4-5 nm. In order to obtain more space within mesopores, the reduction of Pt particle size of Pt/MCF-A was tried by changing the heat treatment condition.

The changes in the heat treatment condition was described in section 2.1.5. From STEM images shown in Fig. 4.7, Pt particle size was found to slightly decrease without the heat treatment at 240 °C. Reduced self-diffusion of Pt particles followed by

enlargement of particles most likely occurred during the heating process.

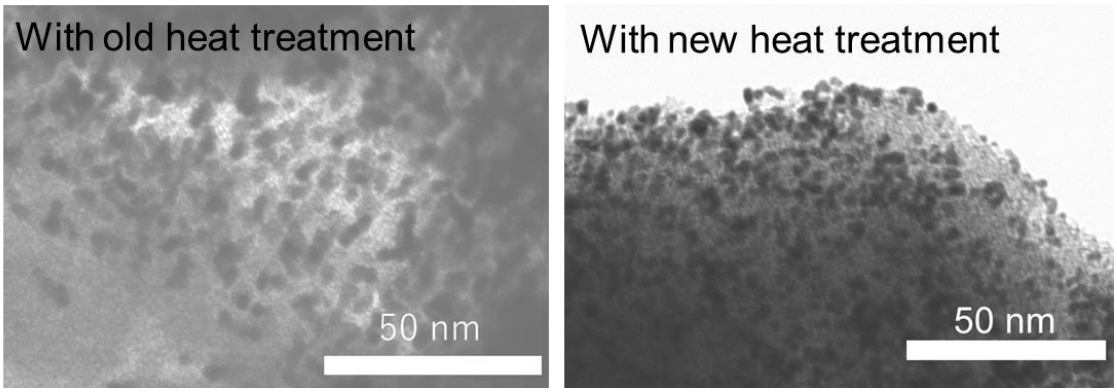

Fig. 4.7 STEM images of original Pt/MCF-A and modified Pt/MCF-A.

For further evaluation of the size of Pt particles, mean size distribution and average size of Pt particles in modified Pt/MCF-A were 2.8-3.5 nm and 3.1 nm, respectively, while they were 3.4-4.8 nm and 4.4 nm, respectively, in original Pt/MCF-A as shown in Fig. 4.8 (b).

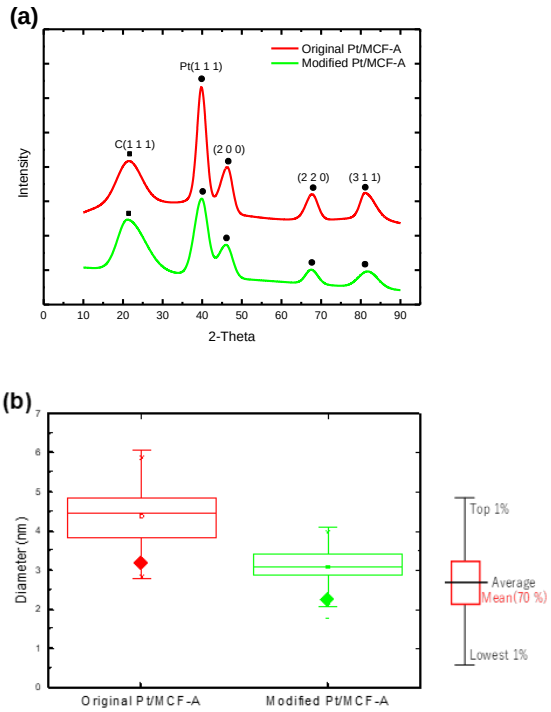

Fig. 4.8 (a) XRD patterns of original Pt/MCF-A and modified Pt/MCF-A, and (b) Pt particle size obtained from STEM images (bar with the range) and Pt(1 1 1) peak in XRD patterns (square).

4.2 Electrochemical characterization

Electrocatalysts selected for electrochemical evaluation in this section was summarized in Table 4.1.

Table 4.1 Electrocatalysts evaluated in this section

Name	Detail
Pt/MCF-PVA	with 14 wt. % Pt on low pore volume MCFs
Pt/MCF-B	with 13 wt.% Pt on high pore volume MCFs
Pt/MCF-A	with 28 wt.% Pt, with modified Pt particle size
Pt/bulk MC	with 26 wt.% Pt, used as a reference
TKK Pt/KB	with 46 wt.% Pt, used as a reference

4.2.1 Evaluation of ECSA

CV curves of Pt/MCF-PVA, Pt/MCF-B, Pt/MCF-A, Pt/bulk MC and Pt/KB in Table 4.1 were obtained and are shown in Fig 4.9.

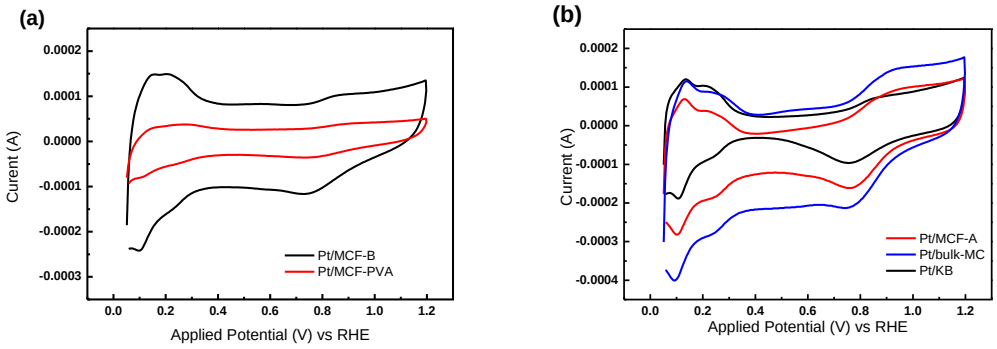

Fig. 4.9 CVs of (a) Pt/MCF-PVA and Pt/MCF-B and (b) Pt/MCF-A, Pt/bulk MC and Pt/KB.

According to CVs results in Fig. 4.9 (a), 13 wt.% Pt/MCF-B showed clear adsorption/desorption of H-atom and O-atom in the voltage region of 0.1-0.3 V and 0.7-1.2 V , respectively comparing to Pt/MCF-PVA. Corresponding ECSAs calculated from the H-atom adsorption region of Pt/MCF-B and Pt/MCF-PVA were 34.83 m^2/g and 6.12 m^2/g, respectively. The difference in ECSA of Pt suggested the different dispersivity of Pt particles. The better Pt dispersion in Pt/MCF-B resulted in a larger ECSA.

On the other hand, CV curves of Pt/MCF-A, Pt/ bulk MC and Pt/KB as shown in Fig. 4.9 (b) also showed clear peaks of adsorption/desorption H-atom and O-atom. The difference in the double layer was due to different amount of carbon, as well as BET surface area of carbon, on the working electrode. Since the amount of Pt was kept on 17.3 μgPt/cm^2, in case of high relative percent Pt deposition, the double layer of Pt/KB resulted in smaller.

The difference of the double layer between Pt/MCF and Pt/MC rather came from the difference in BET surface area of MCF-A and bulk MC, 380 m^2/g and 625 m^2/g, respectively. Same phenomenon was also found in section 3.3.4. Regarding to ECSA, Pt/MCF-A, Pt/MC and Pt/KB showed 41.5 m^2/g, 34.83 m^2/g and 59.5 m^2/g, respectively. The lower ECSA for Pt/MCF and Pt/MC was expected from different hydrogen adsorption behavior on Pt nanoparticles within mesopores [2]. Even through this hydrogen adsorption behavior is not well understood, the hydrophobic character of mesopores might be a reason for this difference.

4.2.2 Evaluation of ORR activity

LSV curves of Pt/MCF-PVA and Pt/MCF-B were obtained and are shown in Fig. 4.10. Unlike Pt/MCF-B, Pt/MCF-PVA only achieved the limiting current of 2.91 mA/cm^2 with a rotating speed of 1600 rpm. Because of the better Pt dispersion in Pt/MCF-B, significant improvements in ECSA followed by the reasonable limiting current, 5.7 mA/cm^2, were found. However, in terms of ORR mass activity at 0.9 V (vs. RHE), Pt/MCF-B still resulted in low.

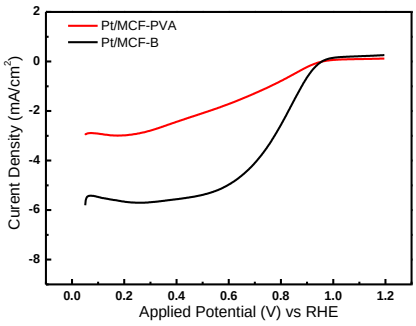

Fig. 4.10 LSV curves of Pt/MCF-PVA and Pt/MCF-B under 1600 rpm.

On the other hand, LSV curves of Pt/MCF-A, Pt/bulk MC and TKK Pt/KB resulted in similar, in terms of the onset potential and limiting current as shown in Fig. 4.11 (a).

In order to further analyze ORR activity in detail, the K-L analysis was performed by changing rotation speed, such as 400 rpm, 900 rpm, 1600 rpm, 2500 rpm and 3600 rpm. K-L plots of each electrocatalyst at 0.9 V are shown in Fig. 4.11 (b). Based on i_k at 0.9 V, mass activities of Pt/MC, Pt/MC, and Pt/KB were 175.6 A/g, 173.9 A/g, and 184.7 A/g, respectively. Mesoporous carbon catalysts showed the slightly lower mass activity. However, the difference in ORR mass activity was rather small than the difference in ECSA, suggesting that even though different hydrogen adsorption behavior on Pt nanoparticles within mesopores was seen, the access of oxygen to mesopores followed by ORR was not limited.

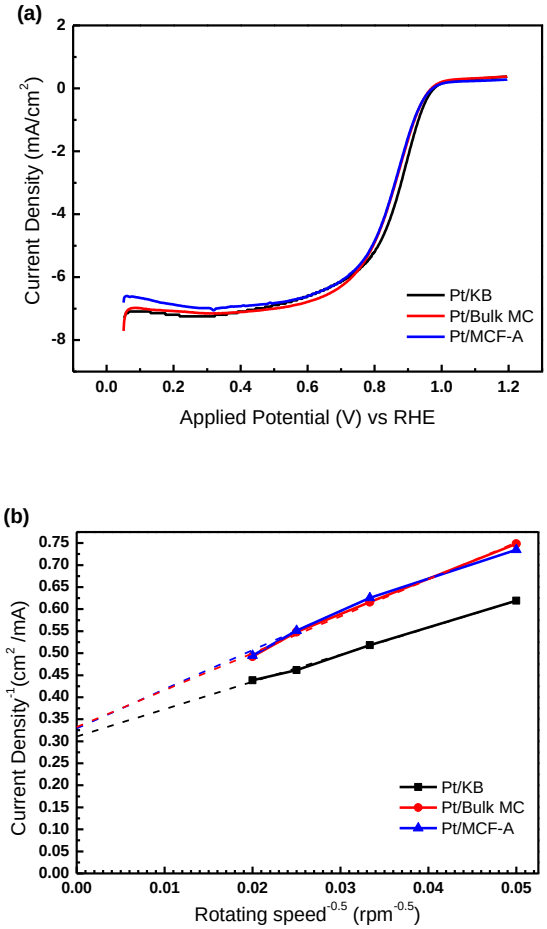

Fig. 4.11 (a) LSV curves of Pt/MC, Pt/MCF and Pt/KB under 1600 rpm and (b) the corresponding K-L plots at 0.9 V.

4.3 Conclusion

In this chapter, the characterization of Pt/MCFs were fully discussed.

With MCF-A, successful encapsulation of Pt nanoparticles into pores was confirmed. During the fundamental electrochemical characterization of Pt/MCF, Pt/MC, and Pt/KB, mesoporous catalysts showed similar but slightly lower ORR mass activity. However, the difference was rather small in mass activity than in ECSA, suggesting that even through different hydrogen adsorption behavior on Pt nanoparticles within mesopores was seen, the access of oxygen to mesopores was not limited.

List of references

[1] A. L. Patterson, The scherrer formula for X-ray particle size determination, Phys. Rev. **56**, 978-982 (1939)

[2] J. Zeng, F. Su, J. Y. Lee, X. S. Zhao, J. Chen, X. Jiang, Method for preparing highly dispersed Pt catalysts on mesoporous carbon support, J. Mater. Sci., **42,** 7191–7197 (2007).

CHAPTER 5

Evaluation of MEAs Made by Pt/MCFs Cathodes

Chapter 5 : Evaluation of MEAs Made by Pt/MCFs Cathodes

Introduction

In this chapter, evaluation of MEAs made by Pt/MCFs cathodes was fully introduced. This chapter was divided into three sections; 5.1 Evaluation of MEA made by MCF-A cathode, 5.2 Evaluation of MEA made by MCF-HC cathode, and 5.3 evaluation of MEA made by MCF sheet cathode.

5.1 Evaluation of MEA made by MCF-A cathode

MEA made by 800-rpm ball-milled 28 wt.% Pt/MCF-A cathode with 28 wt.% Nafion content was evaluated compare with a MEA made by TKK Pt/KB cathode. Only cathode materials were different, but Pt loading was kept to 0.3 mg/cm^2 as explained in section 2.4.2.

IV performance of MEAs made with TKK 46 wt.% Pt/KB cathode and 28 wt.% Pt/MCF-A cathode are shown in Fig. 5.1. MEA made with 46 wt.% Pt/MCF-A cathode resulted in lower performance than MEA with TKK 46 wt.% Pt/KB cathode. MEA with 28 wt.% Pt/MCF-A cathode showed 425 mA/cm^2 at 0.6 V, while MEA with TKK 46 wt.% Pt/KB cathode showed 623 mA/cm^2 at 0.6 V, which was about 45 % higher.

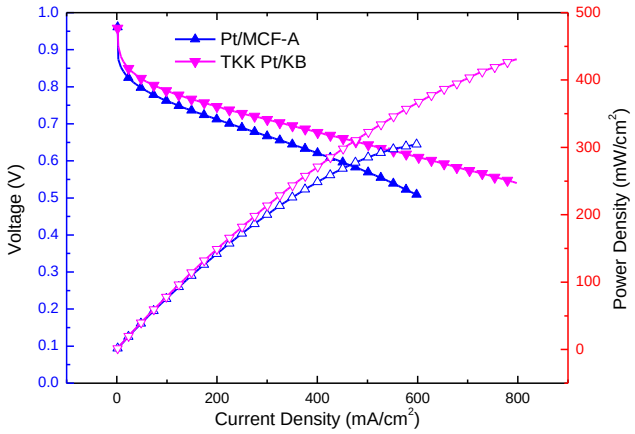

Fig. 5.1. IV performance of MEAs made with TKK 46 wt.% Pt/KB and 28 wt.% Pt/MCF-A cathodes.

To understand reasons of the low IV performance with 28 wt.% Pt/MCF-A cathode, activation overvoltage, ohmic overvoltage, and concentration overvoltage were separately analyzed and are shown in Fig. 5.2.

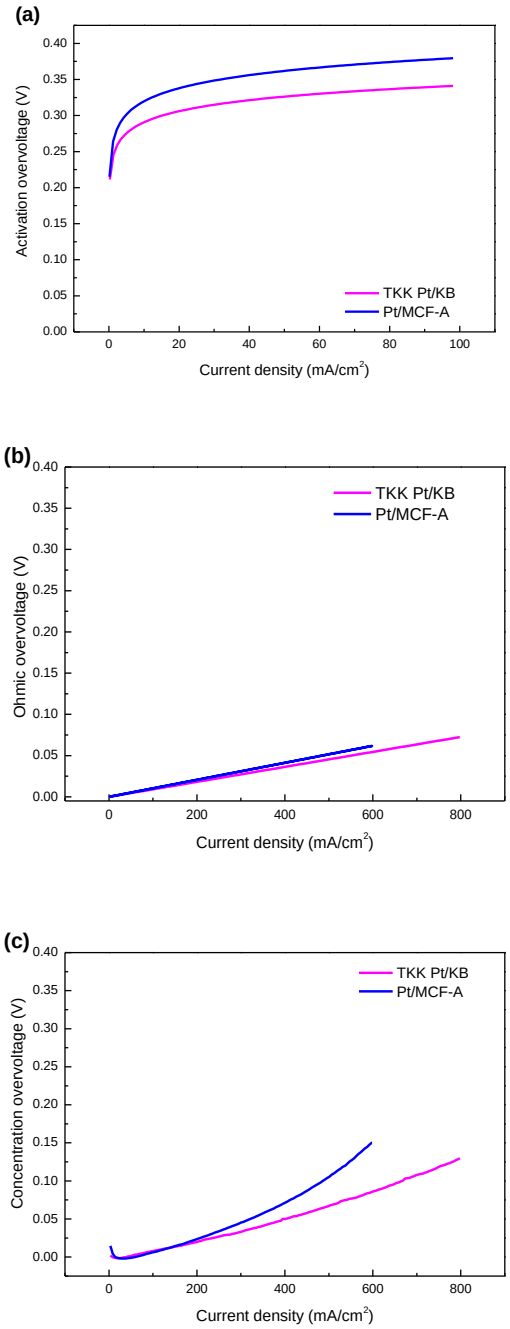

Fig. 5.2. (a) Activation overvoltage, (b) ohmic overvoltage, and (c) concentration overvoltage separated from I-V curves of MEAs made with TKK 46 wt.% Pt/KB cathode and 28 wt.% Pt/MCF-A cathodes.

According to Fig. 5.2 (b), ohmic overvoltage resulted in similar, which was reasonable since the ohmic overvoltage mostly came from Nafion membrane resistance. In terms of activation overvoltage and concentration overvoltage, MEA with 28 wt.% MCF-A cathode revealed higher overvoltage comparing to MEA with TKK 46 wt.% Pt/KB cathode, even though fundamental ORR activity evaluated in section 4.2.2 was similar for both electrocatalysts. The major difference in two experimental conditions was whether or not there was Nafion ionomer. The narrow mesopores of MCFs, too much Nafion ionomer might be introduced, and optimization of introduction of Nafion ionomer might be necessary. Therefore, varying the Nafion ionomer content was considered. During the preparation of Pt/MCF-A slurry for MEAs, the amount of Nafion content was reduced to 14 wt.% and 7 wt.%.

IV performance of MEAs made with 28 wt.% Pt/MCF-A cathode with the different Nafion ionomer content were evaluated and are shown in Fig. 5.3. Although the Nafion content was reduced, increase in IV performance of MEA was not seen. Therefore, simply reducing the Nafion content did not solve mass transfer issues within mesopores, and so MCFs with further larger mesopore diameter, MCF-HC, was tested in the following section.

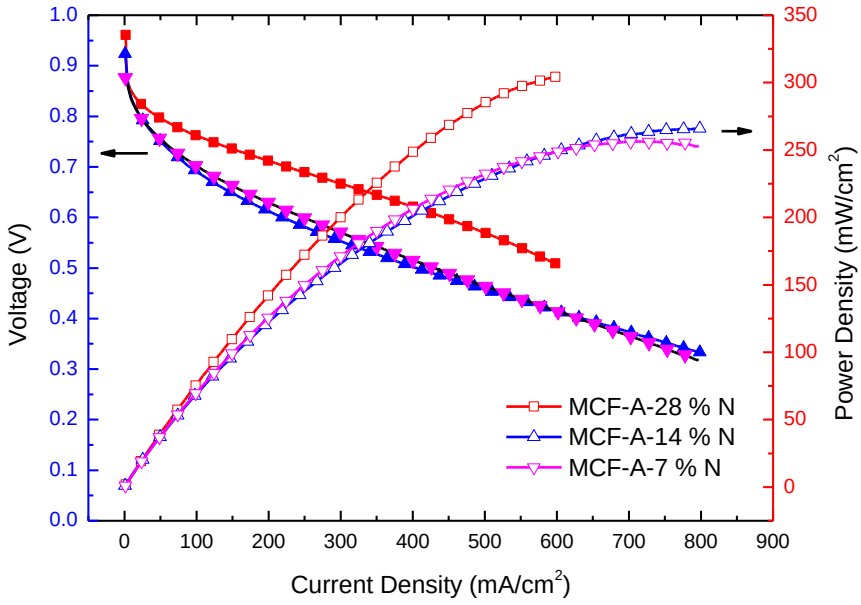

Fig. 5.3 IV performance of MEAs made with Pt/MCF-A with the different Nafion content.

5.2 Evaluation of MEA made by Pt/MCF-HC cathode

IV performance of MEAs made with 28 wt.% Pt/MCF-HC cathode, whose diameter and volume were largest among MCFs, was evaluated and are shown in Fig. 5.4. MEAs made by 28 wt.% Pt/MCF-A cathode and TKK 46 wt.% Pt/KB cathode was used as references. IV performance of MEA made with 28 wt.% Pt/MCF-HC cathode was significantly improved comparing to MEA made with 28 wt.% Pt/MCF-A cathode. The current density at 0.6 V was increased from 425 mA/cm^2 to 615 mA/cm^2, resulting in almost the same IV performance as MEA made with TKK Pt/KB cathode, 623 mA/cm^2 at 0.6 V.

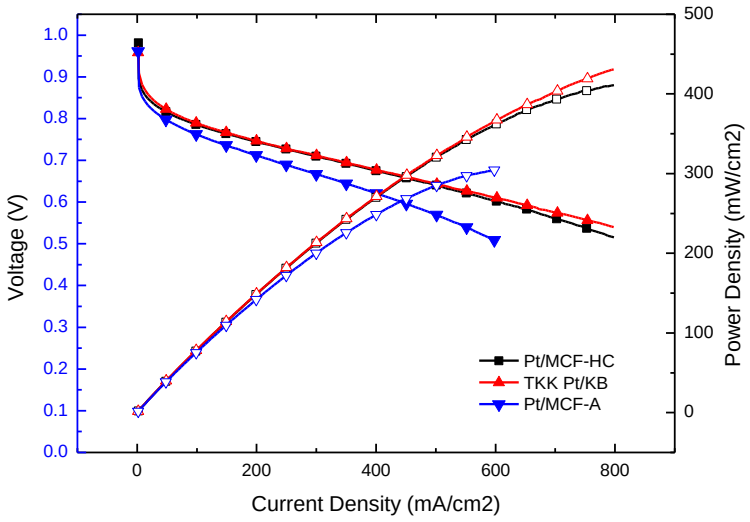

Fig. 5.4. IV performance of MEAs made with Pt/MCF-HC, Pt/MCF-A and TKK Pt/KB cathodes.

Activation overvoltage, Ohmic resistance, and concentration overvoltage were further analyzed separately for these three cases and are shown in Fig. 5.5.

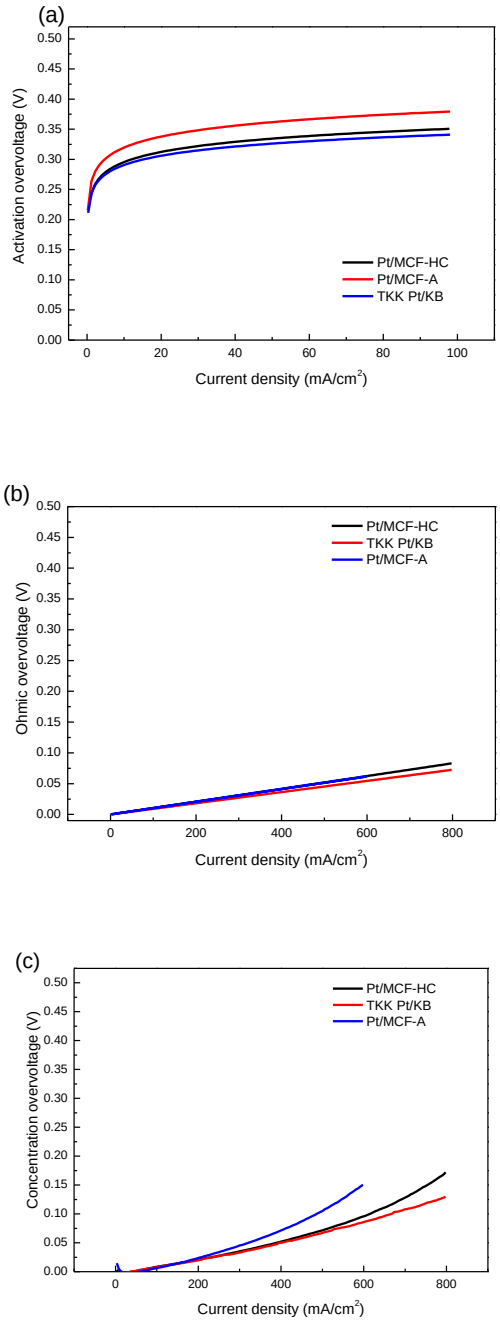

Fig. 5.5 (a) Activation overvoltage, (b) ohmic overvoltage, and (c) concentration overvoltage of MEAs made with 28 wt.% Pt/MCF-HC, 28 wt. % MCF-A and TKK 46 wt.% Pt/KB.

As seen in Fig. 5.5 (b), ohmic overvoltage was almost the same for MEA made by Pt/MCF-HC cathode and Pt/MCF-A cathode, and slightly higher than for MEA made by TKK 46 wt.% Pt/KB cathode. The resulting thicker of MCF-based catalysts, about

12-14 μm for MCF-based cathodes vs 8-9 μm for Pt/KB cathode, due to the lower wt.% Pt deposition, resulted slightly higher in ohmic overvoltage. In terms of activation overvoltage as shown in Fig. 5.6 (a), it was improved with Pt/MCF-HC cathode than with Pt/MCF-A cathode. The activation overvoltage at 40 mA/cm^2 was improved from 0.35 V to 0.32 V, which was almost the same as MEA made with 46 wt.% TKK Pt/KB cathode. Concentration overvoltage in Fig. 5.6 (c) was also improved.

Therefore, the enlargement in mesopore diameter and volume improved the mass transfer within mesopores even after Nafion encapsulation. However, ohmic overvoltage was still slightly higher due to the thicker catalyst layer. According to the literature, since the ESD-made electrode used as a fine sheet without crushing into powder shows better conductivity [1]. Therefore, in the following section, the MCF-sheet electrodes were considered.

5.3 Evaluation of MEAs made by MCF sheet cathode

First 12 wt.% Pt/MCF sheet was directly applied as the cathode catalyst layer as described in section 2.4.2. MEAs made with Pt/MCF sheet cathode resulted in low OCV around 0.8 V and low current density, like 100 mA/cm^2 at 0.6 V.

The poor contact between Pt/MCF sheet and PEM probably led to low IV performance. Since MCF sheet was consist of μm-scale diameter of fibers and macropores between fibers. Therefore, addition of Pt/KB to MCF sheet was tried in order to improve the contact between the electrode and membrane.

IV performance of MEAs made with 46 wt.% Pt/KB-MCF sheet cathode was evaluated and shown in Fig. 5.6. MEAs made by Pt/MCF-HC cathode and TKK Pt/KB cathode are also shown in Fig. 5.6. IV performance of MEA made with Pt/KB-MCF sheet cathode resulted in slightly lower, the current density at 0.6 V was 606 mA/cm^2, 612 mA/cm^2 and 622 mA/cm^2 for MEAs with 46 wt.% Pt/KB-MCF sheet, 28 wt.% Pt/MCF-HC and TKK 46 wt.% Pt/KB cathode, respectively.

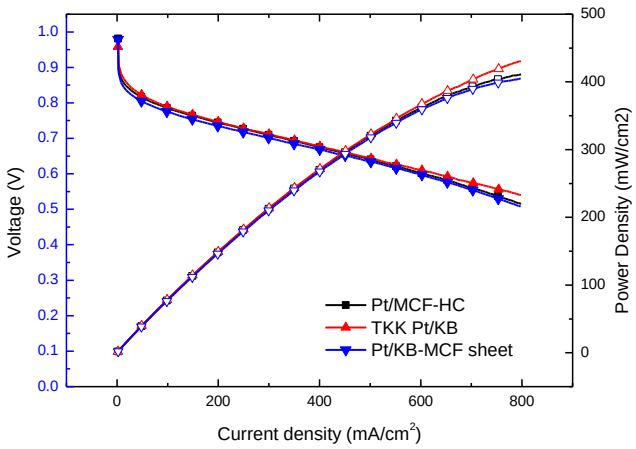

Fig. 5.6. IV performance of MEAs made with 28 wt.% Pt/MCF-HC, 46 wt.% Pt/KB-MCF sheet, and TKK 46 wt.% Pt/KB cathodes.

Then, activation overvoltage, ohmic resistance, and concentration overvoltage were separately and are shown in Fig. 5.7.

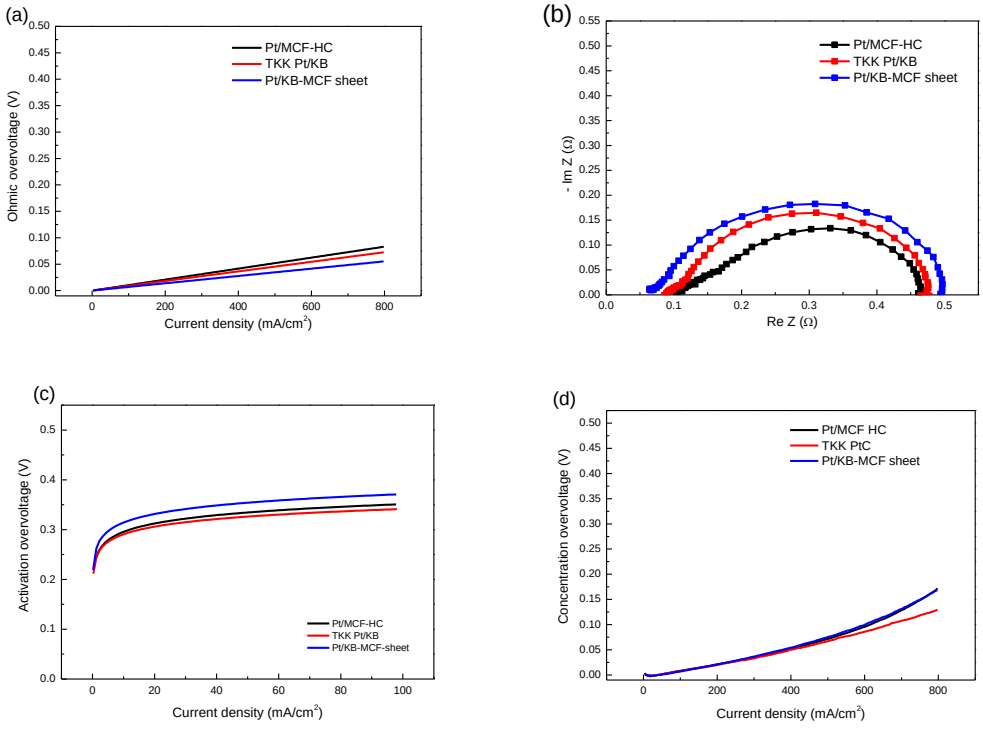

Fig. 5.7. (a) Ohmic overvoltage, (b) Nyquist plots obtained at 200 mA/cm^2, (c) activation overvoltage and (c) concentration overvoltage MEAs made with 46 wt.% Pt/KB-MCF sheet, 28 wt.% Pt/MCF-HC, and 46 wt.% Pt/KB cathodes.

Regarding to ohmic resistant measured from EIS at a current density of 200 mA/cm^2, Pt/KB-MCF sheet cathode showed lower resistance, 70 mΩ, than Pt/MCF-HC and Pt/KB cathodes, 105 mΩ and 96 mΩ, respectively. The MCF sheet, whose μm-scale pores were partially filled up by Pt/KB, resulted in better electron conductivity and low ohmic overvoltage as seen in Fig. 5.7 (a). On the other hands, in terms of the activation overvoltage and concentration overvoltage as shown in Fig. 5.7 (c) and (d), respectively, with Pt/KB-MCF sheet cathode slightly higher activation and concentration overvoltage were seen. Since MCF sheet itself was Pt-free for Pt/KB-MCF sheet cathode, the use of Pt deposited MCF sheet might further improve the activation and concentration overvoltage. Therefore, MEA with Pt/KB-Pt/MCF sheet cathode was made and evaluated.

IV performance of MEA with 46 wt.% Pt/KB-Pt/MCF sheet cathode is shown in Fig. 5.8. Since Pt/MCF sheet contained 0.075 mgPt/cm^2, resulting composite contained Pt/KB first layer with 0.15 mgPt/cm^2, Pt/MCF sheet, and Pt/KB top layer with 0.075 mgPt/cm^2. Therefore, the total Pt loading was kept to 0.3 mgPt/cm^2.

MEAs made with 46 wt.% Pt/KB-MCF sheet cathode and TKK 46 wt.% Pt/KB cathode are also shown in Fig. 5.8. IV performance of MEA made with 46 wt.% Pt/KB-Pt/MCF sheet cathode resulted in slightly lower. The current density at 0.6 V was 592 mA/cm^2, 606 mA/cm^2 and 622 mA/cm^2, for MEAs with 46 wt.% Pt/KB-Pt/MCF sheet, 46 wt.% Pt/KB-MCF sheet, and TKK 46 wt.% Pt/KB, respectively.

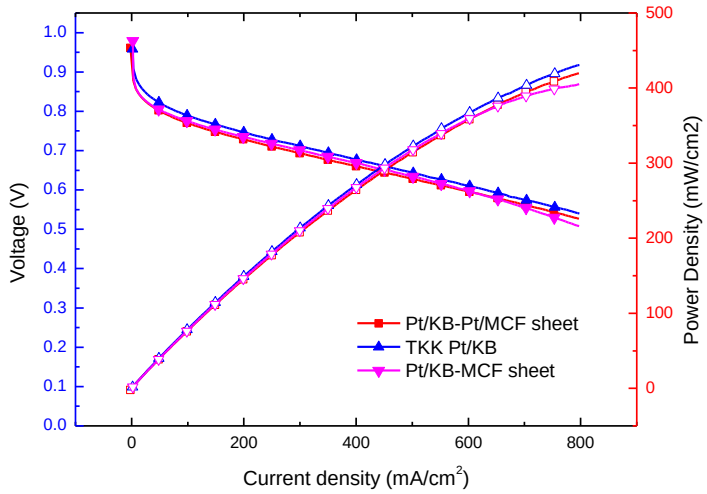

Fig. 5.8 IV performance of MEAs made with Pt/KB-Pt/MCF sheet, Pt/KB-MCF sheet and TKK Pt/KB cathodes.

Then, activation overvoltage, ohmic overvoltage, and concentration overvoltage were separately analyzed and are shown in Fig. 5.9.

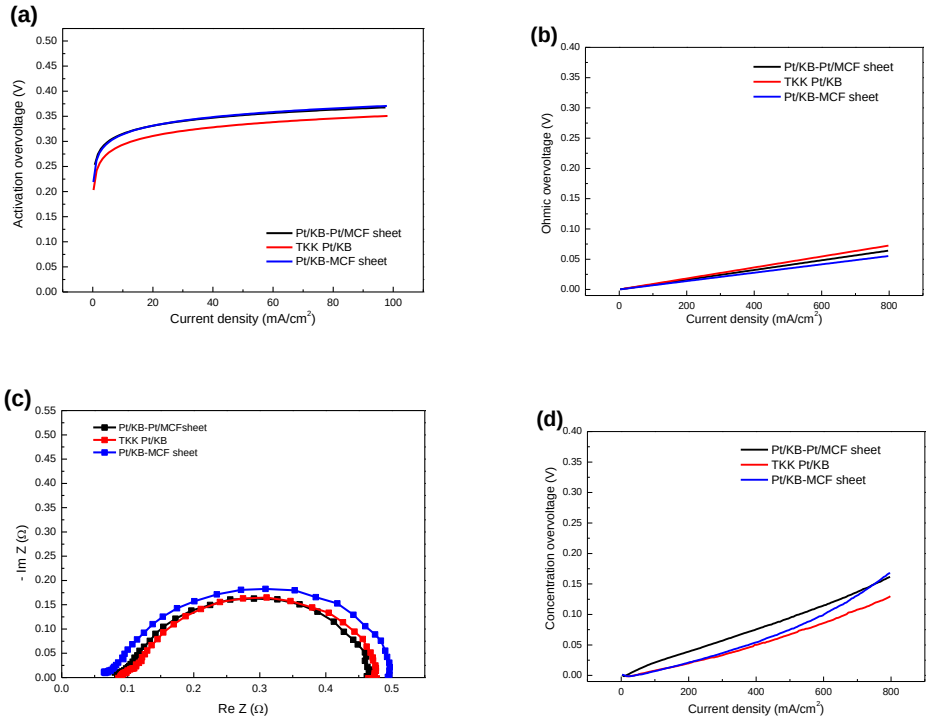

Fig. 5.9 (a) Activation overvoltage, (b) ohmic overvoltage, (c) Nyquist plots obtained at 200 mA/cm^2, and (d) concentration overvoltage MEAs made with 46 wt.% Pt/KB-Pt/MCF sheet, 46 wt.% Pt/KB-MCF sheet, and TKK 46 wt.% Pt/KB cathodes.

As shown in Fig. 5.9 (a), activation overvoltage of MEA made with Pt/KB-Pt/MCF sheet cathode was not improved unfortunately. Ohmic overvoltage rather slightly increased with Pt/MCF sheet than with MCF sheet as shown in Fig. 5.9 (b). The concentration overvoltage significantly increased in comparison to other MEAs as shown in Fig. 5.13 (c).

Since the difference in MEA performance between 46 wt.% Pt/KB-MCF sheet and 46 wt.% Pt/KB-Pt/MCF sheet cathodes was not seen and activation overvoltage was almost same, only the first layer of Pt/KB (0.15 mgPt/cm^2) was possibly used. Therefore, another comparison with MEA made by 46 wt.% Pt/KB with 0.15 mgPt/cm^2 [2] was performed. Since the internal resistance might be different, IR-free IV performance of MEAs with 46 wt.% Pt/KB-Pt/MCF sheet, 46 wt.% Pt/KB-MCF sheet, 46 wt.% Pt/KB (0.30 mgPt/cm^2), and 46 wt.% Pt/KB (0.15 mgPt/cm^2) cathodes are

shown in Fig. 5.10.

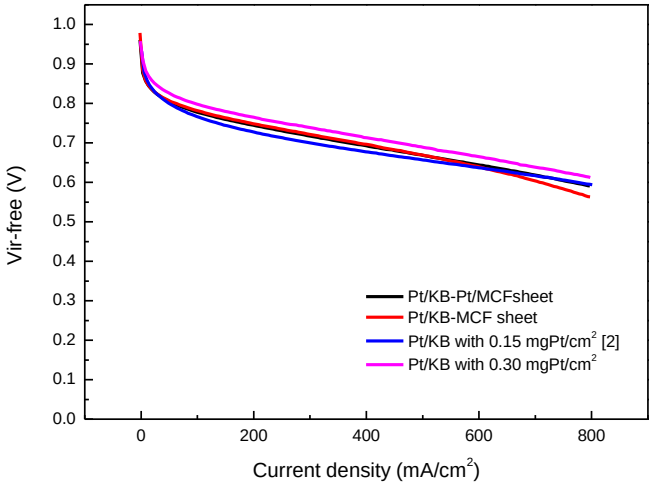

Fig. 5.10 IV performance of MEAs made with 46 wt.% Pt/KB/Pt/MCF sheet, 46 wt.% Pt/KB/MCF sheet, TKK 46 wt.% Pt/KB (0.30 mgPt/cm^2), and TKK 46 wt.% Pt/KB (0.15 mgPt/cm^2) cathodes.

As shown in Fig. 5.10, IR-free IV performance of MEA made with 46 wt.% Pt/KB-MCF sheet and 46 wt.% Pt/KB-Pt/MCF sheet cathodes were closer to that with 46 wt.% Pt/KB (0.15 mgPt/cm^2) than to 46 wt.% Pt/KB (0.30 mgPt/cm^2). Therefore, the second layer of Pt/KB was most likely not in use successfully. A major reason for this probably because no successful introduction of Nafion ionomer within the MCF sheet between two Pt/KB layers.

In addition, MCF sheet became fragile after addition of Pt. During Pt deposition process, carbon might be oxidized slightly. Then Pt/MCF sheet resulted in slightly low electric conductivity, leading to higher ohmic resistance.

Regarding to increase in concentration overvoltage, partial flooding of water might be a reason. Since Pt/MCF sheet was fragile, and a part sheet was crashed into small pieces, the reaction was concentrated on a certain part of the electrode, leading to partial flooding of produced water.

5.4 Conclusion

In this chapter, Pt/MCF-A was ball milled and used as cathode catalyst layer of MEA, but only 425 mA/cm^2 at 0.6 V of IV performance was achieved. To further achieve higher IV performance, the MCF-HC with enlarged mesopores diameter was rather used, and Pt/MCF-HC showed a comparable IV performance, 615 mA/cm^2 at 0.6 V, to the TKK Pt/KB catalyst, 623 mA/cm^2. In order to further solving the ohmic resistance and concentration overvoltage issues, MCF sheet cathode was introduced with the combination of TKK 46 wt.% Pt/KB, the improvement in ohmic resistant was found. However, a critical issue of successful Nafion introduction into MCF sheet was also found.

List of references

[1] W. Zhang, P. N. Pintauro, High-Performance Nanofiber Fuel Cell Electrodes, ChemSusChem, 4, 1753 – 1757 (2011).

[2] 武井翔太、修士論文（R1 年）

CHAPTER 6

Conclusion

Chapter 6 Conclusion and Future Outlook

6.1 Conclusion

As explained in the introduction, the cost and durability of catalyst layers are known as major issues for wide commercialization of PEFCs. In previous study, our group has been trying to improve the durability of catalysts through the approach of using MC as a catalyst support. Although improved durability has successfully reported, the slightly low IV performance has been found due to the disorderness in the μm-structure.

Therefore, the aim of this study was to further improve the IV performance of MC-based catalyst by controlling both its nm- and μm-scale structure. Different from conventional powder based catalyst layers, with fiberized MC, named as mesoporous carbon fibers (MCFs), a new structure design of catalyst layers was achieved. Details of achievements in this study were listed as follow;

- MCFs were successfully developed by combining the organic-organic self-assembly and electrospinning disposition. Mesoporosity, such as pore volume and pore diameter, of MCFs were also successfully controlled.
- Higher electronic conductivity MCFs (-20 mΩ in fine MCF sheet) comparing to common carbon materials was achieved owing to the fiber structure, and it was further improved as MCF sheet.
- Comparative IV performance of MEA made with a standard cathode 46 wt.% Pt/KB was achieved by MEA with Pt/MCFs consisting of largest diameter (7 nm), 28 wt.% Pt/MCF-HC (623 mA/cm^2 at 0.6 V with 46 wt.% Pt/KB, and 615 mA/cm^2 at 0.6 V with 28 wt.% Pt/MCF-HC).
- Furthermore, MCF sheet cathodes were also tried owing to fully control both μm-structure and nm-structure. An advantage in reducing ohmic overvoltage was found. However, some critical issues came up and were explained in the following.

Toward our goal, many progresses were achieved, but only comparative IV performance to the standard MEA was achieved. In order to further improve IV performance, MCF sheet cathodes became a key, and two major critical issues to overcome were found in the following;

- Nafion introduction to MCF sheet: During this study, Nafion ionomer was not

successfully introduced into MCF sheet. Therefore, Pt in MCF sheet was not efficiently used, and Pt/KB layer above MCF sheet was not successfully used, either.

- Pt deposition to MCF sheet: Deposition wt.% Pt was relatively low comparing to other electrocatalysts. Therefore, performance resulted in low. Because of Pt deposition process, MCF sheet also had a tendency to be fragile.

6.2 Future outlook

In order to further improve the performance of MCFs based cathodes, possible approaches toward two major critical issues are in the following;

- For successful introduction of Nafion ionomer to MCF sheet, optimization of spray-printing process of Nafion solution onto the MCF sheet should be tried (Fig. 6.1 (a)). Other coating methods, such as dip coating (Fig. 6.1(b)), should also be tried.
- For successful Pt deposition to MCF sheet, repeating the present process of Pt deposition should be tried in order to increase wt.% Pt deposition. However, by considering the MCF sheet became fragile during the current process, other methods should also be considered. Chemical vapor deposition (CVD) or physical vapor deposition (PVD) as shown in Fig. 6.2 may be possible methods.
- In addition to the solution to two critical issues, fiber structure can be further optimized in order to improve the performance of MCFs. Since the diameter can be controlled by the content ratio between polymer precursors and linear additive. In the present process, the further increasing in linear additive, PVA, in precursor solution is difficult, but the using another type of electrospinning called co-axial spinning (Fig. 6.3) is one solution. In this machine, the nozzle with co-axial double layer design needle was used, and the separation of polymer precursors and PVA is possible. With the separation of polymer precursors and PVA, followed by the individual controlling in the feeding rate of each solution, it is possible to further control the fiber diameter.

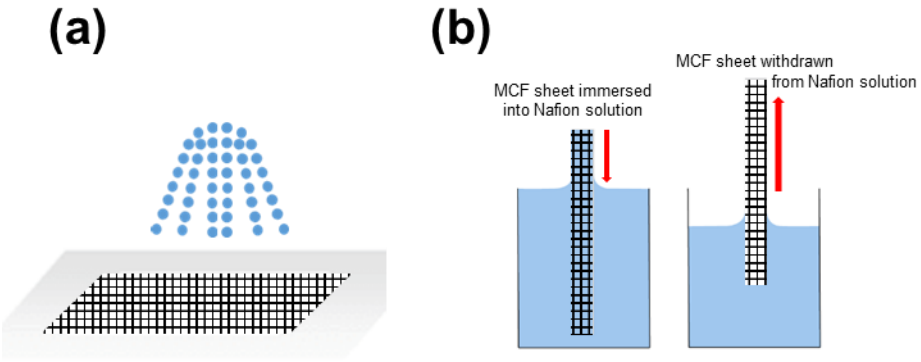

Fig. 6.1 Schematic diagrams showing introduction of Nafion ionomer on MCF sheet by spray-printing process (a) and dip coating process (b).

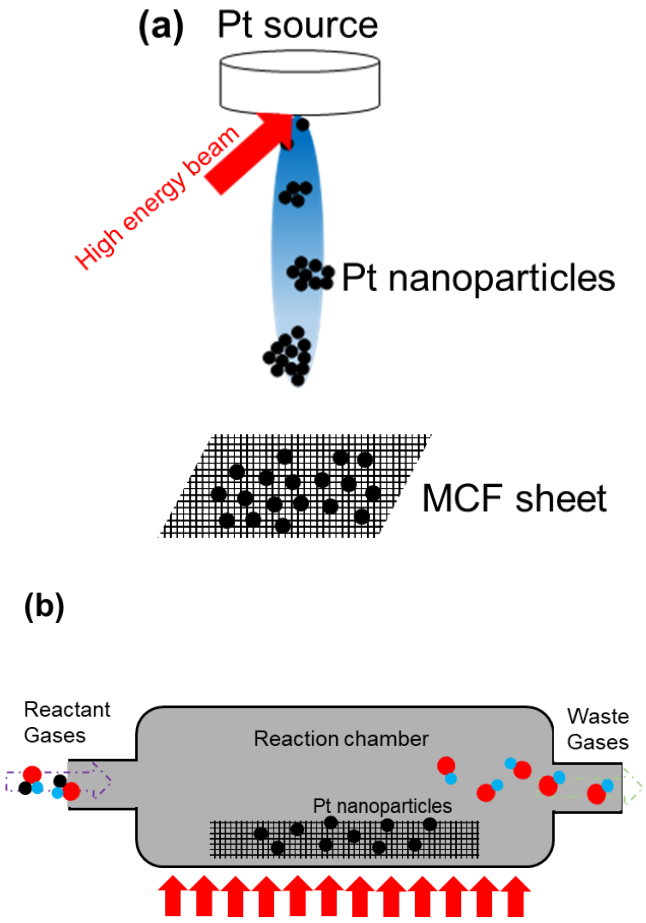

Fig. 6.2 Schematic diagrams showing Pt deposition on MCF sheet by PVD process (a) and CVD process (b).

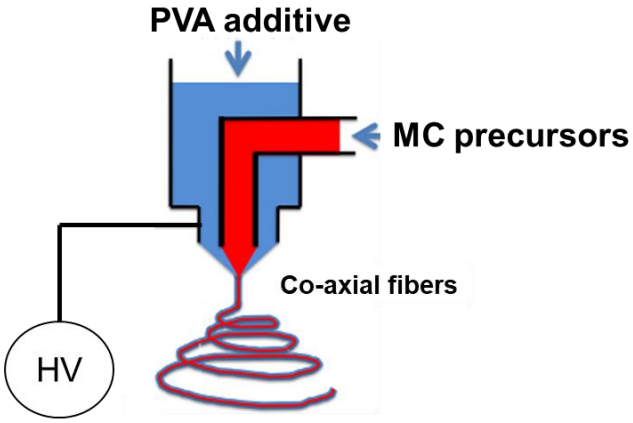

Fig. 6.3 A schematic diagram of co-axial electrospinning device.